

**The Effects of Porous Surfaces on the Control of Flows
over Bluff Bodies of Circular, Square and Rectangular
Cross-Sections**

Sakineh (Parvaneh) Sadeghipour

B.Sc. in Marine Engineering, Naval Architecture
M.Eng. in Mechanical Engineering

Submitted in fulfilment of the requirements for the degree of

Doctor of Philosophy



College of Engineering and Science
Victoria University

July 2018

to:

My Beloved Parents

ABSTRACT

Bluff bodies are an inextricable part of life. They are found abundantly in engineered structures. When exposed to high velocity fluid flows, bluff bodies cause the flow to separate from their surfaces, which result in vortices shed from the bodies. Vortex shedding gives rise to large unsteady forces in the wake of the bluff bodies. The control of such forces is of great importance in engineering design because they reduce drag forces, vibrations and the generation of noise. There is evidence that the application of porous media to the surfaces of bluff bodies immersed in turbulent fluid flows has a profound effect on the associated aerodynamic phenomena. This idea is explored in this thesis by performing a series of experiments and numerical simulations on cylinders treated with porous media. The findings contribute to existing knowledge by providing researchers in the field with a trove of new, and carefully obtained experimental data on the flow fields generated by bluff bodies that have been modified by incorporating regions of porous media. These data will provide theoreticians with benchmark cases against which they can evaluate their mathematical models. The study is significant for two principal reasons. Firstly, it provides new insights into the fundamental mechanisms of the fluid dynamics of flows around bluff bodies, and secondly it has useful practical implications for the design of a multitude of systems immersed in turbulent flow fields. The novelty of the research is that it develops the idea of porous treatment by investigating the effects of the replacement of a part of a bluff body with a porous material and determining the efficacy of such treatment in the control of flow. The benefits include

reduction of drag, vibration and noise, which in turn leads to the reduction in fuel consumption of vehicles and therefore a decline in the emissions of greenhouse gases.

In the experiments, cylinders that have circular, square and rectangular cross sections have been studied. Well-established benchmarks were set by measuring the flow fields around bare solid aluminium cylinders. The flow fields were also established around circular cylinders that had been encased in porous media, and which retained the same dimensions of the bare cylinder. The square and rectangular bluff bodies were modified so that their upstream and downstream halves consisted of solid and porous materials respectively. As a result, their leading and trailing edges were respectively solid and porous. The porous media consisted of open cell polyurethane. Three formulations were used that had permeabilities of $4.64 \times 10^{-7} \text{ m}^2$, $5.70 \times 10^{-8} \text{ m}^2$ and $6.87 \times 10^{-8} \text{ m}^2$. The corresponding porosities were 91.8%, 86.2% and 82.1%. Experiments were performed in a wind tunnel operating under conditions that resulted in a Reynolds number of about 53000 based on the diameter of the circular cylinder and the dimensions of the leading edges of the square and rectangular bodies. The flow streamlines, wake velocity profiles and Reynolds stresses were determined by means of Particle Image Velocimetry (PIV).

The experimental investigations revealed that the porous media applied to the circular cylinder had the most effect on the wake, and the largest effect was observed in the wake generated by the most permeable material. The principal effect of the porous media was to cause the eyes of the recirculation region to be located further downstream. This effect is apparent in all three geometries considered, but the effect of the permeability is increasingly diminished in the square and rectangular geometries. The presence of the porous media also had a significant effect on the Reynolds stresses. For example,

immediately downstream of the cylinders higher normal stresses in the direction of flow are generated by bare cylinders compared with those generated by the cylinders modified by porous media. The effect of the porous media applied to all three geometries is to damp the normal stresses further downstream of the bluff bodies.

Experiments provided results, which were used as benchmarks for numerical simulations. A CFD code, CFX using an SST-RANS turbulence model was validated against the experimental results and further investigations were performed numerically. Square cylinders with and without porous materials were further examined and compared with each other to expand our understanding of the flow structures around the cylinders. A porous material with a measured permeability equal to $4.64 \times 10^{-7} \text{ m}^2$ and a resistance loss coefficient equal to 1658 m^{-1} was used. The same configurations in the experiments, namely the bare square cylinder and the square cylinder with its trailing half composed of porous material have been examined. Furthermore, the effect of the disposition of porous material on the flow behaviour and drag force was studied by examining a square cylinder consisted of porous material at its leading half. The flow behaviour in the wake and in the boundary region, pressure distributions and drag forces were obtained in each case and compared with each other.

Investigations of the flow around the bare and porous-treated square cylinders disclosed that the trailing-half porous cylinder is the most effective in the control of flow. This was demonstrated through the location of the recirculation bubbles, and the drag force. Maximum shift in the recirculation bubbles occurred in the trailing-half porous cylinder. The biggest development in the boundary layer was also observed in the trailing half-porous cylinder. The presence of porous material both at the leading and trailing half of the cylinders resulted in a decrease in the drag force. The maximum reduction in the

drag coefficient was achieved with the trailing-half porous cylinder by 13% compared to the bare cylinder. In addition, the use of porous materials significantly altered the pressure distributions around the cylinders, when the highest pressure gradient was found for the leading-half porous cylinder.

DECLARATION

I, Sakineh Sadeghipour, declare that the PhD thesis entitled ‘The Effects of Porous Surfaces on the Control of Flows over Bluff Bodies of Circular, Square and Rectangular Cross-Sections’ is no more than 100,000 words in length including quotes and exclusive of tables, figures, appendices, bibliography, references and footnotes. This thesis contains no material that has been submitted previously, in whole or in part, for the award of any other academic degree or diploma. Except where otherwise indicated, this thesis is my own work.

Sakineh Sadeghipour

25/07/2018

Signed

Date

ACKNOWLEDGEMENTS

I acknowledge the financial support, in the form of a postgraduate research scholarship, provided by Victoria University, Melbourne, Australia.

I would like to thank my supervisors, Professor Graham Thorpe, and Dr Duncan Sutherland for their guidance and support towards the completion of this thesis. I am grateful to them for encouraging me on conducting high-level research. A large part of my work was accomplished under the supervision of Dr. Mahdi Azarpeyvand. I am grateful to him for providing access to his laboratory and his considerable expertise and advice whilst I was a visiting scholar at the University of Bristol.

My deepest gratitude goes to my father, Keramatollah Sadeghipour, and my mother, Maryam Yahyazadeh, for their endless love, sacrifice and continued support in all stages of my life. Your dedication, hard work and constant patience have taught me so much about life.

I thank my siblings, siblings in law, nephews and nieces who remained near even when far. My special thanks go to my dear cousin, Mehrnoosh Mohammadpour without whom I could not survive the tough times.

Finally, I would like to thank Mr. Joe Trafficante, our IT staff. This work would not have been completed on time without his help in the provision of the computer facilities. I am thankful to all my friends who were a shoulder when I needed them. My thanks also go to my fellow colleagues at the University of Bristol who have offered guidance, feedback and suggestions along the way, and to everyone who directly or indirectly involved during the completion of this thesis.

LIST OF PUBLICATIONS

- **Sakineh Sadeghipour**, Graham R. Thorpe and Duncan Sutherland, “*CFD Simulation of Turbulent Flow over Immersed Bluff Bodies Modified by Porous Materials*”. 6th European Conference on Computational Mechanics (ECCM 6) - 7th European Conference on Computational Fluid Dynamics (ECFD 7), 11 – 15 June 2018, Glasgow, UK.
- **Sadeghipour, S.**, Thorpe, G., and Sutherland, D., “*The Experimental Investigation of the Flow over a Porous Treated Square Cylinder at a Reynold Number of 53000*”. 12th International Conference on Advanced Computational Engineering and Experimenting, 1 – 5 July 2018, Amsterdam, the Netherlands.
- **Sadeghipour, S.**, Thorpe, G. Sutherland, D., “*3-D simulation of turbulent flow past porous-treated square cylinders*”. 26th Annual Conference of the Computational Fluid Dynamics Society of Canada, 10-12 June 2018, Winnipeg, Canada.

Under review:

- **Sadeghipour, S.**, Showkat Ali, S. A., Liu, X., Azarpeyvand, M., Thorpe, G., “*Control of flows around bluff bodies mediated by porous materials*”. Journal of Wind Engineering and Industrial Aerodynamics.

Declaration of Co-Authorship

I hereby declare that the journal publication incorporates the outcome of joint research undertaken in collaboration with my supervisors, Prof Graham Thorpe from Victoria University and Dr. Mahdi Azarpeyvand and my colleagues Syamir Alihan Showkat Ali and Xiao Liu from University of Bristol. The collaboration is covered in Chapter 3 and 4 of the thesis. The author generated the key ideas and performed the primary contributions, experiments, data analysis and interpretation. The contributions of the co-authors were primarily through the provision of guidance and discussions on technical issues, assistance in conducting experiments and editing of the manuscripts.

TABLE OF CONTENTS

ABSTRACT	i
DECLARATION	v
ACKNOWLEDGEMENTS	vi
LIST OF PUBLICATIONS	vii
TABLE OF CONTENTS	viii
LIST OF FIGURES.....	xii
LIST OF TABLES.....	xviii
NOMENCLATURE	xix
CHAPTER 1 Introduction.....	1
1.1 Background.....	1
1.2 Problem Statement.....	2
1.3 Research Objectives.....	3
1.4 Research Methodologies and Techniques.....	4
1.5 Research Contribution to Knowledge and Statement of Significance.....	8
1.5.1 Academic Contribution.....	8
1.5.2 Practical Contribution	10
1.6 Thesis Structure	11
CHAPTER 2 Literature Review on Flow control over Bluff Bodies Using Porous Treatment.....	14
2.1 Introduction.....	14
2.2 Flow Control Techniques.....	19
2.3 Mathematical Formulations for Porous Materials	20
2.3.1 Darcy’s Law and Brinkman Model	21

2.3.2	Darcy–Forchheimer Law	22
2.4	Porous Treatment for Different Configurations.....	23
2.4.1	Circular Cylinders.....	24
2.4.2	Square and Rectangular Cylinders.....	27
2.4.3	Configurations with Blunt Trailing Edges.....	29
2.5	Mathematical Formulations for the Modelling of the Flow Around and Through Porous Materials	30
2.5.1	Implementation of the Mathematical Formulations and Numerical Modelling.....	34
2.6	Study of the Effect of Porous Treatment Through Experiments	40
2.7	Summary.....	43
CHAPTER 3 Experimental System and Instrumentation.....		46
3.1	Introduction.....	46
3.2	Configurations of the Bluff Bodies.....	47
3.3	Porosity and Permeability Measurement	49
3.3.1	Porosity	49
3.3.2	Permeability	51
3.3.2.1	Permeability Uncertainty Analysis.....	53
3.4	Measurement of the Flow Field	55
3.4.1	Experimental Setup.....	56
3.4.2	PIV Sub-Systems and Data Analysis.....	61
3.4.2.1	Pulsed Lasers	61
3.4.2.2	Tracer Particles	62
3.4.2.3	Image Pre-Processing	65
3.4.2.4	Interrogation Area.....	66
3.4.2.5	Evaluation of the Particle Displacement	67
3.4.2.6	PIV Post-Processing	68

3.5	Summary	69
CHAPTER 4 Experimental Results and Discussion		71
4.1	Introduction.....	71
4.2	Circular Cylinder	72
4.2.1	Velocity Components for Circular Cylinders	74
4.2.2	Reynolds Stresses for Circular Cylinders	78
4.3	Square Cylinder	84
4.3.1	Velocity Components for Square Cylinders	86
4.3.2	Reynolds Stresses for Square Cylinders	88
4.4	Rectangular Cylinder	93
4.4.1	Velocity Components for Rectangular Cylinders	94
4.4.2	Reynolds Stresses for Rectangular Cylinders	96
4.5	Drag Coefficients from Experimental Results.....	101
4.6	Conclusions.....	103
CHAPTER 5 Computational Model and Mathematical Formulations.....		104
5.1	Introduction.....	104
5.2	Bluff Body Configurations	107
5.3	Numerical Procedure	108
5.3.1	Mathematical Formulations	108
•	Porous Material.....	109
5.3.2	Shear Stress Transport (SST) Turbulence Model.....	110
5.4	Computational Model Configuration.....	113
5.5	Grid Generation	116
5.5.1	Mesh Structure at the Near Wall Region	117
5.6	Computational Setup.....	122
5.6.1	Boundary Conditions	124

5.7	Solution Convergence and Mesh Independency Analysis.....	127
5.8	Model Verification through Comparison with Experimental Data	130
5.9	Conclusions.....	134
CHAPTER 6 Numerical Results and Discussion.....		136
6.1	Introduction.....	136
6.2	Validation of the URANS Results with Available Data.....	137
6.3	Velocity Streamlines.....	140
6.4	Vorticity Contours	142
6.5	Velocity Components	144
6.5.1	Velocity Components in the Shear Layer Region	145
6.5.2	Velocity Components in the Wake	149
6.6	Pressure.....	152
6.7	Aerodynamic Forces	155
6.8	Conclusions.....	158
CHAPTER 7 Conclusions and Future Work.....		160
7.1	Introduction.....	160
7.2	Key Contributions of the Research	162
7.3	Future Work.....	163
REFERENCES		166
APPENDIX A.....		182
APPENDIX B.....		185

LIST OF FIGURES

Figure 2.1	A schematic of the different flow regimes for circular and square cylinders	17
Figure 2.2	A circular cylinder covered with a sheath of porous material.	25
Figure 2.3	The location of the porous treatment on a square and rectangular cylinder commonly used in the literature. (a) a porous cover around a square cylinder, (b) porous layers around a rectangular cylinder.	29
Figure 2.4	Schematic of the blunt trailing edge flat plate with a porous section at the trailing edge (Showkat Ali <i>et al.</i> , 2017).	30
Figure 3.1	The bare circular, square and rectangular cylinders used as the references and the cylinders treated with porous materials. The circular cylinder was covered with porous materials and the square and rectangular cylinders were formed by replacing the downstream halves with porous materials.	48
Figure 3.2	The porous materials used in the experiments. 1, 2 and 3 represent the 20 PPI, 40 PPI and 60 PPI, respectively. Their characteristics are given in Table 3.1.	48
Figure 3.3	The experimental setup for the measurement of permeability of porous materials.	53
Figure 3.4	A sketch of the wind tunnel test section with a sample test model and the coordinate system with its origin at the centre of the models. The camera is positioned on the transparent side of the wind tunnel in the direction of the cross section of the models and the laser is located below the models and outside the wind tunnel.	57
Figure 3.5	The solid circular cylinder mounted in the wind tunnel. The black part in the middle is to prevent light reflection due to the aluminium reflective property.	59
Figure 3.6	The porous covered circular cylinder mounted in the wind tunnel. The porous material shown is 60 PPI.	59

Figure 3.7	The solid rectangular cylinder mounted in the wind tunnel. The black part in the middle is to prevent light reflection due to the aluminium reflective property.	60
Figure 3.8	The half-porous rectangular cylinder mounted in the wind tunnel. The porous material shown is 60 PPI.	60
Figure 3.9	The cross correlation procedure in PIV velocity measurement. A plot is obtained from two corresponding interrogation areas using a cross-correlation algorithm, which is then used to calculate the velocity vector.	67
Figure 4.1	Time-averaged streamline topology for circular cylinders; (a) bare cylinder, (b) cylinder covered with 60 PPI porous layer, (c) cylinder covered with 40 PPI porous layer and (d) cylinder covered with 20 PPI porous layer.	73
Figure 4.2	Mean stream-wise velocities at different axial locations from circular cylinders. black line: solid; green line: porous 60 PPI; blue line: porous 40 PPI; red line: porous 20 PPI.	75
Figure 4.3	Mean cross-stream velocities at different axial locations from circular cylinders. black line: solid; green line: porous 60 PPI; blue line: porous 40 PPI; red line: porous 20 PPI.	77
Figure 4.4	The wake width generated in the wake of solid circular cylinder and the circular cylinder treated with 20 PPI porous material.	79
Figure 4.5	Normal stream-wise Reynolds stress in the wakes of the circular cylinders. black line: solid; green line: porous 60 PPI; blue line: porous 40 PPI; red line: porous 20 PPI.	81
Figure 4.6	Normal cross-stream Reynolds stress in the wakes of the circular cylinders. black line: solid; green line: porous 60 PPI; blue line: porous 40 PPI; red line: porous 20 PPI.	82
Figure 4.7	Shear Reynolds stress in the wakes of the circular cylinders. black line: solid; green line: porous 60 PPI; blue line: porous 40 PPI; red line: porous 20 PPI.	83
Figure 4.8	Time-averaged streamlines generated by square cylinders; (a) bare cylinder, (b) cylinder treated with 60 PPI porous layer, (c) cylinder treated with 40 PPI porous layer and (d) cylinder treated with 20 PPI porous layer.	85

Figure 4.9	Mean stream-wise velocities at different axial locations generated by the square cylinder. black line: solid; green line: porous 60 PPI; blue line: porous 40 PPI; red line: porous 20 PPI.	87
Figure 4.10	Mean cross-stream velocities at different axial locations generated by the square cylinder. black line: solid; green line: porous 60 PPI; blue line: porous 40 PPI; red line: porous 20 PPI.	88
Figure 4.11	Normal Reynolds stress components in the wakes of the square cylinders. black line: solid; green line: porous 60 PPI; blue line: porous 40 PPI; red line: porous 20 PPI.	90
Figure 4.12	Normal Reynolds stress components in the wakes of the square cylinders. black line: solid; green line: porous 60 PPI; blue line: porous 40 PPI; red line: porous 20 PPI.	91
Figure 4.13	Shear Reynolds stress components in the wakes of the square cylinders. black line: solid; green line: porous 60 PPI; blue line: porous 40 PPI; red line: porous 20 PPI.	92
Figure 4.14	Time-averaged streamlines generated by rectangular cylinders; (a) bare cylinder, (b) cylinder treated with 60 PPI porous layer, (c) cylinder treated with 40 PPI porous layer and (d) cylinder treated with 20 PPI porous layer.	93
Figure 4.15	Mean stream-wise velocities at different axial locations from rectangular cylinder. black line: solid; green line: porous 60 PPI; blue line: porous 40 PPI; red line: porous 20 PPI.	95
Figure 4.16	Mean cross-stream velocities at different axial locations from rectangular cylinder. black line: solid; green line: porous 60 PPI; blue line: porous 40 PPI; red line: porous 20 PPI.	96
Figure 4.17	Reynolds stress components in the wakes of the rectangular cylinders. black line: solid; green line: porous 60 PPI; blue line: porous 40 PPI; red line: porous 20 PPI.	98
Figure 4.18	Reynolds stress components in the wakes of the rectangular cylinders. black line: solid; green line: porous 60 PPI; blue line: porous 40 PPI; red line: porous 20 PPI.	99
Figure 4.19	Reynolds stress components in the wakes of the rectangular cylinders. black line: solid; green line: porous 60 PPI; blue line: porous 40 PPI; red line: porous 20 PPI.	100
Figure 4.20	The control volume around the cylinder to calculate the drag coefficient based on the integral momentum equation	101

Figure 5.1	The square cylinders used in the numerical simulations; a) bare cylinder used as the reference, b) the square cylinder treated with 20 PPI porous material at its trailing half, c) the square cylinder treated with 20 PPI porous material at its leading half.	107
Figure 5.2	Schematic of the computational domain showing a) side view and b) top view containing the dimensions of the domain.	115
Figure 5.3	Perspective view of the model geometry in DesignModeler showing the square cylinder with its leading half comprising porous material.	115
Figure 5.4	Side view of the structured mesh generated for the bare square cylinder; a) whole domain, b) enlarged view showing the finer mesh around the cylinder.	120
Figure 5.5	Side view of the structured mesh generated for the square cylinder with porous material at its leading half: a) whole domain, b) enlarged view showing the finer mesh around the cylinder.	121
Figure 5.6	The conditions used on the boundaries of the domain encasing all the cases studied.	125
Figure 5.7	Stream-wise velocities at different axial locations in the wake region for the bare square cylinders; Black solid line: steady RANS, Orange dotted line: time-averaged experimental results.	132
Figure 5.8	Cross-stream velocities at different axial locations in the wake region for the bare square cylinders; Black solid line: steady RANS, Orange dotted line: time-averaged experimental results.	132
Figure 5.9	Stream-wise velocities at different axial locations in the wake region for the trailing-half porous square cylinders; Dark blue line: steady RANS, Red line: time-averaged experimental results.	133
Figure 5.10	Cross-stream velocities at different axial locations in the wake region for the trailing-half porous square cylinders; Dark blue line: steady RANS, Red line: time-averaged experimental results.	134
Figure 6.1	Profiles of the time-averaged stream-wise velocity at the centreline downstream the solid square cylinder. Comparison is made between the experimental results of Durão <i>et al.</i> (1988) and averaged numerical velocity profile of Trias <i>et al.</i> (2015).	138

Figure 6.2	Profiles of the time-averaged stream-wise velocity at $x/H=-0.625$. Comparison is made between the numerical results of Minguez <i>et al.</i> (2011) and Trias <i>et al.</i> (2015).	139
Figure 6.3	Profiles of the time-averaged stream-wise velocity at $x/H=0.625$. Comparison is made between the numerical results of Minguez <i>et al.</i> (2011) and Trias <i>et al.</i> (2015).	139
Figure 6.4	Time-averaged velocity streamline generated by square cylinders; (a) bare cylinder, (b) cylinder treated with 20 PPI porous layer at the trailing half, (c) cylinder treated with 20 PPI porous layer at the leading half.	141
Figure 6.5	Contours of instantaneous vorticity magnitude in the wake of the square cylinders; (a) bare cylinder, (b) cylinder treated with 20 PPI porous layer at the trailing half, (c) cylinder treated with 20 PPI porous layer at the leading half.	143
Figure 6.6	Axial locations around the cylinder used in Figures 6.7 to 6.9; a: $x/H = -0.9$, b: $x/H = -0.8$, c: $x/H = -0.7$, d: $x/H = -0.6$, e: $x/H = -0.5$, f: $x/H = -0.4$, g: $x/H = -0.3$, h: $x/H = -0.2$, i: $x/H = -0.1$.	144
Figure 6.7	Time-averaged stream-wise velocities at different axial locations in the shear layer region for the bare and porous-treated square cylinders.	147
Figure 6.8	Time-averaged cross-stream velocities at different axial locations in the shear layer region for the bare and porous-treated square cylinders.	148
Figure 6.9	Time-averaged stream-wise velocities at different axial locations in the wake of the bare and porous-treated square cylinders.	151
Figure 6.10	Normalised time-averaged stream-wise velocity at the centreline downstream the square cylinders. Comparison is made between the bare square cylinder and the square cylinders with porous materials at their leading and trailing halves.	151
Figure 6.11	Time-averaged pressure at the mid-plane downstream the square cylinders. (a) bare cylinder, (b) cylinder treated with 20 PPI porous layer at the trailing half, (c) cylinder treated with 20 PPI porous layer at the leading half.	154
Figure 6.12	Time-averaged pressure coefficient at the centreline downstream the square cylinders. Comparison is made between the solid	155

square cylinder and the square cylinders with porous materials at their leading and trailing halves.

Figure 6.13	Drag and lift coefficients generated by the solid square cylinder; green line: Drag coefficient, yellow line: Lift coefficient.	156
Figure A.1	TKE content in the wake of rectangular cylinders; (a) bare cylinder, (b) cylinder treated with 60 PPI porous layer, (c) cylinder treated with 40 PPI porous layer and (d) cylinder treated with 20 PPI porous layer.	182
Figure A.2	TKE content in the wake of circular cylinders; (a) bare cylinder, (b) cylinder covered with 60 PPI porous layer, (c) cylinder covered with 40 PPI porous layer and (d) cylinder covered with 20 PPI porous layer.	183
Figure A.3	TKE content in the wake of square cylinders; (a) bare cylinder, (b) cylinder treated with 60 PPI porous layer, (c) cylinder treated with 40 PPI porous layer and (d) cylinder treated with 20 PPI porous layer.	184

LIST OF TABLES

Table 2.1	Compilation of the studies on the use of porous materials for flow control of a circular cylinder. The method of the investigation, flow Reynolds number (Re), the ratio of the thickness of the porous cover (h) to the diameter of the cylinder (D) are presented	26
Table 3.1	Values of porosity and permeability of the porous materials used in the experiments	49
Table 4.1	The drag coefficients for the flow around solid bare circular, square and rectangular cylinders and circular, square and rectangular cylinders with porous materials at their trailing halves calculated by the integral momentum method.	102
Table 5.1	Mean values of drag and base pressure coefficients and the rms value of the lift coefficient for the flow around solid square cylinder.	129
Table 5.2	Base pressure coefficient and mean stream-wise velocity at $x/H=0.5$ on the centreline for the flow around leading-half porous square cylinder.	130
Table 5.3	Base pressure coefficient and mean stream-wise velocity at $x/H=0.5$ on the centreline for the flow around trailing-half porous square cylinder.	130
Table 6.1	Mean values of pressure coefficient for the solid bare square cylinder and square cylinders with porous materials at their trailing and leading halves. From left to right: pressure coefficient at the front point, pressure coefficient at the base point, minimum pressure coefficient in the wake. Results of Mínguez <i>et al.</i> (2011) for a solid bare cylinder is included as a comparison to the present work.	153
Table 6.2	The time-averaged drag coefficient and rms value of fluctuations in the lift coefficient for the flow around solid bare square cylinder and square cylinders with porous materials at their trailing and leading halves. Results of Mínguez <i>et al.</i> (2011) for a solid bare cylinder is included as a comparison to the present work	157

NOMENCLATURE

LIST OF SYMBOLS

A	Cross sectional area [m ²]
C	Quadratic loss coefficient
C_d	Drag coefficient
c_f	Skin friction coefficient
C_l	Lift coefficient
C_p	Pressure coefficient
$C_{p,b}$	Base pressure coefficient
$C_{p,f}$	Front pressure coefficient
D	Diameter of circular cylinder [m]
f	Frequency [Hz]
F_D	Drag force [N]
F_L	Lift force [N]
k	Turbulent kinetic energy [m ² /s ²]
L	Distance [m]
L_r	Recirculation length [m]
P	Pressure [Pa]
Q	Volumetric flow rate [m ³ /s]
st	Strouhal number
t	Time [s]
u	Velocity component in the x direction [m/s]
u_c	Velocity component in the x direction on the centreline [m/s]
U_0	Free-fluid velocity [m/s]
U_τ	Frictional velocity [m/s]
v	Velocity component in the y direction [m/s]

$u'u'$	Normal Reynolds stress in the x direction [m^2/s^2]
$u'v'$	Shear Reynolds stress [m^2/s^2]
$v'v'$	Normal Reynolds stress in the y direction [m^2/s^2]
x, y, z	Cartesian coordinates
y^+	Non-dimensional wall adjacent cell distance
ε	Turbulent dissipation rate [$J/kg.s$]
κ	Permeability [m^2]
μ	Dynamic fluid viscosity [$N.s/m^2$]
ρ_p	Particle density [kg/m^3]
\emptyset	Porosity
τ_w	Wall shear stress [N/m^2]
ν	Kinematic viscosity [m^2/s]

ABBREVIATIONS

CFD	Computational Fluid Dynamics
PPI	Pore per inch
RANS	Reynolds Averaged Navier-Stokes
Re	Reynolds number
SST	Shear Stress Transport
TKE	Turbulent Kinetic Energy
URANS	Unsteady Reynolds Averaged Navier-Stokes

CHAPTER 1

INTRODUCTION

1.1 Background

A bluff body can be defined as an object that when situated in a fluid flow, the fluid does not fully follow the boundary of the object and hence the fluid is separated over a substantial part of the surface of the body. Bluff bodies are ubiquitous in nature and in human artefacts. Buildings, offshore structures and transportation vehicles such as cars, ships and airplanes, are some examples of bluff bodies in the engineering field. A bluff body provides considerable resistance and disturbance to a fluid flowing around it. Separation of the flow from the surface of a bluff object produces a region of disturbed flow behind the object called the wake. Instabilities may be triggered and augmented within the near wake leading to the formation and shedding of vortices in the wake region. The vortex shedding is responsible for the production of a resistance force in the opposite direction of the fluid, known as drag force. It also generates large fluctuating forces acting on the body. The fluctuating forces have the potential to create flow-induced vibrations and hence reduce the structural integrity of the body and amplify the acoustic noise.

To control the drag, vibration and noise, the sources causing the instabilities, i.e. the separated flow in the wake region and the dynamics of the vortex formation have to be controlled. Such control can be achieved by using different flow control techniques broadly classified as active and passive methods. Active control is typically achieved by making perturbations in the wake flow through some excitation mechanism, for example rotational oscillations of the body (Choi and Choi 2002), flow forcing (Naim *et al.* 2007) and blowing and suction of fluids through surfaces (Huang *et al.* 2004). Passive methods include making modifications to the surface by introducing roughness (Park *et al.* 2011), the use of riblets (Greidanus *et al.* 2015), changing the geometry of leading or trailing edges (Lyu and Azarpeyvand 2017) and so on. Passive methods have recently been the subject of many studies. These methods are preferred over active control methods due to the simplicity in their application, independence from an external energy source and relatively low cost.

1.2 Problem Statement

As discussed in the previous section, control of the flows over bluff bodies is an important area of fluid dynamics. Control of the flow over configurations having commonly used cross-sections has been extensively studied due to its practical importance in engineering (Siegel *et al.* 2006, Choi *et al.* 2008). Recently attention has turned to examining the effect of porous materials on the flow control (Geyer *et al.* 2010b, Rashidi *et al.* 2013, Showkat Ali *et al.* 2018). Porous materials have been applied on bluff objects to alter the boundary layer characteristics and regularise the flow. Evaluation of the effects of porous surfaces on the aerodynamic or hydrodynamic performance requires a correct prediction of the flow manner. A thorough literature review on the modification of bluff bodies with porous material is presented in Chapter 2.

The literature survey reveals that there is very limited work on flow over porous bluff bodies most of which has been done numerically. Much of the preceding work on this topic has been directed to covering a bluff body with a porous layer (Bhattacharyya and Singh 2011, Rong *et al.* 2011). The majority of these studies are on circular cylinders wrapped with a porous sheath (Liu *et al.* 2012, Naito and Fukagata 2012). In particular, the following gaps have been identified: experimentally determined benchmarks, three-dimensional numerical studies, investigation on the effect of porous treatment on different configurations and the effect of the disposition of the porous treatment on a particular configuration. Therefore, this thesis addresses the above mentioned gaps through developing a novel passive method to control the wake instabilities and therefore reducing the induced drag and vibrations.

1.3 Research Objectives

The main objective of this research is to control the flow around a bluff body by substituting a part of a solid body with a porous medium. The idea is to modify the shear forces in order to regularise the flow and to reduce the induced drag.

In this project, firstly the flow over bluff bodies of widely encountered cross sections, namely circular, square and rectangular are experimentally studied. The effect of porous material with a range of porosities on the flow structure in the wake of cylinders are investigated. Subsequently, simulations are performed over three-dimensional solid and porous square bluff bodies. Comparisons with the experimental results and previous work will serve to refine and validate the chosen numerical method. Studying the formation of the boundary layer form an integral component of the study. Knowledge of the boundary layer formation is critical for drag control.

In summary, the specific aims of this project are:

1. Perform experiments on the flow over solid and porous bluff bodies over a range of parameters including the physical characteristics of porous media and geometries.
2. Evaluate and validate a numerical method for simulating the flow over porous bluff bodies.
3. Perform simulations to investigate the effect of disposition of the porous medium on the boundary layer, drag coefficient and flow structure in the wake of porous bluff bodies.

1.4 Research Methodologies and Techniques

To achieve the objectives enumerated in section 1.3, a step-by-step approach was followed in this research. These steps are summarised in the following.

- **Step 1 - Literature review on passive flow control by means of porous material**

A broad literature review on the use of porous materials for different configurations of bluff bodies has been completed. The review assisted in achieving a holistic view of the existing knowledge as well as the problems and challenges. Firstly, the mathematical formulations governing the flow through and over porous materials have been identified. Next, the existing numerical approaches for the simulation of the flow over porous bodies have been analysed. Finally, the experimental attempts to study the flow over bluff bodies treated with porous material have been reviewed. The effect of porous material characteristics and the location of the material on the flow control of bluff bodies was overviewed in detail. The recent research work concerned with the porous material selection and application with the aim of flow control, particularly drag and noise reduction have been investigated in detail. Moreover, the review of the

literature focused on knowledge gaps yet to be addressed and possible future work in this field of porous flow control.

- **Step 2 – Performing experiments on solid and porous-treated bluff bodies**

Following the investigations of the literature concerned with the use of various porous materials on bluff body configurations, three configurations have been selected for the experimental studies. Circular cylinders were to be covered with a porous sheath, while porous sheaths would replace the downstream halves of the square and rectangular cylinders. Prototypes of the proposed porous-coated bluff bodies were developed based on the characteristics of the system discovered in the literature review. The bluff bodies were selected to be fabricated from aluminium material. The porous media consisted of open cell polyurethane material, selected with three permeabilities. The total size of the prototypes remained the same in all the experiments. In the first set of experiments, the flow over bluff bodies completely consisted of aluminium was investigated. In the second set of experiments, half the size of the bluff bodies consisted of aluminium and the other half was composed of porous material of a distinct permeability.

PIV was selected to measure the mean velocity and turbulence properties due to its non-invasive nature and ability to capture the whole wake domain without any disturbance. The experiments were conducted in a closed-circuit wind tunnel. The mean velocity of the air entering the working section of the tunnel was 20 m/s, corresponding to a Reynolds number of about 53000, based on the diameter or height of the cylinders. The prototypes were made to occupy not more than 6% of the test section to prevent blocking of the flow. The air was seeded with particles of sufficiently small sizes. A cross correlation camera was used to obtain instantaneous images of the flow. The images obtained from the camera were used to determine the values of the mean velocities in the

wake of the cylinders using an adaptive cross-correlation method. The results were used to determine the flow field in the wake of the bluff bodies as well as velocity profiles and Reynolds stresses.

- **Step 3 –ANSYS simulation modelling the bluff bodies treated with porous media**

Once the experimental investigations on the application of porous media to three configurations was completed, further investigations have been performed through numerical studies. Due to the extensive numerical studies on circular cylinders covered with a porous layer, this configuration was not considered for numerical investigations in this work. Moreover, according to the experiments, similar effect of porous material has been observed for the square and rectangular cylinders. Therefore, the studies was continued on the square cylinder to obtain a deeper understanding of the flow in the presence of porous material beyond what has been obtained from experiments.

Among the porous materials used in the experiments, the highest effect on the flow control has been achieved with the highest permeability material. Therefore, the material with the highest permeability was employed in the simulations to show more tangible differences between the flow over the solid cylinder and porous-treated cylinder. Research has been dedicated to investigate the effects of the location of porous layer on the flow structure and aerodynamic performance of the bluff bodies. For this purpose, the system was modelled and simulated using ANSYS CFX. Three-dimensional studies of the bluff bodies were conducted using a structured grid.

The project models the physics of fluid flow in the unobstructed region, in the porous medium and around the solid body. The flow in the unobstructed region is described by the Navier-Stokes equations, a system of nonlinear partial differential

equations, which are typically intractable to analytic techniques. The Navier-Stokes equations describe the momentum of the fluid, which is a balance between external forcing, internal inertial effects, and internal dissipative effects. To consider the details of the flow through the pore structure of porous media is computationally infeasible. Therefore, a numerical solution to the problem is sought, so that the flow behaviour in the three regions can be accurately described. Coupling the Navier-Stokes equations with Darcy or Brinkman equation, representing the porous material, is one method. However, accurate modelling of the interface between the fluid and porous material is still an unsolved challenge in this method. The volume penalisation is another method, which is easy to implement and overcomes the difficulties of coupling the equations governing fluid flow in the unobstructed and porous regions.

A volume penalization method was used in this study to simulate the fluid flow over porous-treated square cylinders. The method included the Navier–Stokes equations with an extra term representing porous material in the porous domain. Continuity in the velocity and stresses were assumed at the interface of the porous and fluid domains. The Reynolds Averaged Navier-Stokes (RANS) modelling was used as the turbulence model. The numerical model was validated through comparison of the results with the experiments for all the uncontrolled and controlled cases and the previous available data in the literature for the uncontrolled square cylinder. Three cases have been studied, a bare square cylinder, a square cylinder with its trailing half consisted of porous material and finally a square cylinder with porous material comprised its leading half. A comprehensive study over the three cases have been performed with a focus on the velocity profiles near the porous surfaces in particular in the boundary layer and the derivation of drag force. The flow field and vorticity and pressure distributions were

determined. In addition, velocity profiles around the obstacles and in the near wake and far wake have been presented.

1.5 Research Contribution to Knowledge and Statement of Significance

1.5.1 Academic Contribution

The contribution of this project to knowledge is that it provides a step towards understanding the flow over bluff bodies modified with porous materials. In studies on fluid flow over porous-treated bluff bodies of basic geometries, the porous treatment is commonly considered as a cover on the bluff body (Takeshi *et al.* 2010, Rashidi *et al.* 2013). The novelty in the present work is that new porous treatments have been considered in which regions of solid cylinders were replaced by porous materials. The significance of this project is that it extends previous studies by considering the effect of the replacement of a part of a bluff body with porous materials, which determines the efficacy of the porous treatment in the control of flow over bluff bodies. The transport of fluid flow around uncontrolled and controlled bodies of circular, square and rectangular cross-sections is examined by conducting a series of experiments. In the experiments, the effect of porous layer permeability, on the topology of the flow field and downstream velocity and turbulence distribution is investigated.

It is also important to understand the formation of boundary layer in order to model large scale flows and devise practical means of reducing the parasitic drag of objects immersed in the flow. However, only preliminary studies have been conducted into porous media surface coatings (Bruneau and Mortazavi 2004). The numerical simulations performed in this research will provide further understanding of the flow dynamics associated with applying a porous layer to a bluff body. The results will deepen our understanding of boundary layer formation over surfaces to include porous coatings.

Furthermore, the position of the porous material on a square cylinder is changed from being the trailing edge to the leading edge and the effect of such disposition on a range of phenomena related to flow control is examined. The phenomena include the flow field, vorticity and pressure distribution, the flow field structures adjacent to the porous layer and within the boundary layer and downstream velocity and turbulence. The effect of different arrangements of porous layer on the drag force is also investigated.

Overall, this research contributes to existing knowledge because it:

- Provides experimental data and a mathematical model on a novel porous treatment for different configurations of bluff bodies. It is anticipated that the experimental data will be very useful to theoreticians and numericists who are required to evaluate their mathematical models.
- Demonstrates how the permeability of porous media affects the flow fields around the bluff bodies that have been studied. This is important because it is one of the key variables over which designers and research have control.
- Provides for the first time the importance of the physical configuration of porous media on bluff bodies. For example, it is shown that the flow fields developed over bluff bodies that have been modified by placing porous media on their leading edge are significantly different from those on which porous media form their trailing edge.
- The work provides a rich source of data and deep insights into the nature of the wake downstream of bare and porous coated bluff bodies immersed in turbulent flows.

1.5.2 Practical Contribution

Fuel consumption of transportation vehicles is directly proportional to the drag coefficient (Browand 2005). Porous media have the capacity to reduce the drag coefficient and hence the judicious use of porous media has the capacity to reduce fuel consumption. A large component of the fuel consumption of a vehicle arises in overcoming the aerodynamic drag, particularly in the case of large vehicles travelling at high speeds. For example, about 20% of fuel in a medium-size sedan is consumed to overcome aerodynamic drag at 100 km/h and this amount can increase to 50% for a heavy commercial vehicle (Wang *et al.* 2016). A reduction in aerodynamic drag by 15% at highway speed of 88 km/h can lead to a saving in fuel by about 5 to 7 % (Browand 2005, Bellman *et al.* 2010). In addition, fuel consumption by ground vehicles accounts for over 30% of CO₂ and other greenhouse gas emissions (Sudin *et al.* 2014). Therefore, a reduction in the aerodynamic drag is significant to improve the fuel economy and reduce greenhouse gas emissions. In this regard, a novel method is proposed to control fluid flows over the vehicles. Currently the technologies and approaches employed for the purpose of drag reduction are expensive and not necessarily efficient. The current approach used on, for example road vehicles, is to streamline the overall shape of the bluff body (Minguez *et al.* 2008). Streamlining reforms all the blunt, angled surfaces of the body to smooth, more gradually changing surfaces so that the fluid can easily flow over the body. The detached flow imposed to vehicles can be decreased by such transformation. However, dynamic stability will be negatively affected and complexities will be added to the model.

This project addresses these problems by introducing a novel aero-dynamical or hydrodynamical design. The hypothesis is that replacing a part of a bluff body with a

porous medium will decrease the drag forces by creating an intermediate flow, which reduces the shear forces. The porous coating can remove the problems caused by the existing flow control methods such as instability and complicated design. Apart from fuel consumption, lifetime of vehicle is of high importance. Fluid flow over the bluff body imposes forces against the direction of the body leading to erosion and decrease the lifetime of the object (Lienhart *et al.* 2002). Taking advantage of the proposed treatment, wear and tear diminishes the degree of decay and deterioration, which in turn increases the lifetime of the devices and reduces costs.

1.6 Thesis Structure

Chapter 1 presents an overview of the thesis, its objectives, research methodology and contribution to the knowledge. Chapter 2 provides a comprehensive literature review with regard to the application of passive methods, in particular porous media to control the flow over bluff bodies. A literature review is conducted to reinforce the background of the problem, refine the research questions and explore previously applied methodologies. The mathematical models of flow over porous objects are reviewed to distinguish their differences, advantages and deficiencies. Methods for approximating the solution of the equations of fluid flow through porous media are explored. Existing data from peer-reviewed articles is collected to describe the physics of the problem and for validation purposes. Existing numerical procedures are investigated identifying their efficacy to predict the behaviour of the fluid flow. The numerical models that have been used for the simulation of the problem and their strengths and limitations are reviewed. Finally, experimental investigations, methods of conducting experiments and materials used are studied. Correspondingly, the gaps in the existing knowledge and potential research directions for future development in this field are identified.

Following the literature review and the detection of the research field, Chapter 3 provides details on the experimental procedure and fundamentals of the experimental method. Details of the bluff body configurations, namely circular, square and rectangular cylinders, characteristics of porous materials and equipment used are described. Chapter 4 contains the results of the experiments, including the velocity field and flow structures in the wake of the cylinders not treated with porous material. In addition, the results of the porous treated configurations are presented in comparison with the solid bare cases. The chapter also includes a full discussion on the effects of different porous materials on the flow structure.

Based on the results obtained from the experiments, the square cylinder was selected for further investigations through numerical modeling. The details of the numerical procedure, the mathematical formulations and the positions of the porous material is presented in Chapter 5. The system is simulated using ANSYS CFX, a commercial CFD package. The simulation procedure selected based on the capability of the method in accurate modelling of the problem. Chapter 5 also gives the results of the simulation work in the steady state condition undertaken to evaluate the capability of the proposed model in estimating and calculating the flow characteristics over porous-treated bluff bodies. Validation studies have been carried out using the experimental results presented in Chapter 4. The unsteady simulations of the flow around square cylinders are given in Chapter 6. The unsteady results for the bare square cylinder are compared with published numerical work to validate and confirm the numerical method in correctly simulating the flow over bluff bodies. Upon validating the numerical model, the bare and porous-treated square cylinders are further investigated in Chapter 6 to obtain a full understanding of the flow structures and drag forces. Finally, Chapter 7 summarises

the whole research work, highlights the contributions made and draws the conclusions. Possible future research opportunities are discussed.

CHAPTER 2

LITERATURE REVIEW ON FLOW CONTROL OVER BLUFF BODIES USING POROUS TREATMENT

2.1 Introduction

Bluff, non-streamlined, bodies are ubiquitous in nature. They include buildings, communications towers, dampers in air conditioning valves, air conditioning registers for admitting and ejecting air from rooms, motor vehicles, components in heat exchangers, chemical reactors and so on. Flow over bluff bodies immersed in a fluid has motivated considerable research for decades. The problem arises when the body moves relative to the fluid, and vortices are generated in the wake downstream of the body. The vortices increase induced drag forces, which act in the direction opposite to the relative motion of the body. Drag forces can give rise to large unsteady forces that have the potential to reduce the structural integrity of the bluff body or to decrease its hydro-dynamical or aero-dynamical effectiveness.

The flow separation from a bluff body results in the formation of a pair of alternate eddies on the either side of the body, which travels into the wake region causing the so-called Karman vortex shedding. The wake behaviour in a bluff body flow and vortex shedding has been widely studied due to its importance in practical applications such as in the calculation of aerodynamic forces around airfoils or in the estimation of the vortex

shedding frequency when designing offshore structures. Roshko (1954) was the first to measure the period of Karman vortex shedding behind a bluff body after whom many researchers investigated the vortex shedding and near-wake flow. Gerrard (1966) has described the mechanism behind the formation of vortex streets for short bluff bodies such as circular and square cylinders. He discusses that alternate vortices in the wake of the bodies are formed as a result of the interaction of the separated shear layers when drawing into the growing vortex. This idea was later verified through the experiments of Green and Gerrard (1993). The studies regarding the vortex shedding in the wake of bluff bodies are extensively analysed in the literature, for example, reviewed by Lin and Pao (1979), Bearman (1984), Oertel (1990), Coutanceau and Defaye (1991), Griffin and Hall (1991), Williamson (1996), Williamson and Govardhan (2004).

Among the types of bluff objects studied in fluid dynamics research, cylindrical bodies have been the topic of particular attention. Cylinders with circular, square and rectangular cross sections have been investigated in order to understand the fundamental physics involved in the dynamics of the wake. The wake of a fluid passing a cylinder exhibits distinct behaviours depending on the cross-section of the cylinder and the flow Reynolds number (Re), which represents the ratio of inertia force to viscous force in the flow. For a cylinder with a circular cross-section, in very low Reynolds numbers ($Re < 5$), the incoming flow tends to follow the curvature of the cylinder, known as laminar flow. By increasing the speed of the flow, separation of the boundary layer occurs at a point along the cylinder due to the adverse pressure gradient imposed by the cylinder divergent geometry (Jorgen and Mutlu 1997). The flow then rolls up into swirling eddies, leading to periodic shedding of vortices in the wake region of the body known as the von Karman vortex street. There is no fixed separation point for the flow around a circular

cylinder. The separation point changes according to the conditions of the incoming flow and the boundary layer developed on the surface of the cylinder.

Different flow regimes have been defined for a circular cylinder based on the Reynolds number, where the flow experiences boundary layer transitions (Williamson 1988, Schewe 2006, Sumer and Fredsøe 2006). For Reynolds numbers from zero up to 3×10^2 , the flow undergoes a transition from being very attached to the surface to a periodic laminar wake, where vortex shedding forms. In Reynolds numbers between 3×10^2 and 2×10^5 the flow is sub-critical, where the laminar wake is replaced by turbulent instabilities with an almost unchanged wake topology in this range. The wake at the sub-critical regime is fully turbulent while the boundary layer remains laminar. The critical regime occurs in Reynolds numbers from 2×10^5 to 3.5×10^5 with major changes in the flow structure, such as the emergence of asymmetries in the wake and an abrupt reduction in the drag coefficient. The flow is super-critical when the Reynolds number lies between 3.5×10^5 and 1.5×10^6 , at which the flow recovers its symmetry in the wake and the drag coefficient remains almost unchanged throughout the entire range. Higher Reynolds numbers put the flow in a post-critical regime. A comprehensive review of the above regimes can be found in Zdravkovich (2003).

In contrast to circular cylinders, the flow separation point is located at the upstream corners of the cylinders with square and rectangular cross-sections. For a square cylinder, at low Reynolds numbers from 49 to 150, a stable regime with laminar 2-D vortex shapes is generally created in the wake of the cylinder (Davis *et al.* 1984, Williamson 1988, Roshko 1993, Williamson 1996). A transition regime is observed at Reynolds numbers between 150 and 300, when 3-D rib-like vortex shedding forms (Barkley and Henderson 1996, Brede *et al.* 1996, Thompson *et al.* 1996, Henderson 1997, Robichaux *et al.* 1999).

Higher Reynolds numbers induces an irregular regime with velocity fluctuations showing distinct irregularities in the cylinder wake (Roshko 1954, Bloor 2006). A schematic of the above regimes for the circular and square cylinders is illustrated in Figure 2.1.

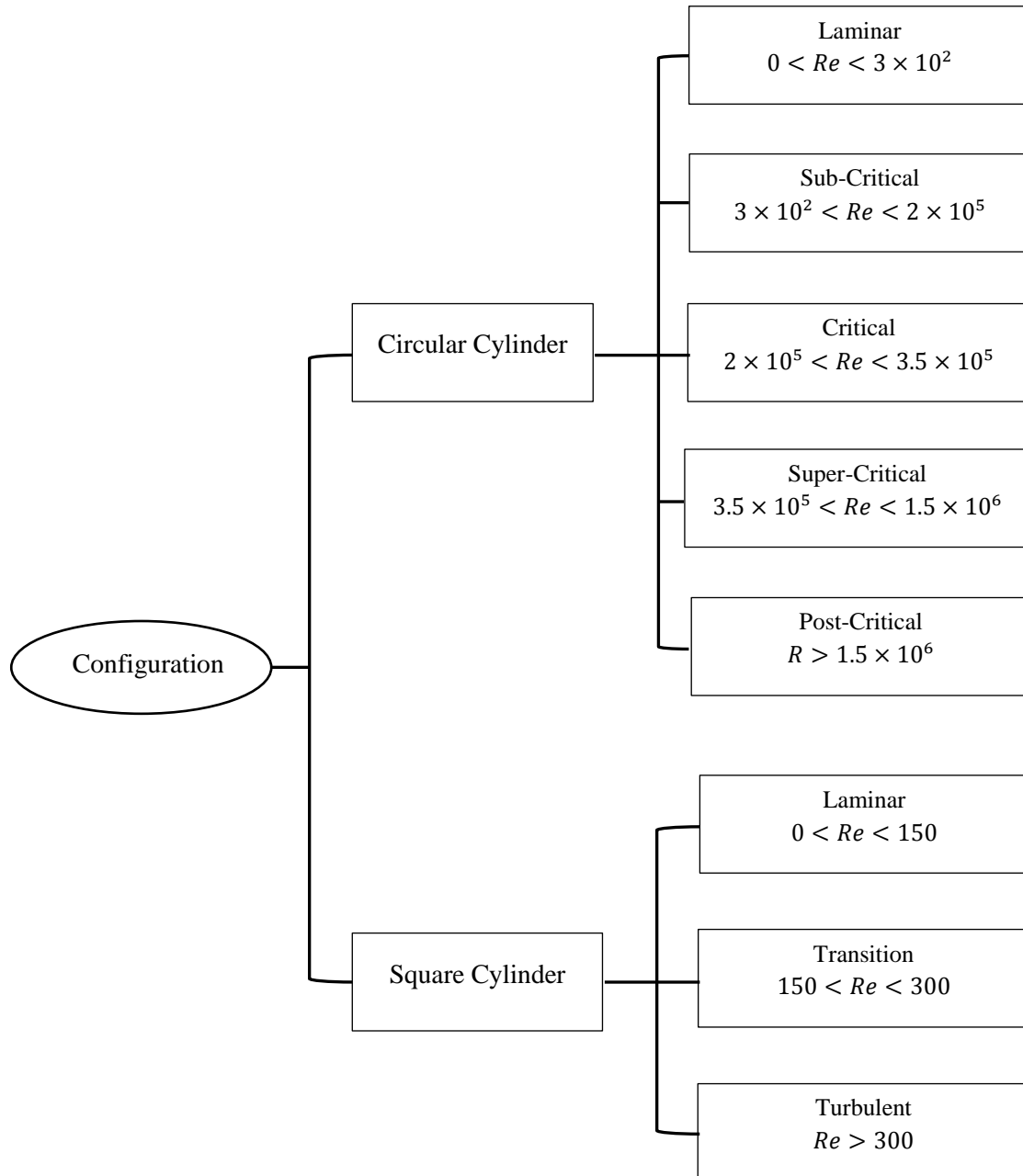


Figure 2.1. A schematic of the different flow regimes for circular and square cylinders

The aspect ratio (L/H) in a rectangular cylinder, where L is the width along the direction of flow and H is the height of the cross-section, plays an important role in determining the vortex formation and the hydrodynamic forces on the body. The aspect ratio and the flow Reynolds number determine whether the flow over the rectangular cross section is separated or reattached, which depends on the reattachment of the shear layer on the surfaces of the cylinder parallel to the free-stream flow hereinafter called side surfaces (Okajima 1982). In the separated flow case, the flow separates at the upstream edge of the cylinder and remains separated along the side surfaces, i.e. no reattachment happens for the shear layer. Therefore, the separation bubble covers the entire side surface. In the reattached case however, the flow reattaches to the surface at a certain point along the side surfaces with a possibility of another separation further downstream the sides. For an aspect ratio equal to $L/H=2$, Okajima (1982) found that the flow undergoes a transition from a reattached to a separated condition at a Reynolds number around 500 based on the free stream velocity and the height of the rectangular cylinder. However, at higher aspect ratios, the transition from an attached condition to a separated one may occur at higher Reynolds numbers or the flow remains reattached to the side surfaces. The study of the flow over rectangular cylinders with different side ratios and over a range of Reynolds numbers can be found in the literature for example, studies in the range of $1 < L/H < 4$ and $70 < Re < 2 \times 10^4$ by Okajima *et al.* (1990), $0.6 < L/H < 8$ and $Re = 2.2 \times 10^4$ by Shimada and Ishihara (2002) and $2 < L/H < 3$ and $Re = 2 \times 10^3, 2 \times 10^4$ by Kuroda *et al.* (2007).

Based on the above discussion on the formation of vortex streets, it is expected that a change in the separated shear layers significantly affect the characteristics of vortex street. Persistence of vortex shedding is the main issue in the flow control. Therefore, the

idea of shear layers alteration has been widely applied in the control of flow over bluff bodies. Examples of such alterations are the use of roughness on the surfaces (Park *et al.* 2011), serrations (Shi *et al.* 2012) and a secondary control cylinder (Liu *et al.* 2015). An extensive review of the studies with the aim of changing the vortex street to decrease the drag force and fluctuating lift force can be found in the work of Choi *et al.* (2008).

2.2 Flow Control Techniques

The fundamental occurrence of flow over bluff bodies and the problem of attenuation of vortex shedding, lift and drag fluctuations and noise generation have been an important subject of study for years (Fink and Bailey 1980, Robinson 1991, Choi and Choi 2002, Naito and Fukagata 2012). Efforts have been made to modify and suppress vortex shedding by means of various control methods such as active and passive techniques. Passive methods have been a recent focus of attention to control the flow over bluff bodies and reduce drag due to their relative simplicity, durability and less cost compared to active methods. In passive methods, flow is manipulated by the changes in the geometry of the body without using extra energy. The use of compliant walls that mimic the properties of the skins of dolphin (Carpenter *et al.* 1999, Wiplier and Ehrenstein 2000), riblets (Walsh 1983, Robinson 1991, García-Mayoral and Jiménez 2011, Greidanus *et al.* 2015), rough surfaces (Park *et al.* 2011) and splitter plates (Vu *et al.* 2016, Sarioglu 2017) are examples of passive methods.

Recently, the application of a porous coating to the body has been investigated (Bruneau and Mortazavi 2004, Bhattacharyya and Singh 2011). Reports on the advantages of using porous materials to control boundary layers show that porous coating treatment can significantly reduce the energy of the vortices, hence decrease the pressure fluctuations on the surface of the bluff bodies (Jiménez *et al.* 2001, Hahn *et al.* 2002).

Reduction of pressure fluctuations allows the flow to penetrate the pores, which promotes local blowing and suction (Choudhari and Khorrami 2003). The flow leakage across the porous surface modifies the local mean flow structures. The use of porous material is not restricted to the flow control. It is also used for the enhancement of heat transfer (Liebenberg and Meyer 2007). There has been considerable published research in the field of convection heat transfer within porous media (Perng *et al.* 2011, Sauret *et al.* 2014, Rees 2015). The wide range of published work (for example Pop and Ingham 2001, Vafai 2005, Nield and Bejan 2014, Hooman *et al.* 2017) indicates the level of understanding of momentum and heat transport in porous media.

2.3 Mathematical Formulations for Porous Materials

Porous materials or porous media form a class of materials containing voids or pores, typically filled with a fluid. Porous media can be found everywhere from rocks and soils to woods and bones and manufactured materials such as cements or foams. Porous materials are generally characterised by their porosity (\emptyset), which is an indication of the ratio of the pore volume to the total volume of the material and assumes a value between 0 and 1. Porosity has a significant impact on the mechanical, physical, and chemical properties of the materials. Other basic parameters related to the pores such as the pore size, shape, and surface area have indeed an important role in the functionality of a porous media. The ability of a porous material to pass a fluid through is determined by a parameter called permeability (κ). The SI unit of permeability is m^2 , but darcy is also sometimes used, which is mainly applied in petroleum engineering. A permeability of 1 darcy is equivalent to a permeability of $9.869233 \times 10^{-13} \text{ m}^2$, generally approximated as $1 (\mu\text{m})^2$. The Darcy number (Da) is another parameter used to introduce porous materials,

which is a non-dimensional quantity defined as the permeability over the square of a characteristic length, usually particle diameter,

$$Da = \frac{\kappa}{d^2}. \quad (2.1)$$

Porous materials are also known with other properties, which are governed by the geometrical and mechanical properties of the material. Such properties include tortuosity, thermal permeability, thermal viscous characteristics, surface roughness and so on (Lu et al. 1999). Porous media arise in many areas of science and engineering such as filtration, geo-mechanics, petroleum engineering, biology and material science. Porosity and permeability of porous materials have been demonstrated to be the most important parameters for flow-porous vortex structure interaction when porous materials are used as a mean to control the flow around bluff bodies (Rashidi et al. 2013, Showkat Ali et al. 2017). Fluid flow through porous media has attracted considerable research over the last few decades and many formulations have been developed to explain and quantify the flow through porous materials. The formulations are presented in sections 2.3.1 and 2.3.2.

2.3.1 Darcy's Law and Brinkman Model

Darcy was the first who determined a model to describe the flow through a porous medium known as Darcy's law. In the Darcy model, the flow discharge rate is proportional to the pressure gradient via the relation (Bear 1972, Rajagopal 2007):

$$\frac{\mu}{\kappa} U = -\nabla p, \quad (2.2)$$

where, U is the superficial velocity inside the porous medium, ∇p is the pressure gradient along the porous material, μ is the viscosity of the fluid and κ is the permeability of the porous medium. Darcy's law is valid for laminar flow through sediments. The Darcy model is a simple model and has hitherto been the most widely used model for porous material flow.

Brinkman added an effective viscosity term to the Darcy model to combine the Darcy flow and viscous Stokes flow (Brinkman 1947) as,

$$\frac{\mu}{\kappa} U = -\nabla p + \tilde{\mu} \Delta U, \quad (2.3)$$

with $\tilde{\mu}$ representing the Brinkman effective viscosity. The Brinkman model makes it possible to retain continuity of the velocity profile at the interfaces of porous media that may have permeabilities in the range $0 \ll \kappa \ll \infty$.

2.3.2 Darcy–Forchheimer Law

For flows in porous media with Reynolds numbers greater than 1, the significance of inertial effects has to be taken into account, as the fluid velocity in the pores becomes significant (Vafai and Tien 1981). Therefore, an inertial term, known as the Forchheimer term, has been added to the Darcy's equation, which accounts for the non-linear behaviour of the pressure gradient. The Darcy-Forchheimer model reads (Bejan 1984)

$$\frac{\mu}{\kappa} U + \frac{\rho}{\kappa_1} U^2 = -\nabla p, \quad (2.4)$$

where κ_1 denotes inertial permeability. It was shown by Costa *et al.* (1999) that the Forchheimer model remains valid for sufficiently high Reynolds number when they studied the effect of inertial forces on the flow behaviour in highly porous structures. The authors showed that the model is valid even when convective non-linearities affect the momentum transport at the pore scale. Fourar *et al.* (2004) also demonstrated that the Forchheimer model can reasonably describe the flow at high Reynolds numbers after a critical value from which Darcy's law is no longer valid.

2.4 Porous Treatment for Different Configurations

Flow around and through porous materials has been extensively studied over the past two decades to understand the underlying physics behind it. Development of mathematical formulations to capture the interface conditions between the porous media and fluid (Vafai and Kim 1990, Chan *et al.* 2007), and the effects on aerodynamic forces and wake structure (Zhao and Cheng 2010, Valipour *et al.* 2014) are examples of such studies. The use of porous media as a mean for flow control has recently attracted many studies with application from basic geometries, e.g. circular and rectangular cylinders to more complicated geometries such as airfoils. Porous materials have been used in different forms for example in a shape of a ring around a circular cylinder or as sections at the trailing edge of a blunt surface. Porous materials of different characteristics mainly made of metals or foams have been used. In this section, the configurations in which porous material has been applied and the flow control has been studied by researchers are presented.

There is a series of research on the flow around and through configurations solely comprising porous material. Examples are studies on a porous circular cylinder (Noymer *et al.* 1998, Bhattacharyya *et al.* 2006, Peng *et al.* 2011), a porous square cylinder with zero angle of incidence (Jue 2004, Bhattacharyya *et al.* 2006, Chen *et al.* 2008, Yu *et al.* 2010), a porous square cylinder with an angle of incidence equal to 45° (Valipour *et al.* 2014), porous trapezoidal cylinder (Chen *et al.* 2009) and a porous sphere (Neale *et al.* 1973, Adler 1981, Peng *et al.* 2012). Moreover, flow over configurations in which porous material formed a component of their structure has been investigated. The widely studied configurations and the porous materials applied are summarised in the following subsections. This section aims at providing an overview of the present porous treatments for the control of flow over bluff bodies, the different configurations used and the available data. A comprehensive discussion on the studies is presented in sections 2.5.1 and 2.6.

2.4.1 Circular Cylinders

Circular cylinders are the most studied configurations with the application of porous material in which a porous ring is applied on the cylinder as illustrated in Figure 2.2. Porous covers with various thicknesses have been applied to cylinders of different diameters over a range of Reynolds numbers. The porous cover has been generally replaced a certain thickness of the solid material such that the total diameter remained the same, for example the work of Zhao and Cheng (2010) and Rashidi *et al.* (2013). However, in some studies, the cover was added to the base cylinder, for example the work of Bruneau and Mortazavi (2008) and Khashehchi *et al.* (2014). It must be noted that the addition of a porous cover will add to the total diameter of the cylinder. The increase in the diameter changes the behaviour of the flow even in the absence of the porous material.

Therefore, the changes reported in the flow statistics are not the sole result of applying the porous cover.

Some of the studies regarding porous-covered circular cylinders directed at the control of the flow are listed in Table 2.1. The method on which the study has been performed including numerical and experimental, the operating flow Reynolds number (Re), the ratio of the thickness of porous cover to the diameter of bare cylinder (h/D), and a parameter related to the porous material pointed in the corresponding study are presented. The permeability coefficient (K) used in the work of Bruneau and Mortazavi (2008) is the non-dimensional coefficient of permeability based on the permeability of the porous material (κ), porosity (\emptyset), flow mean velocity (U), kinematic viscosity of the fluid (ν) and the height of the domain (H^*).

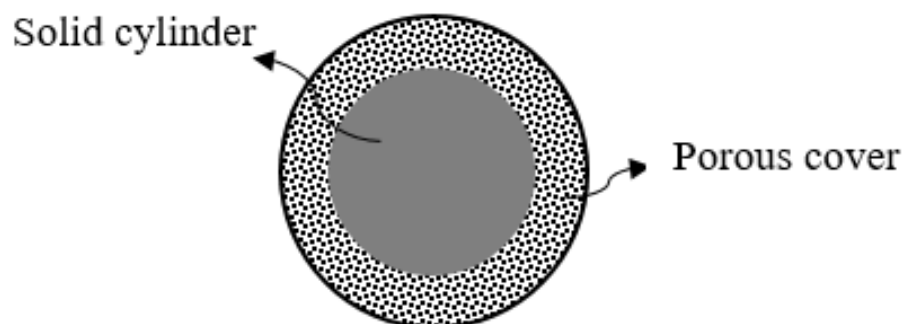


Figure 2.2. A circular cylinder covered with a sheath of porous material.

Table 2.1 Compilation of the studies on the use of porous materials for flow control of a circular cylinder. The method of the investigation, flow Reynolds number (Re), the ratio of the thickness of the porous cover (h) to the diameter of the cylinder (D) are presented.

Reference	Re	Method	h/D	Porous material parameter
Bruneau and Mortazavi (2008)	2.4×10^3 2.4×10^4	Numerical	0.125	$K = \frac{\kappa \phi U}{\nu H^*} = 10^{-1}$
Zhao and Cheng (2010)	$10^3, 2.5 \times 10^3$ 0.5×10^4	Numerical	0.02, 0.1, 0.2, 0.4	$10^{-4} \leq Da \leq 10^{-1}$
Takeshi et al. (2010)	8.3×10^4	Experimental	0.4	$\phi \geq 0.97$
Bhattacharyya and Singh (2011)	$40 \leq Re \leq 200$	Numerical	0.1, 0.25, 0.5	$10^{-5} \leq Da \leq 10^{-2}$
Naito and Fukagata (2012)	$10^2, 10^3,$ $3.9 \times 10^3, 10^5$	Numerical	0.2, 0.5	$10^{-3} \leq Da \leq 1$
Liu et al. (2012)	9.3×10^4	Numerical		$0.75 \leq \phi \leq 0.97$
Rashidi et al. (2013)	$Re \leq 40$	Numerical	0.1, 0.3, 1, 5, 10, 20	$10^{-8} \leq Da \leq 10^{-1}$
Khashehchi et al. (2014)	$10^3 \leq Re \leq 10^4$	Experimental	0.187	$0.4 \leq \text{Pore size} \leq 3$
Showkat Ali et al. (2017)	$6.7 \times 10^4 \leq Re \leq$ 3.9×10^5	Experimental	0.166, 0.5	$\kappa = 3.93 \times 10^{-6},$ $6.44 \times 10^{-6} \text{ m}^2$

From Table 2.1, it can be clearly seen that experimental studies are exiguous. In addition, the majority of studies has been performed in the sub-critical regime with a few studies in the laminar and super critical regimes. Various thicknesses of porous covers have been applied, ranging from a thickness of 0.02 up to a large value of 20 times the cylinder thickness. There is no consensus among the studies on the effect of porous covers on the drag coefficient of a circular cylinder and Reynolds number has no role in this

discrepancy. In some studies, the drag coefficient is found to be inversely related to the porous cover thickness (Bruneau and Mortazavi 2008, Bhattacharyya and Singh 2011), while others reported an increase in the drag coefficient (Zhao and Cheng 2010, Showkat Ali *et al.* 2017). However, the effect of porous thickness on the flow structures found to be dependent on the flow Reynolds number and properties of porous materials. For example Zhao and Cheng (2010) investigated the reduction in lift coefficient in a range of Reynolds numbers and Darcy numbers and found that there is a critical Darcy number at which the lift coefficient is minimum. The critical Darcy number is found to be dependent on the Reynolds number, the porous layer thickness and Forchheimer coefficient. It can be inferred that a parametric study is only beneficial when porous material is applied in a particular application to achieve the optimum parameters of interest.

2.4.2 Square and Rectangular Cylinders

Among other geometries of cylinder, square and rectangular cylinders have also been treated with porous material in limited studies. Again, a porous cover has been applied around the cylinders (Figure 2.3 (a)) or in some cases layers of porous material have been applied on the surfaces of the cylinders (Figure 2.3 (b)) for the purpose of flow control. In the numerical work of Bruneau and Mortazavi (2004) the flow over a porous-covered square cylinder at Reynolds numbers equal to 300, 3000 and 30000 has been investigated. Various thicknesses of porous materials (h) to a square cylinder of the size (H) at a range of $h/H = 0.025, 0.05, 0.1$ and 0.2 has been used. Porous materials used had a permeability coefficient equal to $\kappa = 10^{-2}, 10^{-1}$ and 1 . A reduction of 30% in the drag forces was reported. However, the study is two dimensional, while the nature of the flow

is three-dimensional, therefore the reported value may not be reliable. The authors also used porous layers for a rectangular cylinder on the surfaces parallel to the free-stream flow (Bruneau and Mortazavi 2008). They used a ratio of $h/H = 0.05$ and 0.1 , where (h) is the thickness of the porous layer and (H) is the size of the rectangle side perpendicular to the incoming flow. Their numerical investigations have been performed at the same Reynolds numbers as their previous work and over a range of permeability coefficient to conduct a parametric study. However, they only reported a regularisation in the flow by presenting lift coefficient and a vorticity parameter. The evolution of the wake structures and the mechanism of such regularisation have not been studied. Moreover, in both studies the manipulation of the interface of porous material and fluid flow has not been discussed.

In another numerical investigation by Rong *et al.* (2011), porous covers have been used around a square cylinder at Reynolds numbers between 20 and 200. A Darcy number range of 10^{-6} to 10^{-2} has been used for the porous covers at $h/H = 0.1, 0.15$ and 0.2 . The study showed a dependency of drag and lift coefficients on Darcy number. Again, no data on the velocity components and turbulent intensities in the wake of the cylinder were presented. More recently, Showkat Ali *et al.* (2016) experimentally investigated the same topic of the effect of porous covers around square cylinders. They used two different porous materials having permeabilities equal to $\kappa = 3.93 \times 10^{-6}$ and $\kappa = 6.44 \times 10^{-6}$ with a ratio of $h/H = 0.166$ and 0.5 . The flow was examined at Reynolds numbers from 6.7×10^4 to 3.9×10^5 to discover the optimum parameters for the best flow control. This study presents data on the drag and lift coefficients as well as velocity profiles in the stream-wise and cross-wise directions in the wake region. Here again, a reduction in the drag and lift coefficients and a stabilisation of the near wake flow was demonstrated. The energy

content and Reynolds shear stress components are also presented qualitatively, but not quantitatively. Therefore, the reported reduction in the energy content and stresses cannot be quantified.

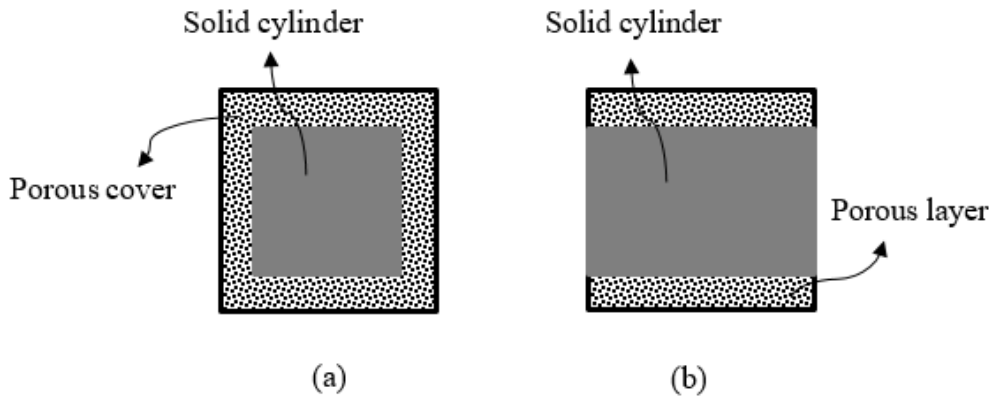


Figure 2.3. The location of the porous treatment on a square and rectangular cylinder commonly used in the literature. (a) a porous cover around a square cylinder, (b) porous layers around a rectangular cylinder.

2.4.3 Configurations with Blunt Trailing Edges

Porous treatments have also been used to reduce noise from airfoils. The noise from an airfoil is generated as a result of the interaction of the airfoil boundary layer with the airfoil components, such as the trailing-edge and wing-tip (Brooks *et al.* 1989) as well as airfoil bluntness and flow separation from the airfoil surface. Substantial research has been directed towards the application of porous materials for the reduction of airfoil trailing-edge noise. An example is replacing a part of the blunt trailing edge of a flat plate, representing an airfoil, with porous materials. A schematic of such treatment is shown in Figure 2.4, extracted from Showkat Ali *et al.* 2017, in which the central part of the trailing edge is replaced with a porous material. The studies have shown that the presence of porous material on an airfoil results in better communication between the lower, upper

and trailing edge surfaces of the airfoil and reduces the aerodynamic noise by creating a pressure release mechanism similar to that which occurs in the trailing edge of an owl feather (Lockhard and Lilley 2004). However, the studies show that porous material on the trailing edge can cause significant reduction in the lift force (Herr *et al.* 2014). Therefore, an optimised treatment is essential not to compromise the aerodynamic performance of airfoils in the interest of reducing the noise.

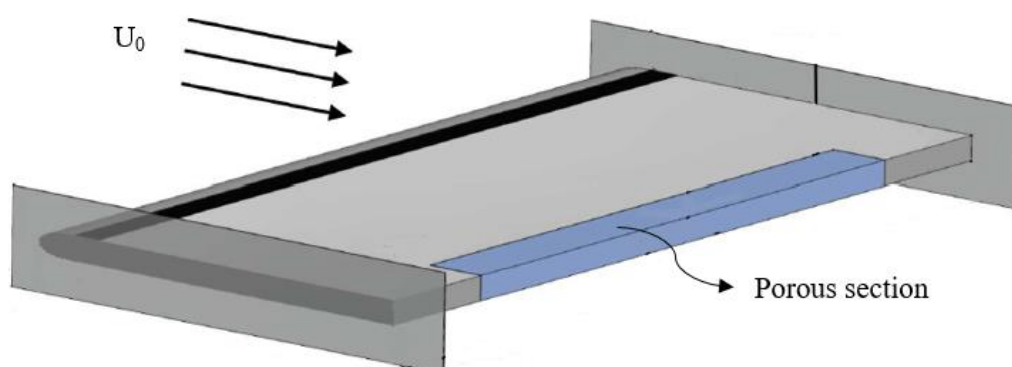


Figure 2.4. Schematic of the blunt trailing edge flat plate with a porous section at the trailing edge (Showkat Ali *et al.* 2017).

2.5 Mathematical Formulations for the Modelling of the Flow Around and Through Porous Materials

Physical heterogeneity of a domain including fluid, solid object and porous material poses challenges for the accurate physical modelling of the processes. The heterogeneity requires introducing different systems of partial differential equations in the free fluid domain and in the porous medium region, which gives rise to a system of coupled

differential equations. Two main methods have been reported to model the fluid flow in configurations containing free fluid, porous layer and solid body domains. One method is to couple the Darcy or Brinkman equation, for flow in a porous medium, with the Navier–Stokes equations, and the other method is the addition of a sink term to the Navier–Stokes equations to represent all the domains.

The primary difficulty in the coupling of the Darcy or Brinkman equation with the Navier–Stokes equations is modelling the interface between the porous medium and the free fluid, which remains a somewhat unresolved problem. One of the proposed models is an empirical relation for the interface given by Beavers and Joseph (1967). The authors assumed that the flow velocity in the porous interface changes from the Darcy velocity in the porous medium (U) to the slip velocity at the interface (u_i). They also presumed that the slip velocity for the fluid is proportional to the shear rate at the interface, and expressed the free flow velocity as:

$$\frac{\partial u}{\partial y} = \frac{\alpha}{\kappa^{1/2}} (u_i - u_p); \quad v = 0, \quad (2.5)$$

in which, κ is the permeability and α is the slip coefficient determined based on the porous medium characteristics. Continuity in the pressure and normal stress across the interface of a porous material and fluid was assumed in some investigations, such as Vafai and Kim (1990), Costa *et al.* (2004a), Costa *et al.* (2004b), Chan *et al.* (2007). The authors discuss that the viscous term in the normal stress is small compared to the pressure and hence the assumption of continuity in the normal stress leads to the continuity in the pressure. Nield (1991) investigated the interface of a fluid and a porous saturated medium and suggested that the pressure and stress change at the interface. Later, Vafai and Kim

(1995) claimed that the velocity and normal stress at the fluid-porous interface is continuous if a zero thickness in the interface is assumed. Other investigators justified the change in the pressure and normal stress at the interface. Ochoa-Tapia and Whitaker (1995a) demonstrated that a stress jump condition exists at the boundary between a porous medium and a fluid and validated their theory by experimental measurements (Ochoa-Tapia and Whitaker 1995b). Tan and Pillai (2009) compared the continuity and stress jump conditions at the porous-fluid interface and found that the two models give similar results in low porosities of porous media, while different results have been found as the porosity decreased. Despite the complications, the coupled problem has gained great attention from both the mathematical and the numerical point of view. Analysis of the coupled Stokes/Darcy system has been studied in the steady state condition (see for example D'Angelo and Zunino (2009) and in the time-dependent case Cao *et al.* (2010)).

An alternative method is the volume penalisation method, a fictitious domain method, which can be implemented without the need to a particular treatment of the interface, which makes it simpler than the coupling method (Arquis and Caltagirone 1984). The penalisation method has been employed in finite difference and finite volume schemes, with pseudo-spectral techniques and adaptive wavelet methods (Schneider and Farge 2002). In the penalisation method, the porous medium and the solid object are modelled as a simple sink term in the Navier-Stokes equation. The main advantage of the penalized equations is that they can be discretised independently of the geometry of the original problem, as the latter has been encoded into the penalisation terms. Such a simplification permits a significant reduction in solver development time, since it avoids the issues associated to the design and management of the grid, allowing for example the use of simple spectral solvers on Cartesian grids (Schneider 2005).

One particular example is the volume penalisation method, introduced by Arquis and Caltagirone (1984) for flows in porous media, which uses the Brinkman–Darcy drag force as a penalisation term. Due to this analogy, the method is sometimes called Brinkman penalisation. The Brinkman-Navier-Stokes equation is written as

$$\partial_t U + (U \cdot \nabla)U - \frac{1}{Re} \Delta U + \frac{U}{K} + \nabla p = 0, \quad (2.6)$$

in which,

$$K = \frac{\kappa \phi U}{\nu H^*}, \quad (2.7)$$

where ϕ is the porosity of the porous medium, U is the mean velocity and H^* is the height of the domain and Re is the Reynolds number based on the mean velocity of the fluid and the height of the domain.

Another example is the macroscopic momentum equation developed by Hsu and Cheng (1990) assuming that the porous material consists of mono-dispersed spherical particles:

$$\partial_t U^* + \frac{(U^* \cdot \nabla)U^*}{\phi} - \frac{1}{Re} \nabla^2 U^* + \nabla p + K^* = 0, \quad (2.8)$$

where U^* is the macroscopic velocity inside the porous medium and K^* is given as

$$K^* = \frac{\phi U^*}{Re Da} + \frac{b}{\sqrt{a}} \frac{1}{\sqrt{Da}} \frac{U^* |U^*|}{\sqrt{\phi}}, \quad (2.9)$$

where a and b are Ergun constants (Ergun 1952), which can be modified according to the porosity and structure of the porous material.

2.5.1 Implementation of the Mathematical Formulations and Numerical Modelling

Numerous researchers modelled the flow interaction with porous walls by fully resolving the porous medium (Larson and Higdon 1986, Durlofsky and Brady 1987, Hsu and Cheng 1990, Vafai and Kim 1990, Kladias and Prasad 1991, Chen and Chen 1992). In particular, the effect of porosity and permeability of porous materials has been extensively studied by the use of numerical techniques. The techniques include the boundary integral method (Larson and Higdon 1986, Larson and Higdon 1987), finite element method (Snyder and Stewart 1966), finite difference method (Schwartz *et al.* 1993), Lattice Boltzman method (Cancelliere *et al.* 1990, Succi *et al.* 1991) and Lattice gas automata method (Rothman 1988, Kohring 1991).

The majority of the numerical studies in the literature regarding porous material treatment are on flows over porous-encased circular cylinders at a Reynolds number below the critical point. Penalisation technique is the most widely used mathematical approach in these numerical investigations, while only a limited number of the investigations used the coupling approach. Rashidi *et al.* (2013) used a coupling approach in simulating the flow over a porous-covered circular cylinder, in which they assumed a continuity in the velocity, shear stress, temperature and heat flux at the interface of the porous and fluid regions. Their study at low Reynolds numbers up to $Re=40$ showed an increase of wake length in the presence of porous cover. The pressure coefficient was found to be either the same or much larger than that of a bare cylinder depending on the

Darcy number. Bhattacharyya and Singh (2011) used a penalisation technique to model the wake of a porous-wrapped circular cylinder placed in a laminar flow at Reynolds numbers between 40 and 200 ($40 \leq Re \leq 200$). They concluded that the use of porous coating for circular cylinders lead to significant reduction of drag, control of vortex shedding and dampening of the structure oscillations compared to a bare cylinder.

Higher Reynolds numbers in the subcritical range have been studied by several authors. In the study by Zhao and Cheng (2010) at Reynolds numbers equal to 1000, 2500 and 5000, Darcy and Navier-Stokes equations were coupled by assuming the continuity condition at the interface between the two regions. Their analysis showed that the thickness and permeability of the porous layer as well as Reynolds number are determining factors in the reduction of the lift coefficient. They also showed that the drag coefficient is either reduced (in Darcy numbers less than 0.001) or unchanged (in Darcy numbers greater than 0.002) at all of the Reynolds numbers they considered. Bruneau and Mortazavi (2008) also investigated the flow over a porous-wrapped circular cylinder at $Re=2400$ and $Re= 24000$ using a penalisation technique. They found that the porous sheath reduces the instabilities at the wake of the cylinder and leads to a more regular vortex shedding. This regularisation is more apparent at the higher Reynolds number, i.e. $Re = 24000$, where the rms value of the lift coefficient reduces by about 72% compared to a bare cylinder. Naito and Fukagata (2012) employed the penalisation technique using DNS and LES simulation methods to study flow control of a circular cylinder covered by a porous surface at different Reynolds numbers in the sub-critical range. They found that the flow stabilisation is more apparent at higher Reynolds numbers where the porous surface delays the onset of instabilities in the boundary and shear layers. This delay causes a shift in the critical Reynolds number for transition from laminar to turbulent regimes by

the use of porous covers. They also showed that when the flow is fully turbulent, a wide region of low energy is generated in the near-wake of a porous-covered cylinder, which indicates the stabilisation of the fluctuating flow field.

An unsteady LES simulation using the penalisation technique was carried out by Liu *et al.* (2012) for the study of a porous-coated circular cylinder at sub-critical condition. The authors demonstrated that the application of porous covers stabilises the wake flow, reduces the wake fluctuations and as a consequent significantly reduces the radiated noise, in particular at the frequencies of vortex shedding. Penetration of flow was also observed, which made the no-slip condition of the velocity at the interface of porous material and fluid no longer valid. In another study by the same authors (Liu *et al.* 2013), an unsteady Reynolds-averaged Navier–Stokes (URANS) method was used in the sub-critical regime employing the penalisation technique. Their results indicate that porous coatings modify the flow characteristics of the near wake generated by a circular cylinder. Porous coatings also significantly attenuate the fluctuations of aerodynamic forces from the aspects of frequency and amplitude. The attenuation of the fluctuations implies that vortex shedding from the bluff bodies is suppressed. The authors also demonstrated the importance of the thickness of the coating on the aerodynamic forces and velocity distribution in the boundary layer. Once again, their results confirmed the penetration of flow inside the porous material and a change in the no slip condition for the velocity on the porous surface. More recently, Liu *et al.* (2015) investigated the flow characteristics within the gap region of two circular cylinders using two-dimensional URANS approach with SST turbulence model. They demonstrated that by using porous covers the flow within the gap stabilises and the turbulence instabilities on the downstream cylinder reduces, which results in the reduction of the noise generated by the cylinders. They also

observed a drag reduction for the downstream cylinder, while an increase in drag coefficient was resulted for the upstream cylinder.

There also exist numerical studies on the flow over other configurations using porous treatments. A study of the flow over a two-dimensional square cylinder with a porous coating was carried out by Bruneau and Mortazavi (2004). The authors used the Brinkman volume penalisation method and found a 30% reduction in drag in the presence of porous coating. In another study by the same authors (Bruneau and Mortazavi 2008) the Brinkman penalisation method was used to simulate the flow inside fluid and porous regions around a rectangular cylinder and two Ahmed bodies with square back and with a rear window. The authors implemented a porous layer between a bluff-body and a fluid, to alter the characteristics of the boundary layer and found a dramatic regularisation of the flow, particularly at high Reynolds numbers. They found the highest drag reduction by 40% for the square back Ahmed body when changing the location of the porous layer around the body. Reduction in pressure gradient in the near wake region by up to 67% was another finding of their research. Rong *et al.* (2011) also numerically studied the flow over a porous covered square cylinder using Lattice Boltzman Method. They found that at $Da \geq 10^{-4}$, the increase in the thickness of the porous cover levels up the drag and lift coefficients. However, at $Da \leq 10^{-4}$, no significant effect on the drag and lift coefficients has been observed by the increase in the porous layer thickness.

More recently, porous treatment of airfoils mainly for the purpose of noise reduction has received considerable attention. Flat-back airfoils, airfoils with blunt trailing-edges, are employed in different applications, for example as the inner blades of large wind turbines. The flat-back airfoils are known for their special characteristics such as a superior aerodynamic performance (Standish and van Dam 2003, Winnemöller and

van Dam 2007, Baker and Dam 2008). However, the bluntness of their trailing-edge leads to the generation of vortex in the wake of airfoils and therefore increases the airfoil drag (Baker and Dam 2008), structural vibration and noise generation. The application of porous material as a mean to improve the aerodynamic and aeroacoustic performance of flat-back structures have been investigated in several studies.

Choudhari and Khorrami (2003) applied a porous material on the side edge of a wing flap to modify the flow field. They used RANS simulations in the steady state conditions. Their results showed that when a porous layer is applied on a small part of the flap, the initiation of vortices and the flow roll-up will be modified, which remarkably weakens the vortex structures at the side edges. They also showed that at high flap deflections, the region in which the axial flow reverses is removed in the presence of porous treatment. This region is associated with the breakdown of the vortex at side edges. Hence, the removal of the reversed flow region eliminates the vortex bursting. The authors concluded the porous treatment can reduce the aerodynamic noise of the high lift device with no compromise in its aerodynamic performance. In another computational study by Khorrami and Choudhari (2003), porous treatment on a slat trailing edge was examined to reduce the trailing edge noise. The unsteady RANS simulation has been used considering a jump condition on the porous surface specifying the relation between the flow quantities on the sides of the surface. It was shown that the use of porous treatment over a miniscule part of the slat surface can reduce the pressure fluctuations near the treated edge. Weaker Strouhal-shedding from the trailing-edge of a finite thickness is found responsible for the reduction in the pressure fluctuations.

Bae *et al.* (2009) also investigated the generation of noise from a blunt trailing-edge flat plate treated with porous material. They used an incompressible large eddy simulation

(LES), for the 3-D computation of the turbulent flow field. For the computation of the acoustic field, they coupled a linearized perturbed compressible equations (LPCE) with the LES. They found that the use of porous material weakens the pressure fluctuations around the trailing edge and breaks the spatial correlation of the wall pressure fluctuations. As a consequence, a reduction in the noise in the far field can be observed in the presence of porous treatment. In addition, the application of porous media to control the noise caused by the trailing edge is investigated by Schulze and Sesterhenn (2013). The authors employed a penalisation technique by introducing a volume force to the Navier-Stokes equations. They performed an optimisation study on the porosity and permeability of porous materials and developed a methodology to minimise the noise generation. Bluntness noise reduction was also studied by Koh *et al.* (2014) who performed numerical simulations by the use of acoustic perturbation equations and LES. The results showed a reduction of 10 dB in the sound pressure level at the fundamental frequency of vortex shedding. Moreover, a reduction of between 3 to 8 dB was observed in the overall level of sound pressure. In a later study, Zhou *et al.* (2015) evaluated the control of turbulence and hence reduction of the noise from a flat plate. The authors developed an discrete adjoint-based optimization framework based on LES and obtained an optimal distribution for the porous media on the trailing-edge of a flat plate.

More recently, a study has been performed by Koha *et al.* (2017) on the noise reduction of the trailing edge. A numerical method was used to study the effect of porous surfaces on the noise. It was demonstrated that the vortex shedding noise is effectively reduced by the porous trailing-edge. The results also indicated up to 11 dB reduction in the overall sound pressure when the flat plate is at an angle of attack equal to zero. Moreover, the attenuation of the noise was attributed to the reduction of the flow

acceleration near the trailing edge due to the presence of porous material. Mobner and Radespiel (2017) performed numerical and experimental studies on a wing with a porous trailing edge. In their 2-D simulations, they used a closure model based on the Darcy and Forchheimer term applied to a Reynolds-stress turbulence model to simulate the turbulent flow through and over porous material. They used pressure and PIV results of their experiments to validate their model. The comparison of the results showed very good agreement between the lift coefficients and boundary layer profiles obtained from both studies. However, the model found to be unable to accurately capture the velocity fluctuations. The authors found limitations in the ability of the closure model in modelling the porous flow and suggested further research for general applications of the model.

2.6 Study of the Effect of Porous Treatment Through Experiments

Experimental studies on bluff bodies modified with porous materials focus mainly on vortex shedding and noise control. Circular cylinders with and without porous cover were examined experimentally in a wind tunnel by Takeshi *et al.* (2010). Aerodynamic force and sound as well as the distribution of the cylinder surface pressure were measured. In addition, Particle Image Velocimetry (PIV) was used to study the flow field at the wake of the cylinders. The experiments revealed a reduction in the vorticity variation in time downstream of the porous covered cylinder. The authors also observed a delay in the separation point and less velocity fluctuations in the near wake of the cylinder that was covered with a porous medium. Less aerodynamic fluctuations and hence less noise was reported when the porous cover was applied. In another study by Showkat Ali *et al.* (2017) porous layers have been used to wrap circular and square cylinders. Hot wire anemometry and PIV measurements were performed at a range of Reynolds numbers within the sub-critical range with foams of different permeability and porosity as porous cover. A

reduction in the drag coefficient was observed for all the square cases with a porous cover, whereas covering the circular cylinders with porous materials resulted in an increase in the drag coefficient at high Reynolds numbers. However, a significant reduction in lift fluctuations has been observed in all cases studied. Delay in the vortex formation, increase in the formation length, and decrease in the turbulent kinetic energy in the near wake were other findings of their research.

The experimental work of Fink and Bailey (1980) was among the very first studies on the use of porous material as a noise control technique. The authors applied porous layers to a high lift device at its flap trailing edge and slat leading edge and found a noticeable reduction of the noise. In a later study by Revell *et al.* (1997), porous treatment has been used on a flap side edge to investigate the effect on the noise reduction. It was found that the use of porous material can significantly reduce the noise of an airframe with a negligible negative effect on the aerodynamic performance. The authors have identified and discussed mechanisms potentially involved in the noise reduction. Flow dissipation, flow penetration into the porous flap medium and porous surface impedance reduction were among the various mechanisms studied for the interaction of the fluid flow and porous material. Finally, a mechanism called flow-through-leakage that reduces the strength of the side edge vortex was found to be the main reason for the noise reduction. Angland *et al.* (2009) has also experimentally studied a flap side edge treated with porous material. Their result showed a shift in the side edge vortex to a downstream location. A remarkable reduction in the turbulent stresses in the shear layer and therefore a reduction in the near-field pressure fluctuations were also observed. Reduction of the pressure fluctuations suggested the attenuation of the noise near the flap side edge.

Sarradj and Geyer (2007) experimentally investigated the effect of porous material on the noise from an airfoil. The experiments were performed on semi-symmetrical SD7003 airfoils. It was shown that at low frequencies the noise is reduced by up to 10 dB in the presence of porous material with minimal compromise in the aerodynamic performance. It was also found that the reduction of noise depends strongly on the resistance of the porous media to the flow penetration. The effect of resistivity of porous materials and surface roughness as well as the likelihood of an increase in the noise at high frequencies were studied by Geyer *et al.* 2010a and Geyer *et al.* 2010b. Lower lift and higher drag forces were observed with airfoils consisting of porous materials. It was also shown that the greater the resistance of the porous material to the fluid flow, a higher lift force and lower drag force will be obtained. Studies were performed on a symmetric NACA0012 airfoil with poro-elastic carper applied on its suction side by Venkataraman and Bottaro (2012). The flow was studied at the airfoil high angles of attacks and in a low Reynolds number. A significant reduction in the drag force and lift fluctuations of the airfoile was observed. The formation of vortex shedding was also delayed compared to the airfoil without the carper on its suction side. Furthermore, the trailing-edge noise was investigated by Geyer and Sarradj (2014) when a porous treatment was applied to the trailing-edge of airfoils. Greater noise reduction was found when larger sections of porous material was used. The authors showed that partial modification of airfoils with porous material will reduces the noise generation and improves the aerodynamic performance. The reduction of noise was partly attributed to the changes in the energy spectrum of turbulence structures. The effect of porous material on the ‘hydrodynamic dampening’ was also found responsible for the noise reduction. However, these phenomena were not backed up with the measurements of the surface pressure or boundary layer at near field.

More recently, a series of experiments have been performed on the use of a blunt porous trailing edge on a flat plate over a range of Reynolds numbers by Showkat Ali *et al.* (2017). The results demonstrated a delay in vortex shedding and an increase in formation length in the case of porous trailing edges. Reduction in the turbulence in the near wake region and expansion of the turbulent structures in the wake were other findings of their research. The authors also found that the higher permeability of the porous material results in more significant drag reduction.

2.7 Summary

As reviewed in this chapter, the use of porous media as a flow control technique has been the subject of several computational and experimental studies. There is a limited number of experimental studies on the dynamics of the flow over porous bluff bodies, and there is a preponderance of numerical studies. Investigations have revealed that porous treatments can stabilise the turbulence in the flow, attenuate the vortex shedding, control the flow instabilities and reduce the noise from airfoils. A number of mechanisms regarding the interactions of flow and porous medium have been identified as the potential reasons for the reduction of the surface pressure fluctuations, break-up of large coherent structures and control of the vortex shedding. As discussed, a part of the changes in the flow field has been mainly related to the hydrodynamic absorption, the penetration of flow into the porous media and viscous interaction between the porous materials and flow.

Flow in porous media is governed by the empirical Darcy's law at low permeabilities. However, the inertia and boundary terms have to be included at high values of permeability. Two main numerical methods for the simulation of flow around porous bodies, namely the coupling method and penalisation method have been discussed. The arguments regarding the treatment of the porous-fluid interface in the

coupling method including the stress continuity and the stress jump approaches have been presented. The study of the literature indicates that the penalisation technique provides promising results in the simulation of porous-flow structures without the complications of the coupling method.

Scrutinizing the literature, the following gaps are identified:

- **Lack of experimental studies on the basic configurations:** As discussed, the experimental studies on the application of porous materials for flow control of the basic configurations are very limited. Among the existing experimental investigations, most of the work is focused on the porous-wrapped bluff bodies. The study of these configurations aids in strengthening our understanding of the fundamentals of the flow control using porous materials for the later applications in the industrial appliances.
- **Limited use of different shapes of porous materials in porous treatments:** The porous treatment used for the basic configurations in the literature mainly includes a sheath of porous material covering the geometry. Some of these studies are devoted to the addition of the porous covers to a bare cylinder, and therefore the effect of the increase in the dimension of the geometry is also included. There is a shortcoming in the use of porous materials in different shapes such that the explicit role of porous material in the change of flow behaviour can be clarified.
- **The wake and boundary layer study:** Current studies on the wake control of bluff bodies investigated some aspects related to the flow mainly drag and lift forces. However, other fundamental aspects, such as boundary layer and the instabilities of the wake structure are not fully addressed. The existing work

suffers from the lack of investigations on the turbulent kinetic energy and Reynolds stresses in the wake region.

The focus of this research directed to filling the gaps in knowledge identified by this literature search. The overarching aim is to better understand the effects of porous treatment on the basic configurations of bluff bodies and to provide an in depth discussion of the flow structures in the wake of the bodies.

CHAPTER 3

EXPERIMENTAL SYSTEM AND INSTRUMENTATION

3.1 Introduction

The work presented in this thesis is motivated by the need to gain insights of the wakes generated by flows over bluff bodies, the surfaces of which have been modified in some way by the imposition of porous media. For this purpose, solid circular cylinders were covered with a sheath of porous material, similar to the previous studies in literature, to provide more data on the flow phenomena in the wake of the cylinders. However, as a new design, square and rectangular cylinders with porous media attached to their downstream faces were considered with the intention to obtain results that are potentially useful in the design of vehicles such as trucks and locomotives. The physical nature of the porous media is clearly important, and in this chapter, we describe how one of its key properties, namely their permeability is measured. Central to this work is the measurement of the flow field. PIV was selected as the measurement technique because it is minimally invasive of the flow compared with probes, say. It is also capable in capturing the entire flow field of interest in a short period of time. In this chapter, we describe in detail the principles, equipment, materials and steps involved in obtaining PIV images. The specifications of a closed loop wind tunnel located in the University of

Bristol in which the experiments have been conducted are provided. The configurations of the bluff bodies and their placement in the wind tunnel along with the coordinate system considered in this work are presented. The PIV system used and the details of image capturing and processing are also described.

3.2 Configurations of the Bluff Bodies

Circular, square and rectangular cylinders are prototypical geometries that are often the subject of studies of external flows. They also arise in practical applications, and they were selected as the configurations of this case study. The diameter, D , of the circular cylinders is 40 mm, and this corresponds with the height of the leading edges of the square and rectangular cylinders normal to the mean direction of flow. The length to height ratio of the rectangular cylinder is set as $L/H = 2$, i.e. $H = 40$ mm and $L = 80$ mm. With this ratio, the flow over the extended cylinder remains fully separated, and no reattachment occurs on the upper and lower surfaces. The 715 mm long-cylinders were positioned in a wind tunnel with their axes horizontal and normal to the mean direction of the airflow.

To assess the effect of porous materials on the flow field, a solid circular cylinder with a diameter of 20 mm was covered with sheets of porous material such that its diameter was equal to that of the bare reference cylinder, namely 40 mm. In the cases of the square and rectangular cylinders, the solid material that comprised the rear halves of the cylinders was replaced with porous materials. The porous materials comprised sheets of polyurethane open cell materials with three different values of pores per inch (PPI*), namely 20, 40 and 60. The configurations of the solid and porous treated cylinders used

* Note that that the non-SI unit, PPI, is used commercially to characterise porous materials.

in the experiments are shown in Figure 3.1. Enlarged images of the three porous media are shown in Figure 3.2.

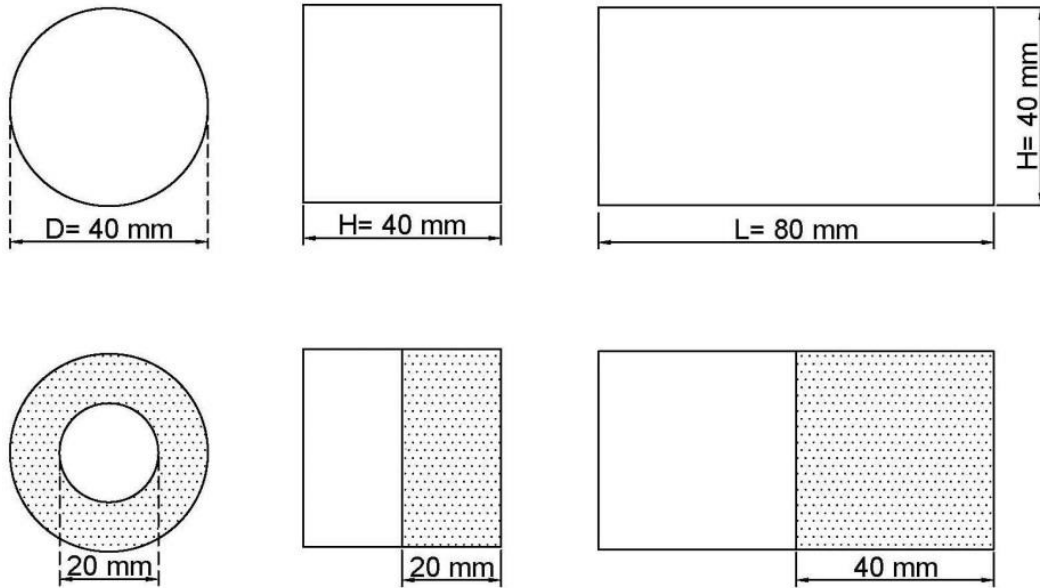


Figure 3.1. The bare circular, square and rectangular cylinders used as the references and the cylinders treated porous materials. The circular cylinder was covered with porous materials and the square and rectangular cylinders were formed by replacing the downstream halves with porous materials.

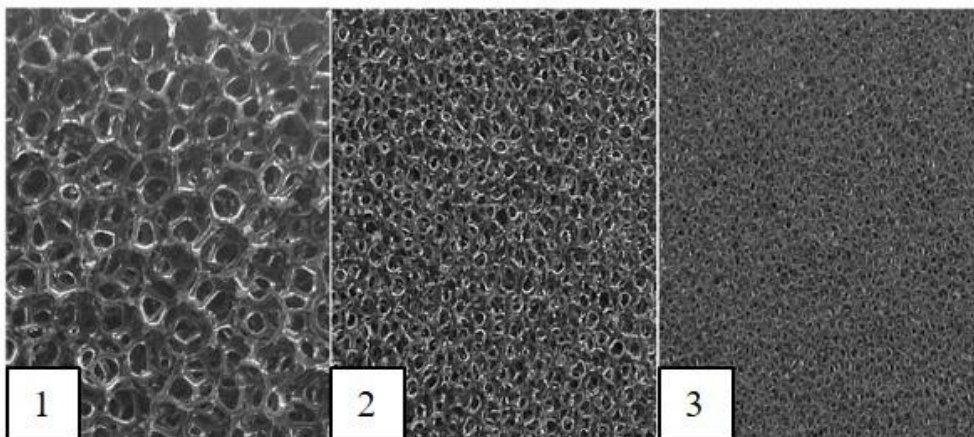


Figure 3.2. The porous materials used in the experiments. 1, 2 and 3 represent the 20 PPI, 40 PPI and 60 PPI, respectively. Their characteristics are given in Table 3.1.

3.3 Porosity and Permeability Measurement

Porous media can be defined as materials consisting of a solid matrix containing pores. The porous media can have either a closed cell structure where the pores are sealed or an open cell structure where the pores are interconnected. The transport in the porous media is through the flow of fluid in the interconnected voids. Porous media are often characterised by their porosity and permeability. Different methods are used to measure porosity and permeability of the porous materials depending on the type of the material. These methods have been widely discussed in literature (for example Bosl *et al.* (1998) and Marshall (1958)). The following two sections discuss the methods that have been used in this thesis to measure porosity and permeability of the porous materials. The measured values are presented in Table 3.1.

Table 3.1 Values of porosity and permeability of the porous materials used in the experiments

Porous material	PPI	Porosity (%)	Permeability (m²)
1	20	91.8	4.64×10^{-7}
2	40	86.2	5.70×10^{-8}
3	60	82.1	6.87×10^{-8}

3.3.1 Porosity

Porosity \emptyset is a property of a porous material indicating the void proportion of the material. Porosity is defined as the ratio of the void volume (V_v) to the total volume (V_t) of the material as:

$$\phi = \frac{V_v}{V_t}. \quad (3.1)$$

One method to measure the porosity of an open cell porous medium is the gravimetry method as the following Eq. (Yunhua *et al.* 2002):

$$\phi = 1 - \frac{\rho_{pm}}{\rho_m}, \quad (3.2)$$

where, ρ_m is the density of the material of which the porous medium is made and ρ_{pm} is the density of the porous medium calculated by dividing the weight of the porous material by its volume. Note that Yunhua *et al.* (2002) have ignored the density of the fluid which is a good approximation when the fluid is air.

Another method to measure the porosity of an open cell porous medium is by the use of the liquid displacement method (Zhang and Ma 1999, Nazarov *et al.* 2004). In the liquid displacement method, the porous material is submerged in a non-solvent liquid with a known volume of (V_1). When the pores of the material are filled with the liquid by a series of evacuation and re-pressurisation cycles, the volume of the liquid containing the porous material increases to (V_2). The volume of the solid skeleton of the porous material is therefore ($V_2 - V_1$). Then, the porous material is removed taking with it the liquid remained within the pores. The volume of the remaining liquid is (V_3). The porosity is therefore given by:

$$\phi = \frac{V_1 - V_3}{(V_2 - V_1) + (V_1 - V_3)} = \frac{V_1 - V_3}{(V_2 - V_3)}. \quad (3.3)$$

In the present work, the liquid displacement method has been used to measure the porosities of the porous materials. The measurements involve carrying out measurements of volumes and weights, which can be carried out with great accuracy. The measurements were repeated three times, and the uncertainty was determined to be less than 1%.

3.3.2 Permeability

Permeability of a porous material is the ability of the material in passing a fluid through it. To measure the permeability of a porous material a fluid of known viscosity is passed through a sample of known dimensions at a predetermined rate. The pressure difference across the sample is then measured and the permeability is calculated from the following Eq. which is now known as Darcy's law, (Darcy 1856).

$$\kappa = -\frac{Q \cdot \mu \cdot \Delta L}{A \cdot \Delta P}, \quad (3.4)$$

where, κ is the permeability of the material, μ is the viscosity of the flowing fluid, Q is the volumetric flow rate, A is the cross-sectional area of the tube in which the flow passes, ΔP is the pressure drop across the porous material and ΔL is the distance that the flow travels through the porous medium. From the above equation, the pressure difference can be calculated as:

$$\frac{\Delta P}{\Delta L} = \frac{\mu}{\kappa} v_D. \quad (3.5)$$

However, Darcy's equation is valid when the flow rate is small. At high flow rates, an extra second-order term for velocity is added to the pressure drop equation, which gives the so called Dupuit-Forchheimer equation (1963) as,

$$\frac{\Delta P}{\Delta L} = \frac{\mu}{\kappa} v_D + \rho C v_D^2, \quad (3.6)$$

where, C is the inertia coefficient. The values of permeability and inertia coefficient can be calculated based on the least mean square method as suggested by Antohe *et al.* (1997). In this method, curve fitting of the pressure drop as a function of fluid flow velocity is performed by rearranging equation 3.6 as

$$\frac{\Delta P}{v_D \Delta L} = A^* + B^* v_D, \quad (3.7)$$

where, $A^* = \frac{\mu}{\kappa}$ and $B^* = \rho C$. The values of A^* and B^* can be found by curve fitting of the pressure-velocity plot using the least mean squared method, out of which the permeability and inertia coefficient can be calculated.

To measure the permeability of porous materials used in this work, an experimental rig was designed and built (Figure 3.3). The permeability rig consisted of a square section tube with a length of 2.5 m. The tube was equipped with static and dynamic pressure taps. Porous samples of 10 mm thickness and square cross-sections equal to 80×80 mm were placed inside the tube at 1.2m from the inlet. Static pressure taps were inserted on the channel 50 mm far from porous samples from each side. This distance was to ensure minimum error would arise due to the flow acceleration and deceleration around the

porous section. The Darcy velocity was considered in this work and measured by other static pressure taps and pitot-tube mounted inside the measurement tube. The pressures were measured using a MicroDAQ Smart Pressure Scanner-32C with an accuracy output of $\pm 0.05\%$ full-scale.

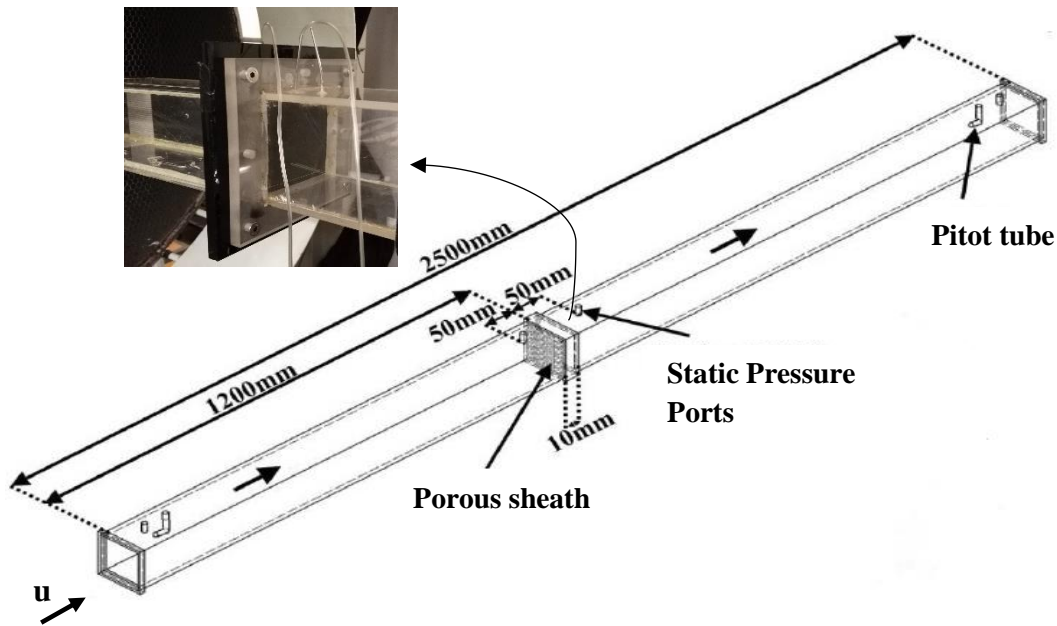


Figure 3.3. The experimental setup for the measurement of permeability of porous materials.

3.3.2.1 Permeability Uncertainty Analysis

To determine the uncertainty in the measurement of permeability of porous materials, the Kline and McClintock error propagation method (Kline and McClintock 1953) was implemented to the least mean squared quadratic function. The uncertainties in the calculation of coefficients A^* and B^* were obtained with this method.

The coefficients A^* and B^* were calculated from:

$$A^* = \frac{\left(\sum_{i=1}^N x_i y_i \right) \left(\sum_{i=1}^N x_i^4 \right) - \left(\sum_{i=1}^N x_i^2 y_i \right) \left(\sum_{i=1}^N x_i^3 \right)}{\left(\sum_{i=1}^N x_i^2 \right) \left(\sum_{i=1}^N x_i^4 \right) - \left(\sum_{i=1}^N x_i^3 \right) \left(\sum_{i=1}^N x_i^3 \right)}, \quad (3.8)$$

$$B^* = \frac{\left(\sum_{i=1}^N x_i^2 y_i \right) \left(\sum_{i=1}^N x_i^2 \right) - \left(\sum_{i=1}^N x_i y_i \right) \left(\sum_{i=1}^N x_i^3 \right)}{\left(\sum_{i=1}^N x_i^2 \right) \left(\sum_{i=1}^N x_i^4 \right) - \left(\sum_{i=1}^N x_i^3 \right) \left(\sum_{i=1}^N x_i^3 \right)}, \quad (3.9)$$

where, x_i represents the velocities of fluid flow and y_i represents the pressure drop per unit length. The uncertainties are then obtained using:

$$\Delta A^* = \sqrt{\sum_{i=1}^N \left(\frac{\partial A^*}{\partial x_i} \Delta x_i \right)^2 + \sum_{i=1}^N \left(\frac{\partial A^*}{\partial y_i} \Delta y_i \right)^2}, \quad (3.10)$$

$$\Delta B^* = \sqrt{\sum_{i=1}^N \left(\frac{\partial B^*}{\partial x_i} \Delta x_i \right)^2 + \sum_{i=1}^N \left(\frac{\partial B^*}{\partial y_i} \Delta y_i \right)^2}. \quad (3.11)$$

The uncertainties in the calculation of permeability and inertia coefficient were then calculated substituting $A^* = \frac{\mu}{\kappa}$ and $B^* = \rho C$ in the following equation:

$$u = \frac{\Delta M}{M} \times 100\%. \quad (3.12)$$

The values of uncertainties in permeability u_k and inertia coefficients (u_c) for all the porous materials are tabulated in Table 3.2.

Table 3.2 Values of porosity and permeability of the porous materials used in the experiments

Porous material	Permeability (m²)	u_k	Inertia coefficient	u_c
1	4.64×10^{-7}	2.4586	1658	14.1691
2	5.70×10^{-8}	2.9586	1162	8.5248
3	6.87×10^{-8}	3.5648	985	5.3421

3.4 Measurement of the Flow Field

Techniques that have been developed and introduced to determine the flow field may be categorized as being either invasive or non-invasive. In invasive methods flow information is obtained by means of probes located in the flow stream, and these may distort the fluid flow (Lundgren and Ashurst 1989, Bruun 1995). An example of this method is hot wire anemometry. As an alternative, non-invasive methods are generally optical methods in which a thin sheet of light is employed to capture the flow information by illuminating small tracer particles seeded in the flow (Kazuo and Hang-Yu 2000). Particle Image Velocimetry (PIV) and Laser Doppler Velocimetry (LDV) are examples of non-invasive methods. The flow behaviour is negligibly affected in non-invasive methods as the measurement equipment is placed outside of the system with no contact with the fluid. Non-invasive methods are capable of giving highly resolved spatial and temporal data due to their high speed light scattering and advanced data acquisition and signal processing systems.

Selecting an appropriate technique to measure the flow field in the wake of the cylinders was a major consideration in this work. PIV has become a technique of choice in the investigation of fluid dynamics in recent decades. PIV has been drastically advanced over the past two decades by the emergence of digital recording that has replaced the analogue recording. Powerful computers to process high volume of data in a relatively short time has also improved the capabilities of PIV. The applicability of PIV to different types of flow including gas and liquid flows over a range of temperatures and pressures makes it a desirable method for the study of the fluid dynamics. PIV provides significant advantages over other measurement techniques such as temperature and pressure based probe measurements and other laser diagnostic techniques including laser Doppler velocimetry (LDV) and phase Doppler particle analysis (PDPA). The advantages include the non-invasive nature of PIV as well as the capability of PIV in measuring large regions of the flow field in the wake of the bluff bodies. It also allows a great amount of experimental data to be collected in a short time frame providing both quantitative and qualitative insights. These features render PIV a suitable measurement technique for this study.

3.4.1 Experimental Setup

Experiments were carried out to visualise and quantify the mean velocity fields in the wakes of the cylinders to examine the effect of the permeable cylinders on the wake behaviour. Measurements of the velocity field were obtained using Particle Image Velocimetry (PIV) in a low turbulence wind tunnel at the University of Bristol. The wind tunnel has a contraction ratio of 12:1, and the test section has a cross-section that is 800 mm wide, 600 mm high and with a working section length of 1000 mm. The wind tunnel

allowed optical access through a glass wall on its side. The turbulence intensity of air entering the test section at the velocity of 20 m/s has been measured to be around 0.05%.

Figure 3.4 shows a schematic diagram of the wind tunnel in which a test model is located and the experimental apparatus used in the PIV measurement. As shown in the figure, the cylinders have been mounted horizontally with their axes perpendicular to the direction of flow.

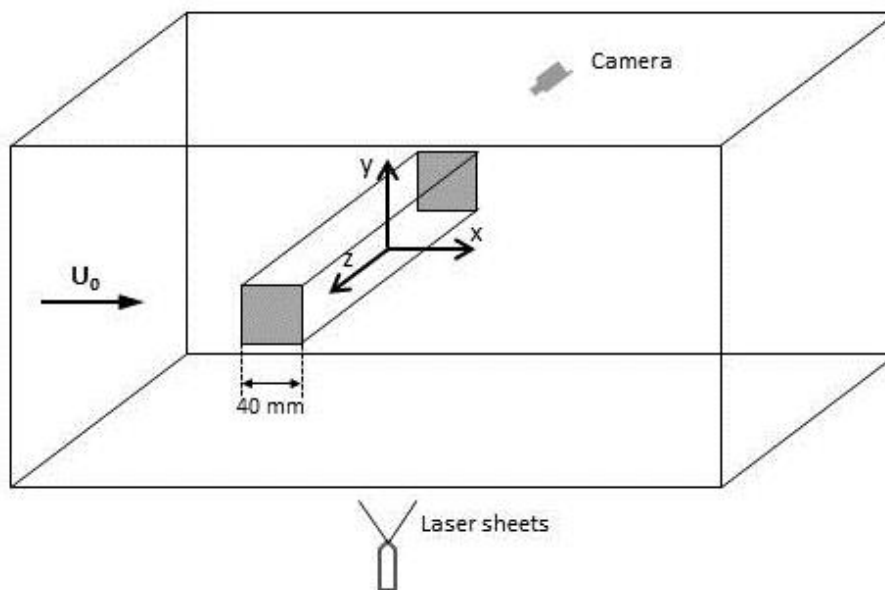


Figure 3.4 A sketch of the wind tunnel test section with a sample test model and the coordinate system with its origin at the centre of the models. The camera is positioned on the transparent side of the wind tunnel in the direction of the cross section of the models and the laser is located below the models and outside the wind tunnel.

The origin of the local coordinate system was defined at the downstream edge of the cylinders. The x-axis is aligned with the mean flow direction, the y-axis is the vertical axis and the z-axis coincides with the cylinder axis. The flow condition was chosen to ensure a turbulence boundary layer flow, with the appearance of vortex shedding. Measurements were carried out at a Reynolds number of about 5.3×10^4 based on the

inflow velocity and the diameter for the circular cylinders or the height for the square and rectangular cylinders. At This Reynolds number, the vortex street developed is fully turbulent (Blevins 1977). To determine the most suitable air velocity, a series of range-finding experiments have been conducted. Reynolds number of 2.65×10^4 , 5.30×10^4 and 7.95×10^4 were studied., and it was observed that they had negligible effect on the flow field. A fluid velocity of 20 m/s was chosen because it would enable capturing a significant region of the flow field. This velocity was also highly compatible with the Particle Image velocimetry equipment available. The blockage ratio for all the configurations was less than 6% ensuring that the presence of the cylinders has a minor effect on the aerodynamic performance of the system (West and Apelt 1982).

The cylinders used in the series of experiments were made of aluminium with the dimensions mentioned in section 3.2. The solid and porous-covered circular cylinders used in the experiments are shown in Figures 3.5 and 3.6, respectively. The porous cylinder in Figure 3.6 is covered with a 60 PPI porous material. The solid and half-porous rectangular cylinders used in the experiments are presented in Figures 3.7 and 3.8, respectively. The downstream half of the cylinder in Figure 3.8 is replaced by a 60 PPI porous material. The light sheet hits the middle of the cylinders. Due to the reflective nature of the aluminium the light will reflect and damage the camera lens. Therefore, this middle part is covered with a black sheet to prevent the reflection of the light.



Figure 3.5 The solid circular cylinder mounted in the wind tunnel. The black part in the middle is to prevent light reflection due to the aluminium reflective property.



Figure 3.6 The porous covered circular cylinder mounted in the wind tunnel. The porous material shown is 60 PPI.



Figure 3.7 The solid rectangular cylinder mounted in the wind tunnel. The black part in the middle is to prevent light reflection due to the aluminium reflective property.

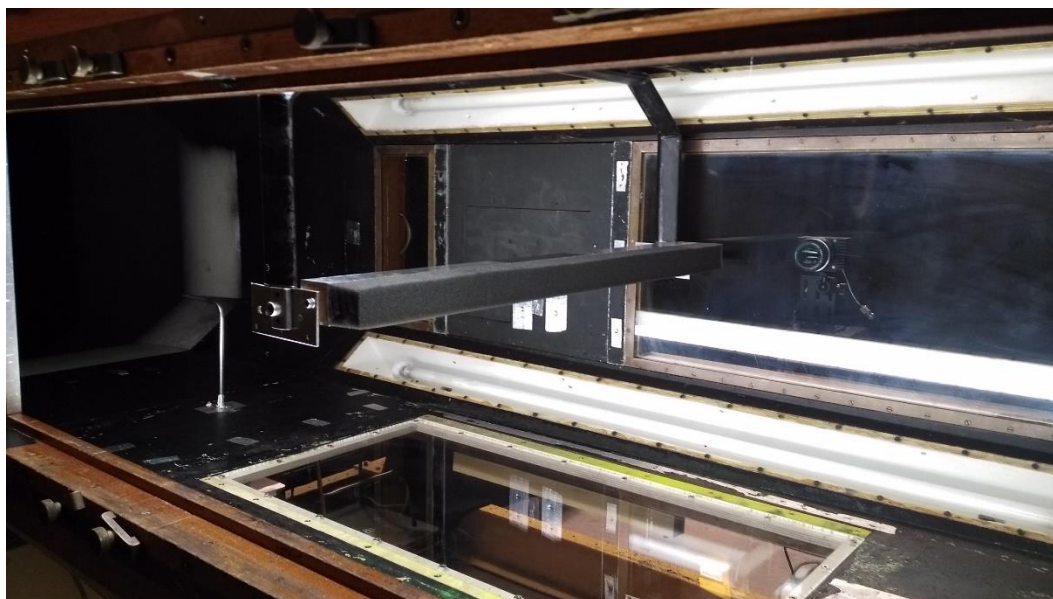


Figure 3.8 The half-porous rectangular cylinder mounted in the wind tunnel. The porous material shown is 60 PPI.

3.4.2 PIV Sub-Systems and Data Analysis

In PIV, velocity is measured in a plane formed by sheets of light generated by lasers. Other characteristics of the flow field such as flow instabilities can also be determined in that plane. PIV required a light source, a recording instrument and an image processing device. Light pulses are produced by a laser and projected through a region in the flow field. Small size particles injected into the fluid are illuminated by two successive laser pulses. The images of the particles suspended in and moving with the flow is typically recorded by a Charge-Coupled Device (CCD) camera during two pulses. The consecutive images are then divided into small interrogation areas and processed using a cross correlation method to produce velocity vectors associated with the flow. The history of the development of PIV measurement technique, fundamentals, applications, current status and possible future improvements have been extensively addressed in literature (Lauterborn and Vogel 1984, Adrian 1986, Dudderar *et al.* 1988, Adrian 1991, Buchhave 1992, Grant 1997, Raffel *et al.* 1998, Prasad 2000, Adrian 2005). The PIV sub-systems and steps in PIV measurements are described in sections 3.4.2.1 to 3.4.2.6.

3.4.2.1 Pulsed Lasers

The particles in the PIV experiments are illuminated in a 2-D plane at least twice in a short time interval. The light scattered by the tracer particles acts as a photographic flash that is sensed by the digital camera. The laser light source is required to have a high power. The more powerful light source employed, the smaller tracer particles can be used and the velocity lag between the particles and the fluid will be minimized. A high light energy can be produced by a pulsed laser in a short time frame. The light pulses must have a short enough duration to freeze the motion of the particles during the pulse, thus preventing blurred images. On the other hand, the duration between pulses must be

adequately long so that sufficient resolution of the displacement between the images is made possible.

A variety of lasers with different limitations and abilities are being used for PIV. Neodym-YAG (Nd:YAG) lasers are solid state lasers which are most commonly used for PIV. The beams in Nd:YAG lasers, generated by Nd³⁺ ions, are orthogonally polarized. High amplification and good mechanical and thermal properties are the characteristics of a Nd:YAG laser. The Nd:YAG laser also has a relatively low laser threshold so that it can generate many successive pulses. Nd:YAG lasers can provide adequate pulse energies between 100 and 750 mJ. The monochromatic nature of the laser lights enables the plane illumination and particle movement recording without chromatic aberration. The fundamental wavelength of 1064 nm is frequency doubled in PIV. When the frequency doubled portion is separated, around 532 nm of the original light energy will become available. PIV lasers are mostly designed as double oscillator systems to enable the adjustment of the separation time between two pulses independent from the pulse strength. Therefore, the two lasers are emitted with a predetermined time delay. Nd:YAG lasers are often operated in a repetitive mode. In the present work, a Nd-YAG laser, positioned below the floor of the wind tunnel, was used to illuminate an x-y plane that intersects the mid-section of cylinders. The laser has a maximum energy output of 200 mJ at a wavelength of 532 nm and the emission interval of the laser is 50 μ s and the thickness of the illuminated sheet of light is approximately 1 mm.

3.4.2.2 Tracer Particles

The fundamental assumption in PIV is that the particles follow the fluid faithfully and both fluid and particles move as one (Melling 1997). Based on this assumption, the

particle velocity is measured instead of the fluid velocity. Therefore, flow seeding is an important component in a PIV set-up. Particle size, shape, density and concentration are determining factors in the agreement of the particles and fluid motion. Proper selection of the above particles properties can prevent any velocity lag and hence increase the accuracy of the flow measurements. The typical particles used in PIV seeding include silver-coated hollow glass spheres, oils and gas bubbles for liquid flows and smoke and atomized oils for gas flows. In this work, a mixture of water and polyethylene glycol 80 in a volumetric proportion of 4:1 was prepared as the seeding medium. The air was seeded with 1 to 5 μm particles of the mixture.

- **SIZE AND SHAPE**

Size, shape and orientation of the seeding particles affect the scattering of the light. Increasing the diameter of the particles improves the intensity of the scattered light, but jeopardizes the tracking of the fluid motion. An alternate solution is to increase the concentration of the particles but at the expense of increasing the background noise. Therefore, in determining the size of the tracer particles it is important to find a compromise between small and large particles. The particles should be small enough to be able to track the fluid motion and large enough to adequately scatter the laser light. Evidently, the size of the seeding particles must be small compared to that of the fluid particles to prevent any significant changes in the fluid velocity due to the presence of the particles.

- **DENSITY**

The density of the particles should match that of the fluid. If this criterion were satisfied the particles would respond rapidly to changes in the fluid velocity. It is also necessary for the particles to remain suspended in the stagnant fluid. In other words, when

the fluid has a zero velocity, the particles should not be affected by the gravitational field. Although, in practical applications the densities of the fluid and particles do not exactly match, the difference is neglected. To estimate the particle velocity, Stokes' drag law given in Eq. 3.13 can be used (Raffel *et al.* 1998). In Eq. 3.13, particles are assumed spherical flowing in a viscous low Reynolds flow with a continuous acceleration.

$$U_p(t) = U[1 - e^{-\frac{t}{\tau_s}}] \quad (3.13)$$

where, U_p is the particle velocity, U is the fluid velocity and τ_s is the relaxation time indicating the response of a particle to the acceleration of the fluid, defined as:

$$\tau_s = d_p^2 \frac{\rho_p}{18\mu} \quad (3.14)$$

where, d is the particle's diameter and μ is the dynamic viscosity of the fluid. The tracer particles used in this work had a relaxation time of order 10^{-7} seconds.

- CONCENTRATION

The concentration of the particles in an image area known as interrogation area is an important factor in getting high spatial resolution. The density of the particles in the area of investigation should be small enough to enable the individual identification of the particles and high enough to provide sufficient data points. (Keane and Adrian 1990) recommended that a minimum of 15 particles is present in an interrogation area in a double pulsed system. A homogenous distribution of the particles in the area of interest is another important factor.

In order to track the movements of the particles, it is important to record both the light pulses in the same image frame. Any particle that follows the flow satisfactorily and

scatters enough light to be captured by the camera can be used. To make sure that the particles do not tend to sediment and distort the actual velocity profile, the number of particles in the flow have to be monitored, particularly in obtaining a good signal peak in the cross correlation [refer to section 3.4.2.5]. Commonly, 10 to 25 particles should be seen in each interrogation area (Figure 3.9). Hence, the measurement volume can be obtained from the interrogation area size, image magnification and the light-sheet thickness.

3.4.2.3 Image Pre-Processing

A cross-correlation camera (FlowSense 4MP) with a spatial resolution of 2072 by 2072 pixels was used to record the movement of the seeding particles. Particle traces were processed using an adaptive cross-correlation method to generate the velocity vectors even though it is noticeably more time consuming than other methods. The adaptive method optimizes the size and shape of each interrogation area in an iterative way. The optimization is done to improve the conformity to the local flow gradients and seeding densities. The measurement field was 224 mm \times 224 mm corresponding to 5.6 D \times 5.6 D for the circular cylinders, 5.6 H \times 5.6 H for the square cylinders and 5.6 H \times 2.8 L for the rectangular cylinders. Due to the limitation of the mobility of the laser beam, a part of the region above the cylinders could not be captured (Figure 3.4). In the image processing, interrogation areas of 16 \times 16 pixels were used with an overlap of 50%, which leads to a 0.86 mm vector spacing.

In each experiment, 1600 sequential images were acquired at a sampling rate of 15 Hz. The acquisition time of 1600 sampled image pairs for each case was above 2 hours. The instantaneous images were used to obtain the time-averaged velocity components

and therefore the flow field and other statistical quantities. For some configurations, two overlapping windows were captured because a single window was insufficient to encompass the entire wake region. The captured images have to be pre-processed to ensure uniform illumination of the measurement area and eliminate any undesired reflections of light. Each experimental sampling involves a large number of images that can be used to compute the median value of the illumination. The median value can be in turn used to detect the actual displacement of the particles (Hart 2000). In addition, ambient light and improper focus or alignment of the camera creates certain amount of noise that can deteriorate the image quality at portions of the image. Also, spurious vectors can be created due to the low quality of images, lack of particles, etc. therefore, a quality control is required to detect and eliminate the spurious vectors.

3.4.2.4 Interrogation Area

In PIV, the displacement of particles is computed from two consecutive images taken between two laser pulses. However, due to the large amount of particles in each image it is almost impossible to track the same particle in both images. Therefore, each image is divided into small areas called interrogation areas. Figure 3.9 shows an interrogation area at time t with its corresponding interrogation area at time $t+\Delta t$. The displacement of particles in the time interval Δt is used to calculate the mean velocity vector. The assumption is that all the particles move homogeneously between two light pulses in each interrogation area. A cross-correlation is used to calculate the average displacement of particles in each interrogation area. The average displacement is then used to create the 2-D velocity vector map. The interrogation area typically has a dimension of 16×16 to 128×128 pixels. Around 10 to 15 particles need to exist in an interrogation area to obtain a reliable estimation of the particle displacement (Raffel *et al.*

1998). In the experiments conducted in this research, interrogation areas of 16×16 pixels with sufficient particles density have been used.

3.4.2.5 Evaluation of the Particle Displacement

The mean displacement of the particles in the interrogation areas is computed using a cross-correlation technique. The cross-correlation between the corresponding interrogation areas from successive times is calculated by performing Fast-Fourier Transform (FFT). The plot resulted from cross correlation procedure has a peak which gives the best estimation of the particles displacement in the window. Knowing the displacement and the time between two successive images, the mean velocity in each interrogation area can be calculated. The PIV cross-correlation procedure is shown in Figure 3.9.

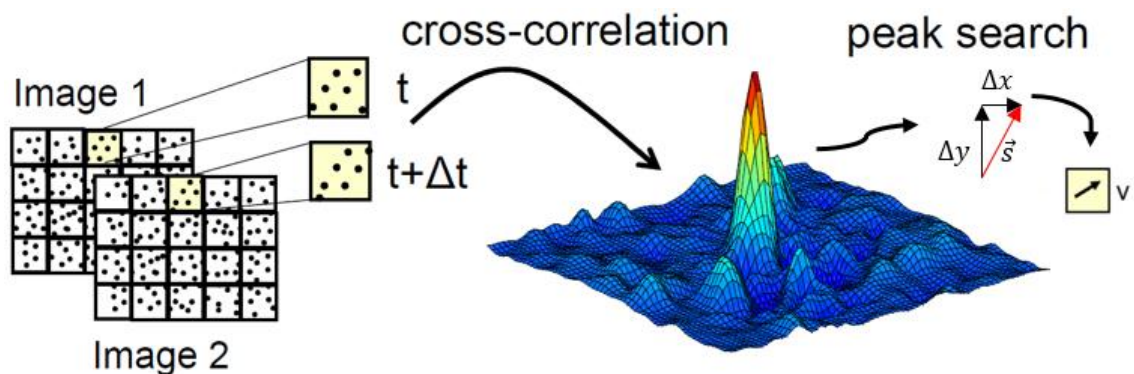


Figure 3.9 The cross correlation procedure in PIV velocity measurement. A plot is obtained from two corresponding interrogation areas using a cross-correlation algorithm, which is then used to calculate the velocity vector.

The geometric centre of the interrogation area is typically used to estimate the velocity. When overlapping of the interrogation area and image boundary happens, the position of the geometric centre can be located out of the boundaries of the image. Therefore, the velocity field will contain some false velocity vectors. To correct the

physical position of the velocity field a weighting function is applied which adjusts the real location of the velocity vectors (Lecuona *et al.* 2002, Usera *et al.* 2004).

In this set of experiments, 16×16 pixels interrogation areas have been used with a 50% overlapping to obtain the velocity field. This window size has been found by trial and error to have the minimum signal to noise ratio and hence the minimum number of spurious vectors. Less interrogation window overlap gives a weak correlation and a bigger overlap requires special attention in the calculation of the differential quantities (Raffel *et al.* 1998).

It should be noted that in PIV only one velocity vector is obtained from the interrogation area, i.e. the velocity of all the particles in the area is averaged (Dudderar *et al.* 1988). Hence, the final velocity field is a filtered version of the real velocity of the flow. This filtering causes a reduction in the resulting second order quantities such as turbulent kinetic energy (Adrian and David 2005).

3.4.2.6 PIV Post-Processing

The essence of PIV is the recording of successive images that portray the position of the tracer particles. From there, it is possible to extract mean velocity field, and measures of turbulence. A considerable amount of post-processing is required to obtain this detailed information. Because of the finite size of adjacent sampling windows, spurious velocity data may arise, which must be corrected. Post-processing also involves reduction of the data into forms that are readily visualised and interpreted.

When obtaining PIV recordings, there usually exist a number of incorrect velocity vectors that can be identified by visual inspection of the data. Special algorithms have to be employed to automatically detect and delete these incorrect data. However, full data fields are usually required in most post processing algorithms. Therefore, the deleted data

have to be replaced with consistent data to fill the gap in the experimental results. The huge amount of the velocity vector maps is hard to interpret to derive the fluid characteristics. Averaging is a commonly used technique to obtain the mean flow information and the flow fluctuations. Other techniques such as conditional sampling and vector field operators are also used. Conditional sampling determines the periodic and non-periodic parts of the flow and vector field operators such as vorticity and divergence discovers the flow structure. The final step in the post-processing of PIV data is the analysis of the reduced data. Data analysis is a challenging task which involves temporal and spatial analysis. Proper orthogonal decomposition (POD) (Wiegel and Fischer 1995) and neural networks (Carosone *et al.* 1995) are examples of the analysis tools that are used for this purpose. The uncertainty of PIV measurements was measured by considering the uncertainty in the subpixel displacements (Timmins 2010) and was found to be below 1 %.

3.5 Summary

In this chapter, the settings of experiments are presented. Bare solid cylinders with circular, square and rectangular cross sections were selected to form benchmarks. Three porous materials used in the experiments, characteristics of the materials along with the techniques for their measurements are presented. The selection of disposition of the porous materials on each configuration is also described. Circular cylinders were treated such that half of their diameters was composed of porous materials. The square and rectangular bluff bodies were modified so that their upstream and downstream halves consisted of solid and porous materials respectively. As a result, their leading and trailing edges were respectively solid and porous.

Experiments were performed in a wind tunnel operating under conditions that resulted in a Reynolds number of about 53000 based on the diameter of the circular cylinder and the dimension of the leading edges of the square and rectangular bodies. PIV were selected for the measurement of the flow field downstream the bluff bodies because as a non-invasive method, it does not interfere with the flow. The fundamentals of the PIV technique, the laser and seeding particles are described in this chapter. The pre-processing of the images taken by a cross-correlation camera used in the experiments are also discussed in detail. Moreover, PIV tests provide a large number of images that should be post processed. The post-processing of the data as an important stage in obtaining accurate results is also described.

CHAPTER 4

EXPERIMENTAL RESULTS AND DISCUSSION

4.1 Introduction

The preceding chapter has described the details of the model configurations and experimental procedure employed in this research to characterise the wake flow. A set of three 2-dimensional bodies, representing increasing bluffness, were studied, namely circular, rectangular, and square cylinders. The porous material treatment for each configuration to control the flow behaviour was presented. Finally, the PIV set-up along with the considerations in a PIV test was discussed.

This chapter presents the results of the PIV experiments. Both qualitative and quantitative studies of the flow features associated with the flow over the bluff body configurations are performed. The average whole field PIV data based on large sample numbers are analysed for the purpose of identifying steady and unsteady flow structures. The flow structure downstream of the bluff bodies with and without porous treatment are compared and discussed. Differences in the effect of porous treatments on different configurations are also presented.

4.2 Circular Cylinder

The time-averaged streamlines based on the non-dimensional stream-wise velocity generated by the solid and porous circular cylinders are shown in Figure 4.1. The black zones in the figure are the zones where laser pulses could not reach due to the blockage by the object, as the laser was located below the wind tunnel. Therefore, no data could be achieved by PIV at the regions above the objects. The same argument holds for the square and rectangular cross-section cylinders presented in Figures 4.8 and 4.14. In the case of the solid cylinder, it is observed that a recirculation zone is generated within a relatively short distance downstream of the solid cylinder. The zone ends at $x/D \approx 2.3$, where the stagnation point forms. Therefore, the recirculation length (L_r), calculated from the downstream extremity of the cylinder to the stagnation point, is about $2.3 D$ for the solid cylinder. The shift in the formation of circulation cells when using porous covers with a range of permeabilities is evident in Figure 4.1. The length of recirculation extends to about $4.4 D$ and $4.6 D$ in the case of porous 60 PPI and 40 PPI, respectively. When the circular cylinder is covered with a layer of porous medium with a high permeability (20 PPI porous sheet) the flow field in the wake is quite different from that observed in the case of the bare circular cylinder. For example, we observe that air exits from the porous medium on the downstream half of the cylinder. This effluxion of air from the downstream face prevents recirculation cells forming immediately downstream of the cylinder. In this case the recirculation is delayed and occurs only after $x/D \approx 2.5$ and extends to $x/D \approx 5.3$.

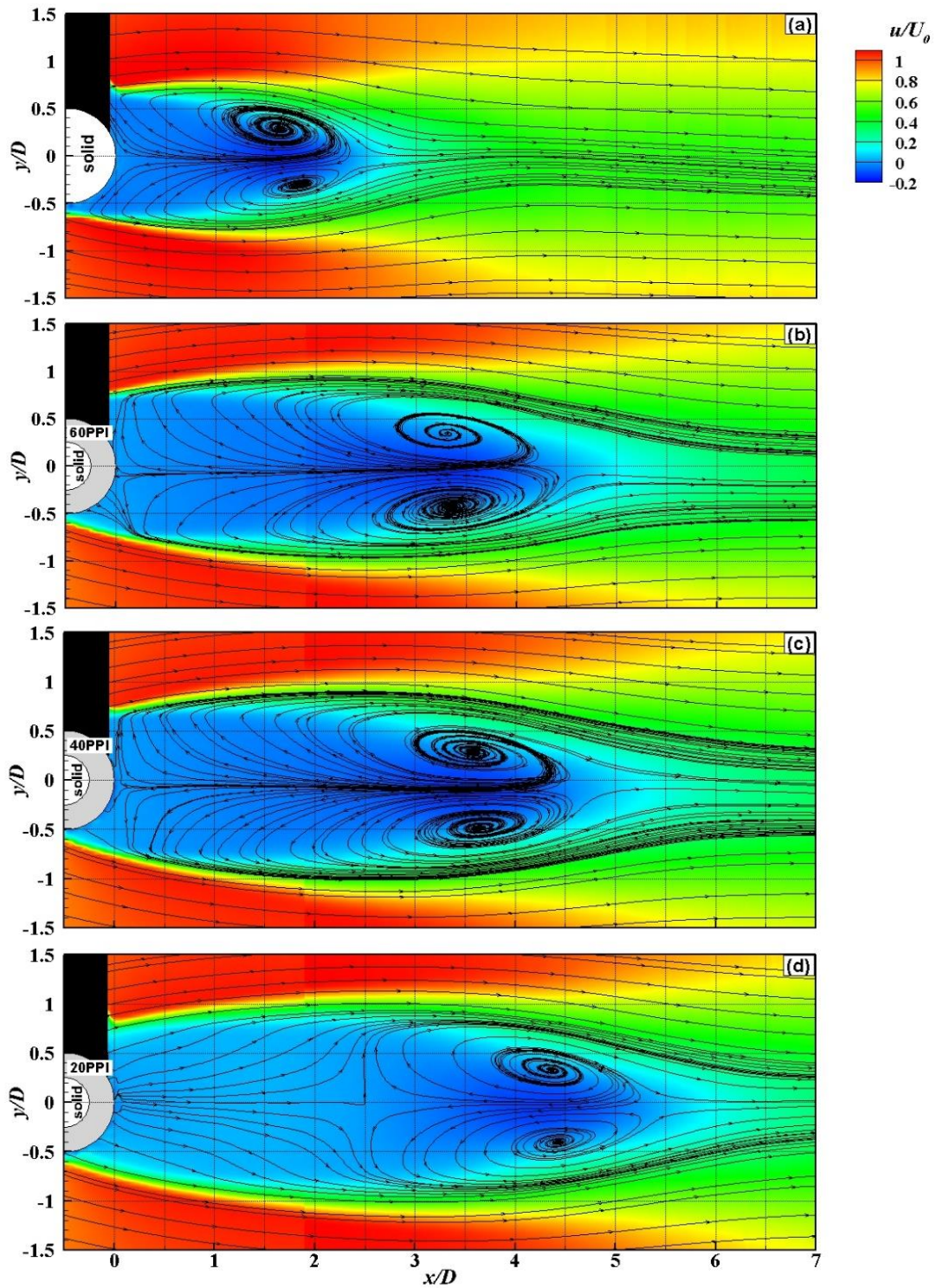


Figure 4.1 Time-averaged streamline topology for circular cylinders; (a) bare cylinder, (b) cylinder covered with 60 PPI porous layer, (c) cylinder covered with 40 PPI porous layer and (d) cylinder covered with 20 PPI porous layer

The presence of porous media has a significant effect on the downstream displacement of the eyes of the recirculation cells. For example, the location of the recirculation centres from the trailing edge of the cylinder is at $1.64 D$ and $1.82 D$ in the case of the bare circular cylinder, and $4.37 D$ and $4.43 D$ for the cylinders covered with highly permeable porous sheets (20 PPI). The presence of the porous media also has the effect of increasing the thickness of the wake. This is manifested in part by the vertical location of the eyes of the vortices in being $+0.3 D$ and $-0.3 D$ created by the bare circular cylinder and $+0.33 D$ and $-0.4 D$ when the cylinder is covered with a porous medium that has 20 PPI.

4.2.1 Velocity Components for Circular Cylinders

Figures 4.2 and 4.3 show the non-dimensionalised, time-averaged stream-wise (u/U_0) and cross-wise (v/U_0) velocities at the axial locations, $x/D = 1, 2, 3, 4, 5$ and 5.5 , where x is the distance downstream of the base of the circular cylinder. As one might expect, the results reflect those presented in Figure 4.1. It can be seen from Figure 4.2 that at $x/D = 1$ all of the stream-wise velocity profiles generated by the cylinders with porous surfaces are quite uniform in the range $|y/D| < 0.5$, and the mean horizontal velocity in this range is close to zero. In other words there is a quasi-stagnant region immediately downstream of the cylinder.

In contrast, in the case of the bare circular cylinder at $x/D = 1$ the corresponding horizontal velocity profile increases monotonically with distance when $0 < |y/D| \leq 0.9$. The reason for this behaviour is that air permeates the porous media from which it emerges with a component of velocity in the stream-wise direction. In the presence of the

porous media the flow exhibits a behaviour that is akin to early separation compared with the case of flow over a bare circular cylinder.

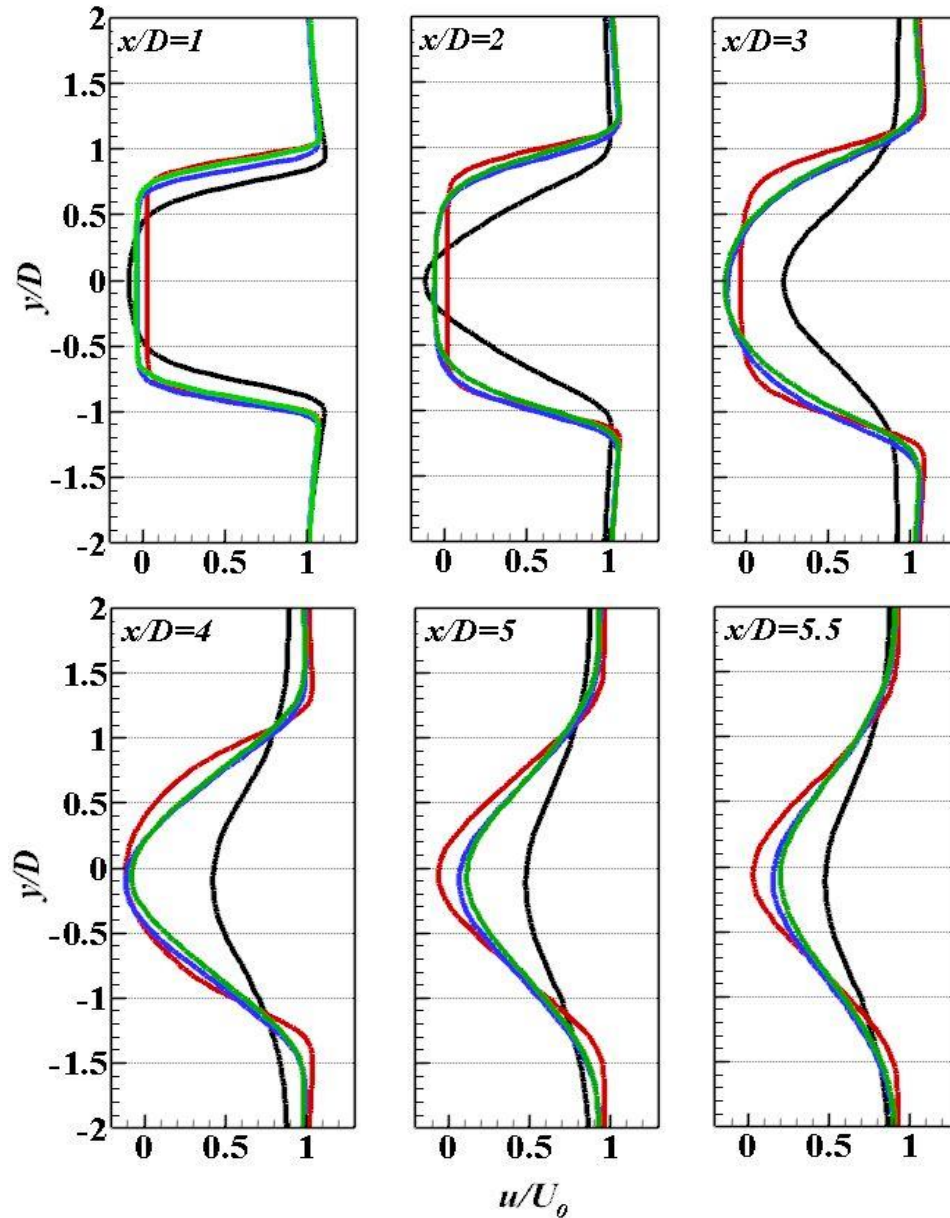


Figure 4.2 Mean stream-wise velocities at different axial locations from circular cylinders. black line: solid; green line: porous 60 PPI; blue line: porous 40 PPI; red line: porous 20 PPI

Between $x/D = 1$ and $x/D = 2$ the widths of the wakes generated by the porous medium covered cylinders increase in thickness. This implies that in this region there are

positive and negative components of vertical velocity components in the vicinity of $y/D = 1.0$, and this is confirmed by the plots of v/U_0 , shown in Figure 4.3. In this region the net flow into the wake behind the circular cylinder is seen to be relatively small. In the case of the most permeable porous medium the mean horizontal component of the fluid in the wake between $x/D = 1$ and $x/D = 3$ evolves slowly and this is reflected in the rather small and uniform values of the vertical velocity. This contrasts with the wake downstream of the bare circular cylinder which becomes increasingly uniform downstream of the cylinder, and this is accompanied with a flow of fluid towards the centreline of the system.

By $x/D = 5$, the horizontal component of the wake is becoming uniform, and as a result the conservation of mass demands that the vertical components of the velocity are small. However, when $x/D = 5$ the wakes behind the cylinders covered with porous media are still developing, and this is reflected by the horizontal velocity component continuing to lose mass to the mean flow ($x/D = 5.5$). Because the mean stream-wise velocity of the fluid immediately downstream of the porous-covered cylinders is close to zero at $x/D = 1$, the conservation of mass demands that the vertical components of flow in this region are also close to zero. This is borne out by the data depicted in Figure 4.1. This figure indicates that net flow of fluid is away from the centre line in the regions $y/D > 1.0$.

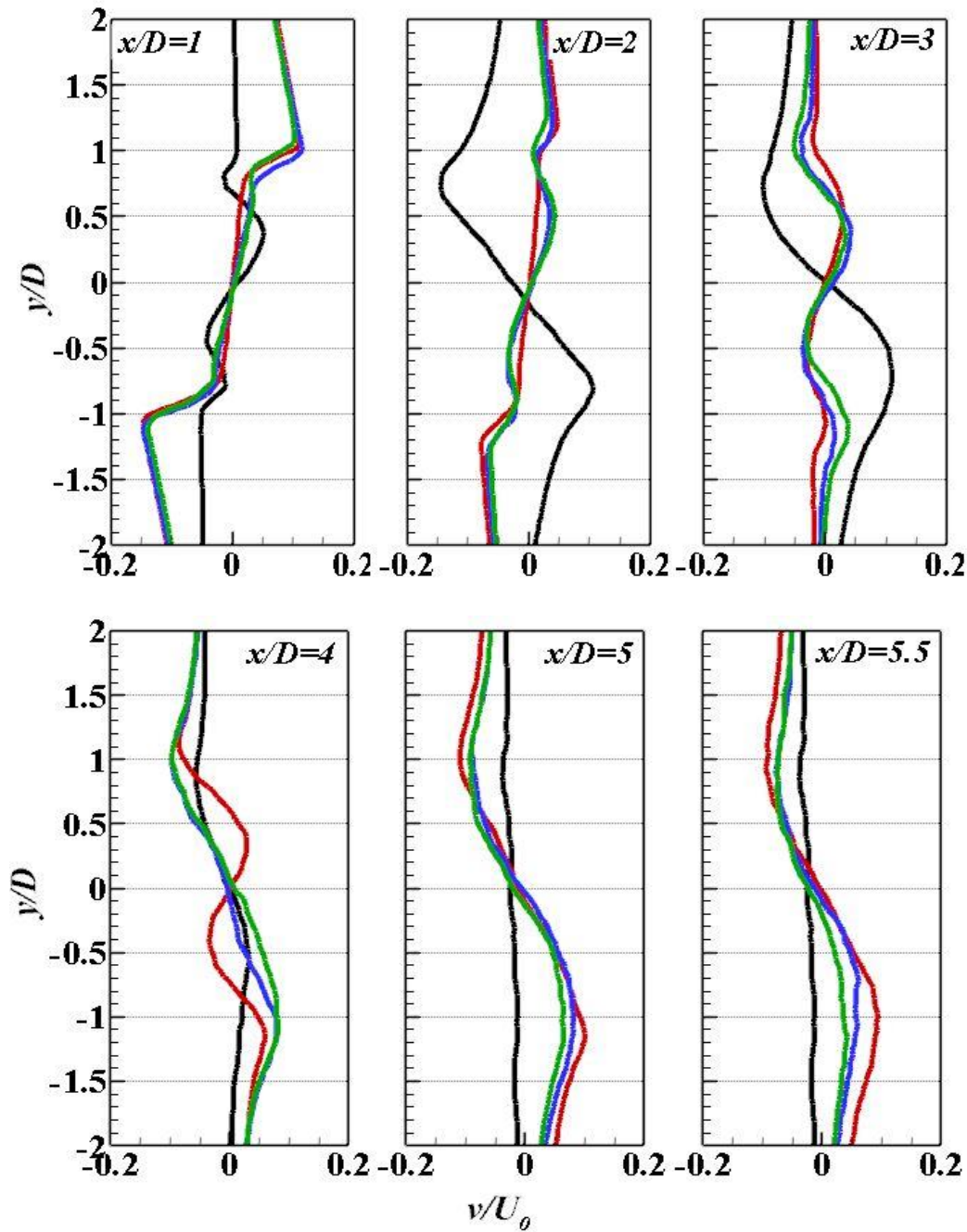


Figure 4.3 Mean cross-stream velocities at different axial locations from circular cylinders. black line: solid; green line: porous 60 PPI; blue line: porous 40 PPI; red line: porous 20 PPI

The cross-stream mean velocity downstream of the solid cylinder at $x/D = 1$ depicted in Figure 4.3 is consistent with the flow field portrayed in Figure 4.1 and the law of conservation of mass. The results shown in both figures demonstrate that the fluid generally flows away from the centreline, and that a maximum occurs at a distance of

$|y/D| \approx 0.5$. In the case of the solid cylinder the distance $x/D = 2$ is downstream of the vortices, and as a result it can be seen that this is associated with a net flow of fluid towards the centreline as the vertical component of velocity increases. This pattern is observed to continue until $x/D = 5$ but the cross-stream velocity attenuates as the flow begins to retain its uniformity.

The magnitude of the cross-stream velocity for all porous cases is much less than that of the solid cylinder within the near-wake region ($x/D < 2$). From $x/D = 2$, the cross-stream velocity profiles for the 40 PPI and 60 PPI cases gradually increase. The increase in the value of the (v/U_0) at $x/D = 3$ signifies the existence of vortex structures, evident in Figure 4.1. However, the (v/U_0) profiles for the porous 20 PPI case exhibits a reversed flow at $x/D = 4$, which is close to the vortex centre.

4.2.2 Reynolds Stresses for Circular Cylinders

In a turbulent flow, the unsteady turbulent motions contribute to the mean motion of the flow. The effect of turbulent fluctuations on the mean flow is identified by the decomposition of the Navier-stokes equations. The decomposition of the non-linear terms and averaging over a time scale results in additional stress terms called Reynolds stresses. The Reynolds stresses are generated in the form of both normal stresses and shear stresses, which indicates the existence of additional momentum fluxes.

Normalised Reynolds stress components for the solid and porous-treated circular cylinders are presented in Figures 4.5, 4.6 and 4.7. It is observed from Figure 4.5 that the value of the normal stress $\overline{u'u'}$ for the solid cylinder develops quickly, increasing significantly moving further downstream towards the recirculation zone, followed by a

reduction in the far-wake region. The peak of the $\overline{u'u'}$ profile is located at about $|y/D| \approx 0.75$ near-wake at $x/D = 1$, which is the centre of shear layer, and moves downward to about $|y/D| \approx 0.5$ far wake at $x/D = 5$. In the porous cases, the magnitude of $\overline{u'u'}$ near the centreline remains negligible compared to the solid centreline $\overline{u'u'}$ up to $x/D = 3$. Nevertheless, at further downstream locations, the value of $\overline{u'u'}$ near the centreline for the porous cases is greater than that for the solid case, which is due to the delay in vortex shedding, as observed in Figure 4.1. The peak location of $\overline{u'u'}$ for porous cases is at a farther distance from the centreline compared to the solid case, which indicates changes to the location of flow separation point on the surface of cylinder. For instance, in the near-wake ($x/D = 1$), the peak location for porous cases varies from $|y/D| \approx 0.8$ to $|y/D| \approx 0.9$, also indicating different separation points for each porous case.

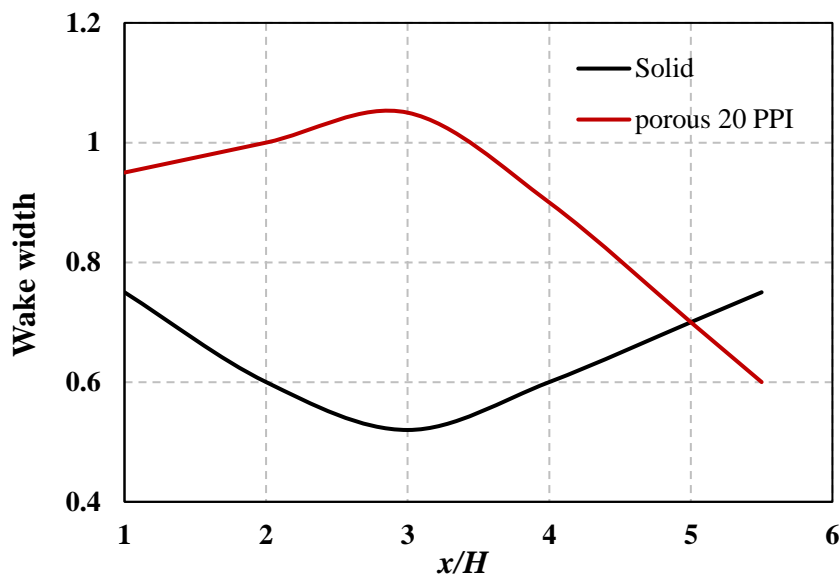


Figure 4.4 The wake width generated in the wake of solid circular cylinder and the circular cylinder treated with 20 PPI porous material.

The wake width is estimated from the location of the maximum fluctuation of the stream-wise velocity at the wake of cylinder (Norberg 1986). The plots of wake width for the solid case and the circular cylinder treated with 20 PPI porous material are presented in Figure 4.4. As the behaviour of all porous-treated circular cases are the same, the wake width is plotted only for the 20 PPI porous case as the most effective treatment. From the Figure, it is observed that the wake width for the solid cylinder initially shows a sharp decrease from a value of about 0.75 at $x/D = 1$ to about 0.52 at $x/D = 3$, after which it climbs up to that of $x/D = 1$ at $x/D = 5.5$. The porous cylinder however shows the opposite behaviour. In the porous case, the wake width starting from a value about 0.95 at $x/D = 1$ gradually increases to about 1.06 at $x/D = 2.9$. The wake profile then experiences a steep decrease to a value of 0.6 at $x/D = 5.5$.

The $\overline{v'v'}$ component of the normal stress (Figure 4.6) for the solid cylinder is almost zero before the vortex centre, then suddenly increases from $x/D = 1$ to $x/D = 2$. Furthermore, the peak location of the $\overline{v'v'}$ term moves towards the centreline as we move downstream. The maximum value of $\overline{v'v'}$ is observed after the vortex zone at $x/D = 3$. In case of porous cylinders, however, the magnitude of $\overline{v'v'}$ is almost zero up to $x/D = 2$ for the 40 PPI and 60 PPI cases and up to $x/D = 3$ for the 20 PPI case. Subsequently, beyond the recirculation zone, the value of $\overline{v'v'}$ begins to increase considerably. This shows the delayed recirculation which can also be observed in Figure 4.1.

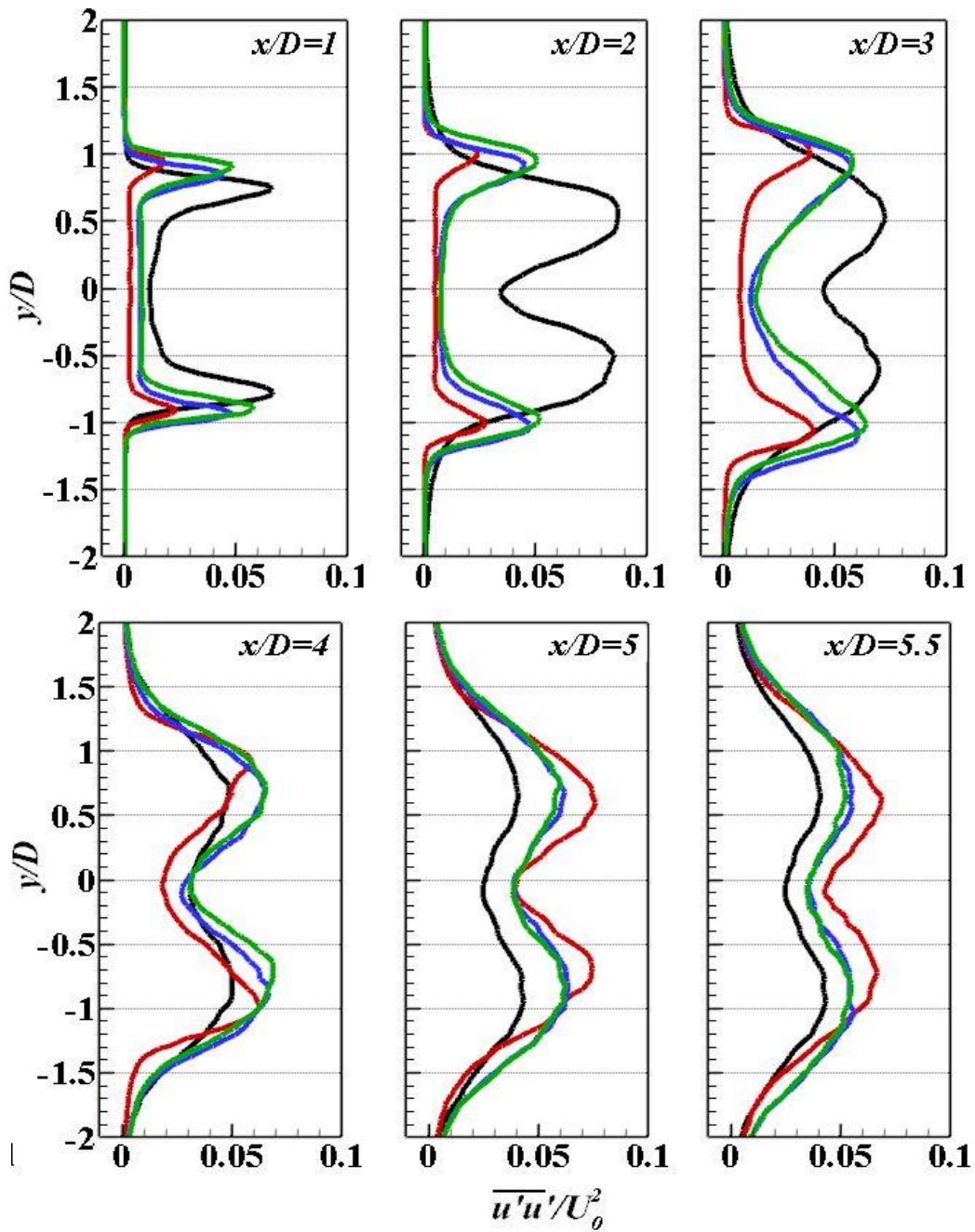


Figure 4.5 Normal stream-wise Reynolds stress in the wakes of the circular cylinders. black line: solid; green line: porous 60 PPI; blue line: porous 40 PPI; red line: porous 20 PPI

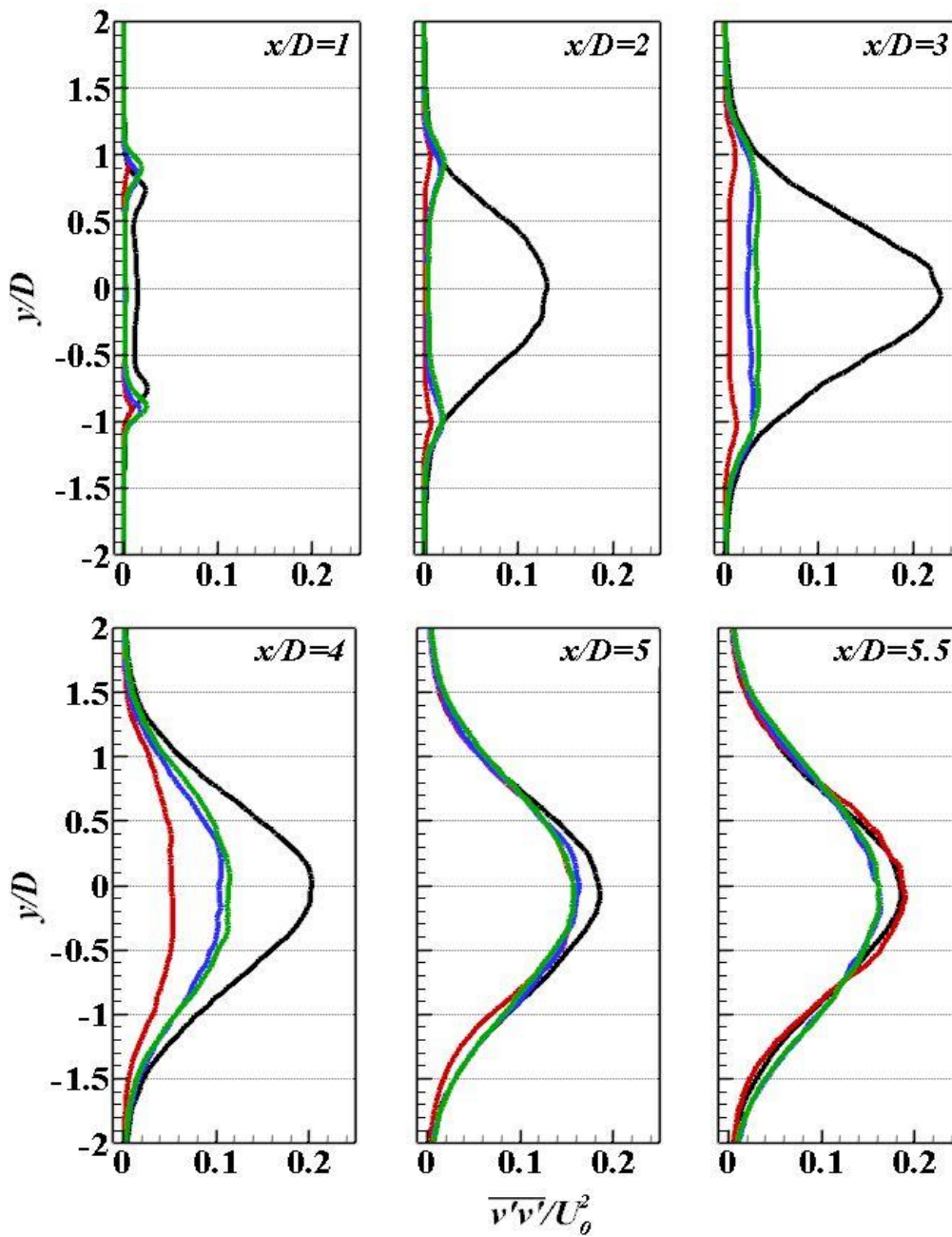


Figure 4.6 Normal cross-stream Reynolds stress in the wakes of the circular cylinders. black line: solid; green line: porous 60 PPI; blue line: porous 40 PPI; red line: porous 20 PPI

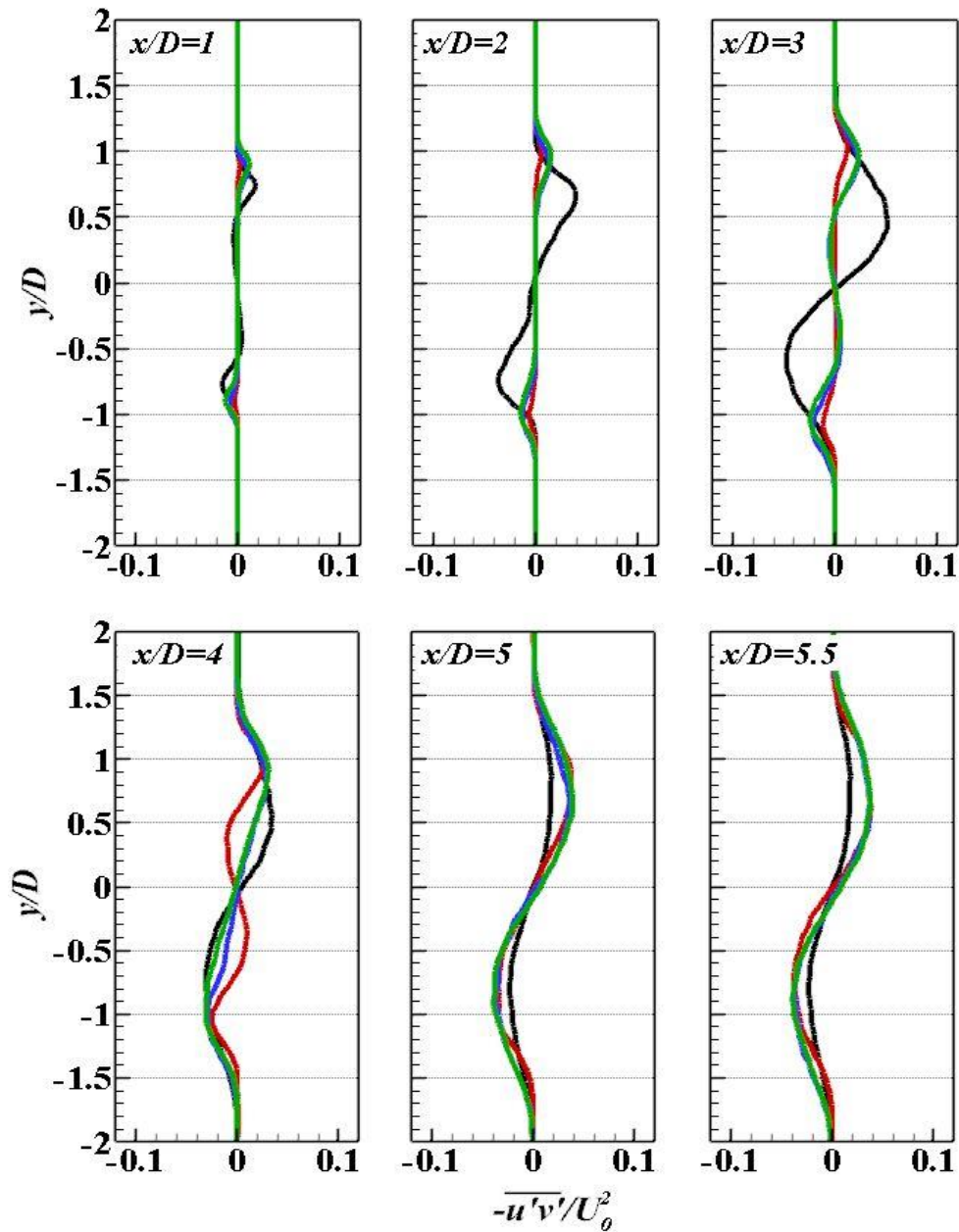


Figure 4.7 Shear Reynolds stress in the wakes of the circular cylinders. black line: solid; green line: porous 60 PPI; blue line: porous 40 PPI; red line: porous 20 PPI

The turbulent kinetic energy (TKE), also expressed as (k) , for a quasi-two-dimensional flow can be derived from both Reynolds normal stresses based on the definition (Jones and Launder 1972):

$$\text{TKE} = \frac{(\overline{u'u'} + \overline{v'v'})}{2}. \quad (4.1)$$

Features of TKE may be inferred from the $\overline{u'u'}$ and $\overline{v'v'}$ results. The TKE content in the wake of all cylinders is presented in Appendix A. From the $\overline{u'u'}$ and $\overline{v'v'}$ profiles, it can be concluded that TKE around the centreline is almost zero in the near-wake of both the solid and porous covered cylinders. The energy content of the flow for the porous covered cylinders reduces significantly further downstream in comparison to the solid cylinder for all permeabilities. The outer porous cover attenuates the large vortices, therefore weakens the velocity fluctuations downstream of the cylinder. The vortex sheds at a further downstream location in the case of cylinders with porous covers (illustrated in Figure 4.1). The Reynolds shear stress ($-\overline{u'v'}$) term is an important parameter for describing the turbulence production (shown in Figure 4.7). The $-\overline{u'v'}$ in the case of bare circular cylinder, increases with distance within the near-wake region and reaches its maximum at $x/D = 3$. The Reynolds shear stress for the porous cylinders is negligible in the near-wake, increasing to that of the solid cylinder at $x/D = 5$.

4.3 Square Cylinder

The time-averaged streamline results for the square cylinders with and without the porous treatment are presented in Figure 4.8. As expected, a pair of counter-rotating vortices is formed in the near-wake of the reference model (solid cylinder). However, the vortices formation is delayed and occurs further downstream for cylinders with porous treatment. This is believed to be due to the reduction of the velocity gradients in the vertical direction immediately downstream of the cylinders fitted with porous media compared to the bare square cylinder. This is particularly visible in the case of the most

permeable porous medium (20 PPI), where reverse flows can be seen entering the rear face of the square cylinder. Although this phenomenon is not observable in the case of the less permeable porous treatments the eyes of the recirculation regions are nonetheless observed to be forming further downstream than in the bare square cylinder case.

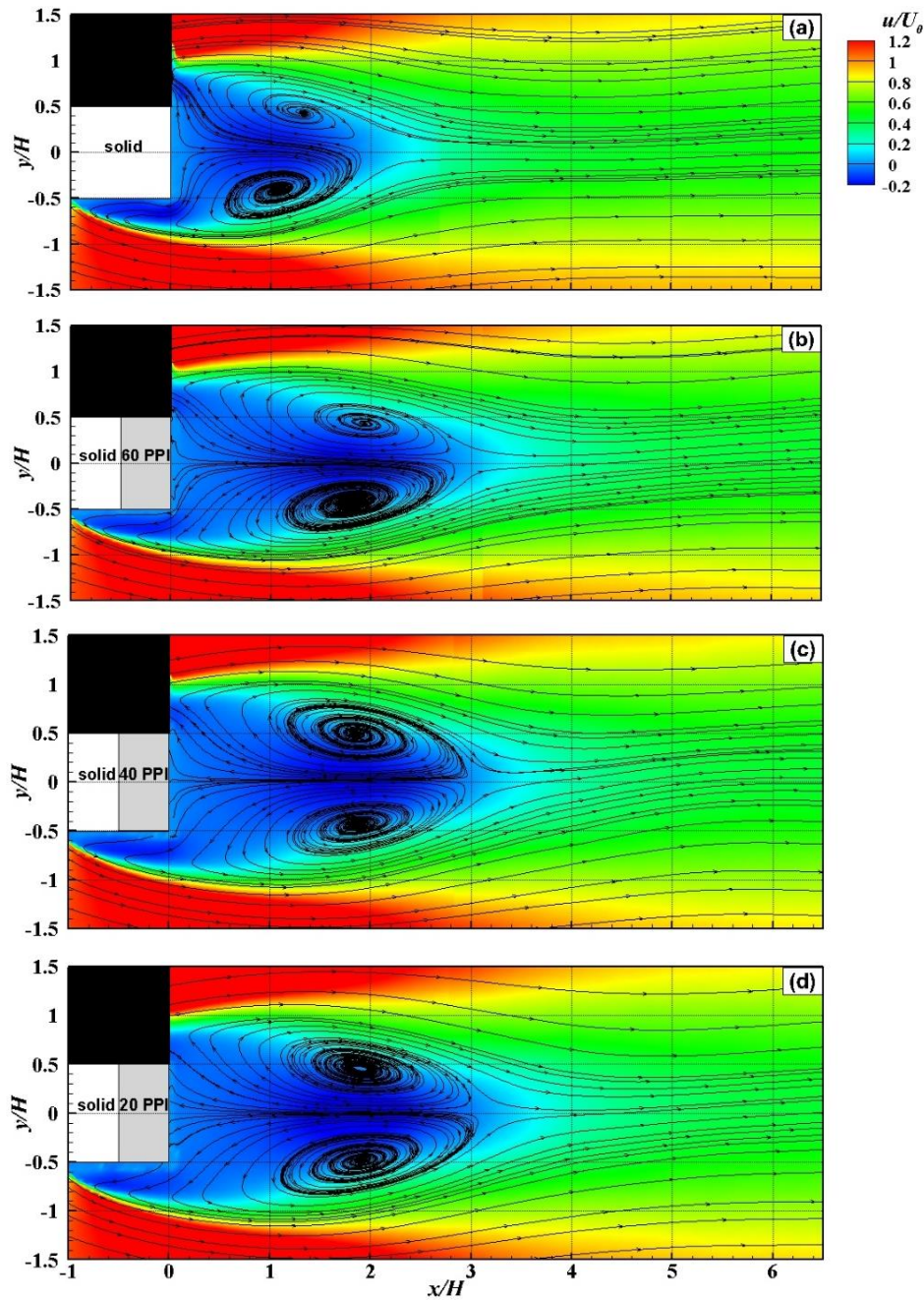


Figure 4.8 Time-averaged streamlines generated by square cylinders; (a) bare cylinder, (b) cylinder treated with 60 PPI porous layer, (c) cylinder treated with 40 PPI porous layer and (d) cylinder treated with 20 PPI porous layer

4.3.1 Velocity Components for Square Cylinders

Figures 4.9 and 4.10 respectively display the mean horizontal and vertical velocity components at selected distances, normalized by the freestream velocity, for the square cylinder configurations. In the case of a solid square cylinder, a flat top hat profile is seen for the stream-wise velocity (u/U_0) in the near-wake ($x/H = 0.5$) which transforms into a parabola-like curve in the far wake. Porous-treated cylinders exhibit a lower velocity region at all axial locations, which is believed to be due to the flow penetration into the porous media on the downstream face of the square cylinders.

For the cylinders treated with a porous layer, the velocity profiles retain their flat top hat behaviour for a greater distance, followed by the parabola-like velocity behaviour at $x/H = 1.5$. Moreover, a higher velocity deficit in the whole wake region can be seen in the porous cases, which is more significant at far-wake locations. The shear layer width remains almost the same for both the solid and porous cases, which is because there are no changes in the separation point. A reversed flow region can be observed from the cross-wise velocity (v/U_0) for the solid case at $x/H = 1.5$ in Figure 4.10, which corresponds to the vortex centre. The reverse flow behaviour for the porous cases, however, occurs at $x/H = 2$, consistent with the results presented in Figure 4.8.

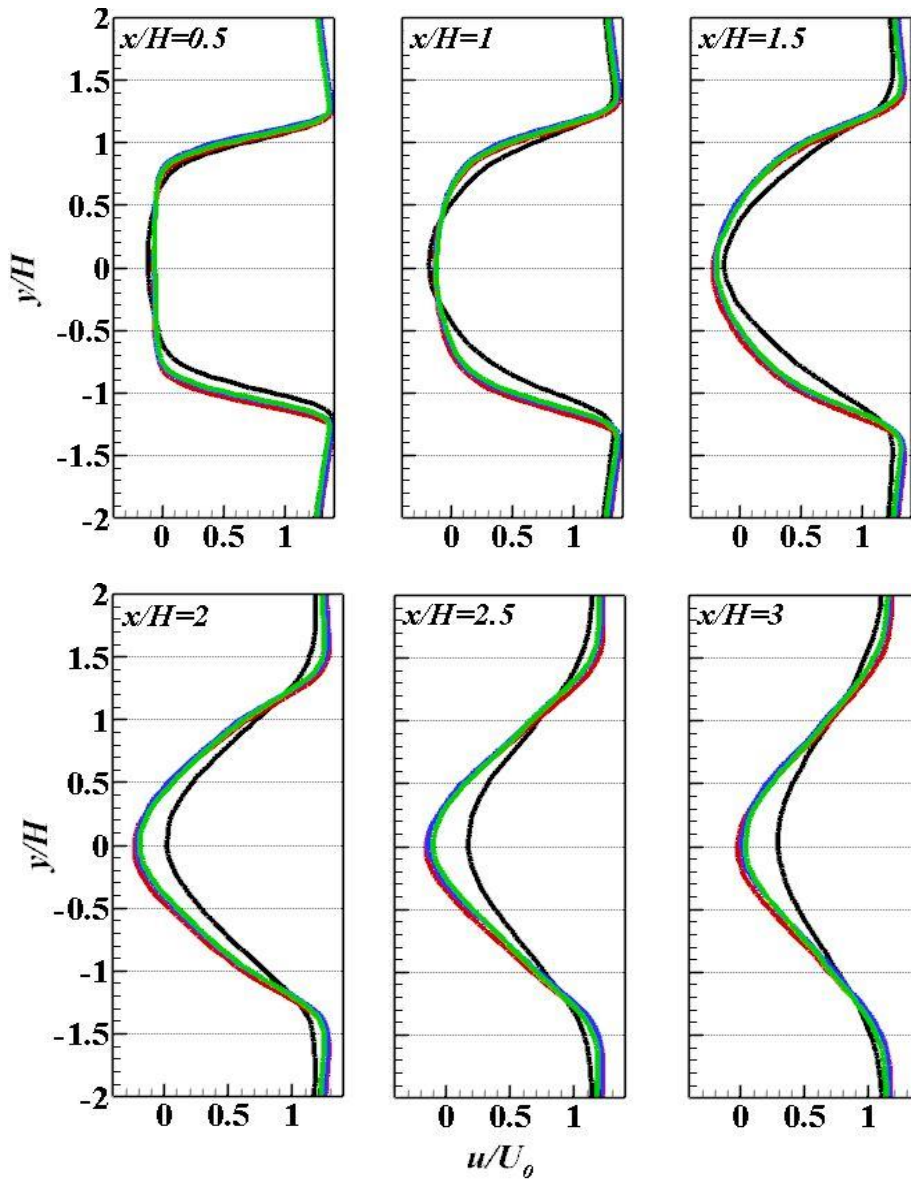


Figure 4.9 Mean stream-wise velocities at different axial locations generated by the square cylinder. black line: solid; green line: porous 60 PPI; blue line: porous 40 PPI; red line: porous 20 PPI

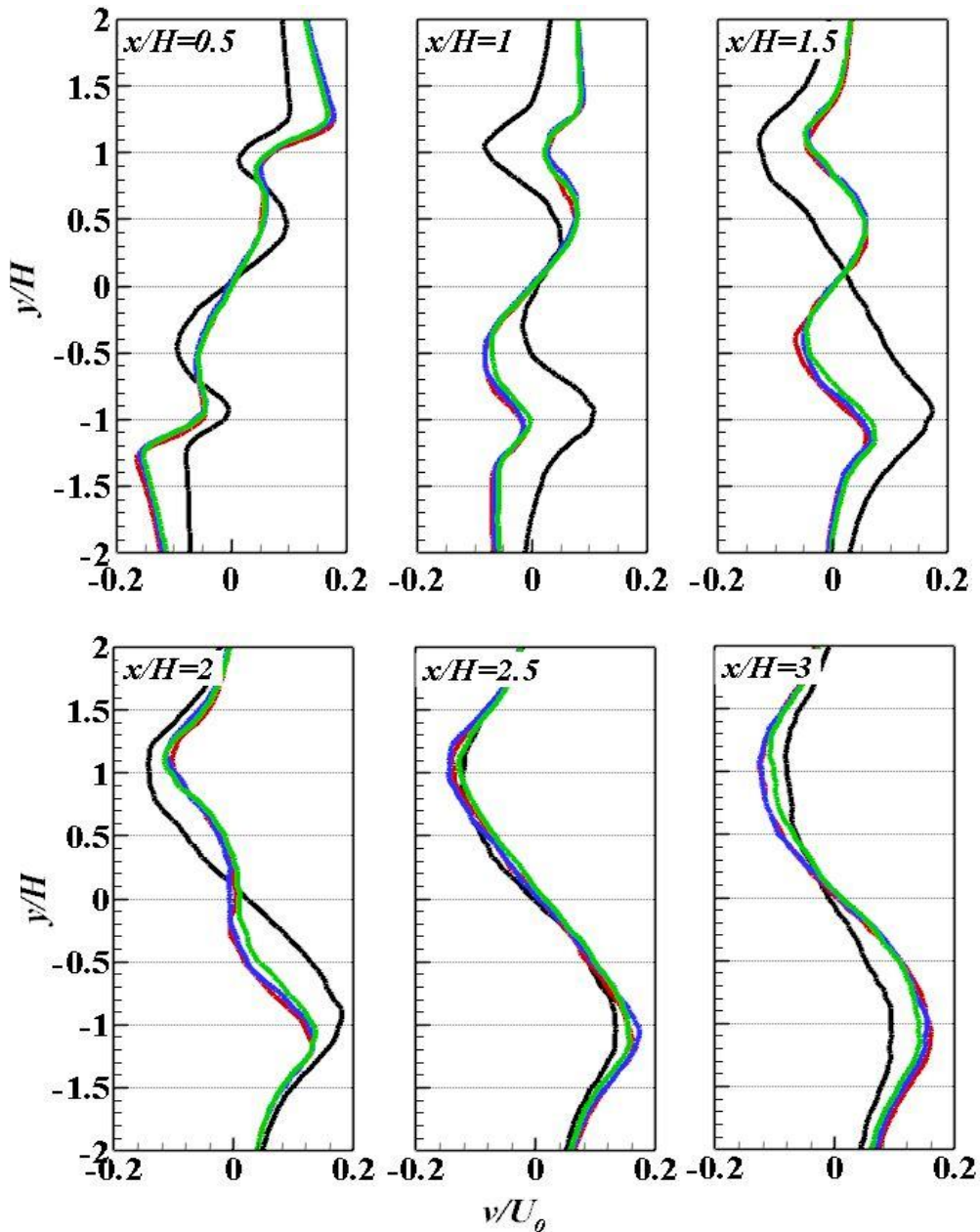


Figure 4.10 Mean cross-stream velocities at different axial locations generated by the square cylinder. black line: solid; green line: porous 60 PPI; blue line: porous 40 PPI; red line: porous 20 PPI

4.3.2 Reynolds Stresses for Square Cylinders

Profiles of the normal and shear Reynolds stresses normalised by the square of the freestream velocity downstream of square cylinders are illustrated in Figures 4.11, 4.12 and 4.13. For the solid case, the value of $\overline{u'u'}$ near the centreline is very small in the near-

wake at $x/H = 0.5$ and gradually develops with distance. The development of the whole profile is visible at $x/H =$, which indicates the existence of vortex recirculation region, in agreement with that observed in Figure 4.8. The maximum value of $\overline{u'u'}$ for the solid cylinder is observed at $x/H = 1$, close to the vortex centre. The $\overline{u'u'}$ term then reduces with distance beyond the vortex centre. The $\overline{u'u'}$ profile peaks at the shear layer, similar to the results for the circular cylinders. The peak for the solid case is observed at $y/H \approx \pm 1$ in the near-wake, which then contracts and reaches to $y/H \approx \pm 0.5$ further downstream. For the porous cases, the maximum value of the $\overline{u'u'}$ can be seen at $x/H = 2.5$ near the vortex centre. The peak amplitude for the porous profiles in the near-wake is almost half of that for the solid case. Also, the peak location for the porous cases changes from $y/H \approx \pm 1.1$ in the near-wake to $y/H \approx \pm 0.75$ in the far wake region.

The normal Reynolds stress in the vertical direction, $(\overline{v'v'})$ induced by the solid cylinder has a small value in the near-wake, and then increases downstream. The $\overline{v'v'}$ component of the Reynolds stress is negligible up to $x/H = 1$ for all the porous cases, and then gradually increases. The growth of the profiles for different porous treatments is almost the same upstream of $x/H = 2$. Downstream of this location less growth is seen for the less permeable materials. The largest reduction for the $\overline{v'v'}$ component is achieved for the 20 PPI case. The shear stress $(-\overline{u'v'})$ at the shear layer for all the porous cases is less than the solid case in the near-wake. The reduction in shear stress value is more significant in the far wake locations.

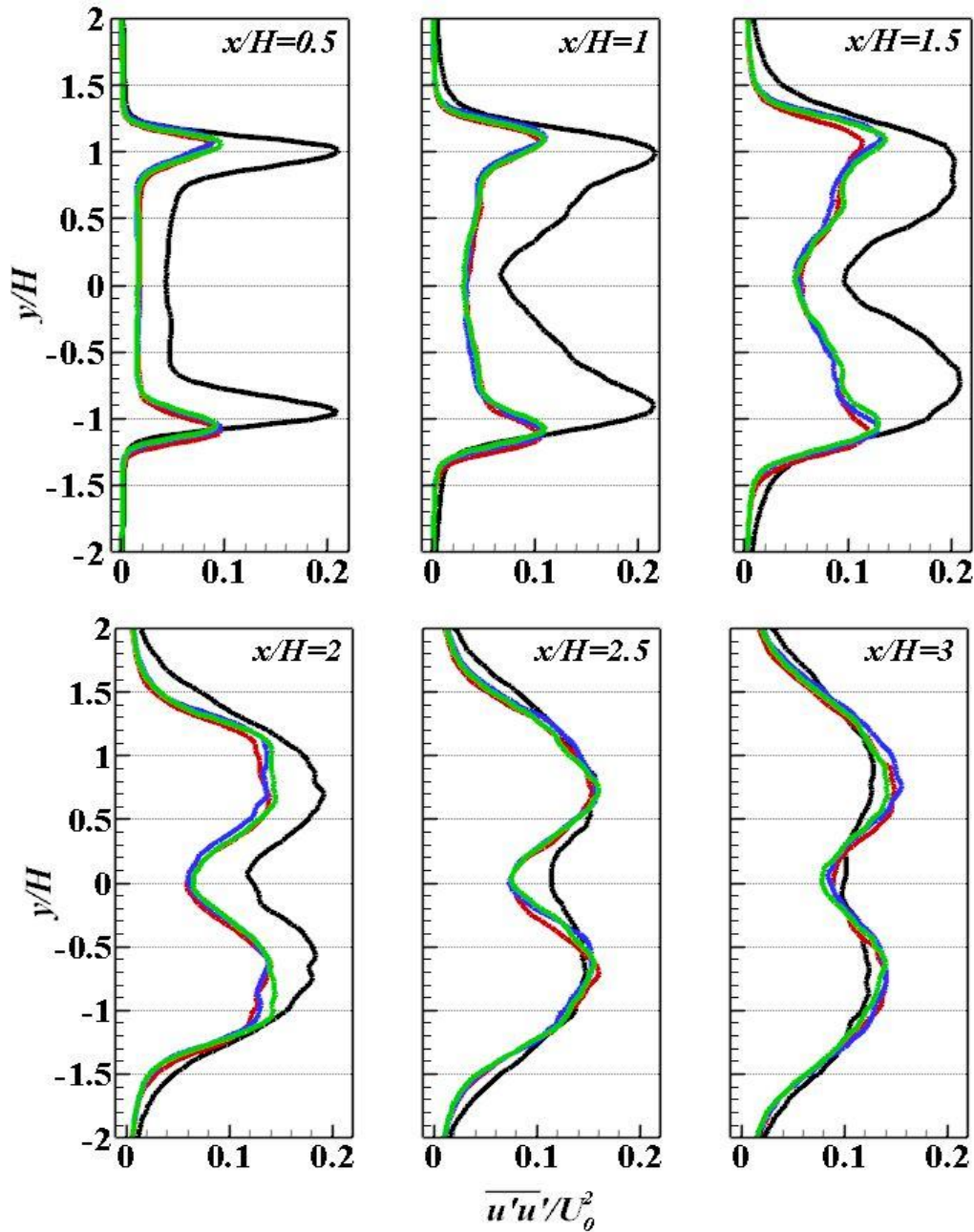


Figure 4.11 Normal Reynolds stress components in the wakes of the square cylinders. black line: solid; green line: porous 60 PPI; blue line: porous 40 PPI; red line: porous 20 PPI

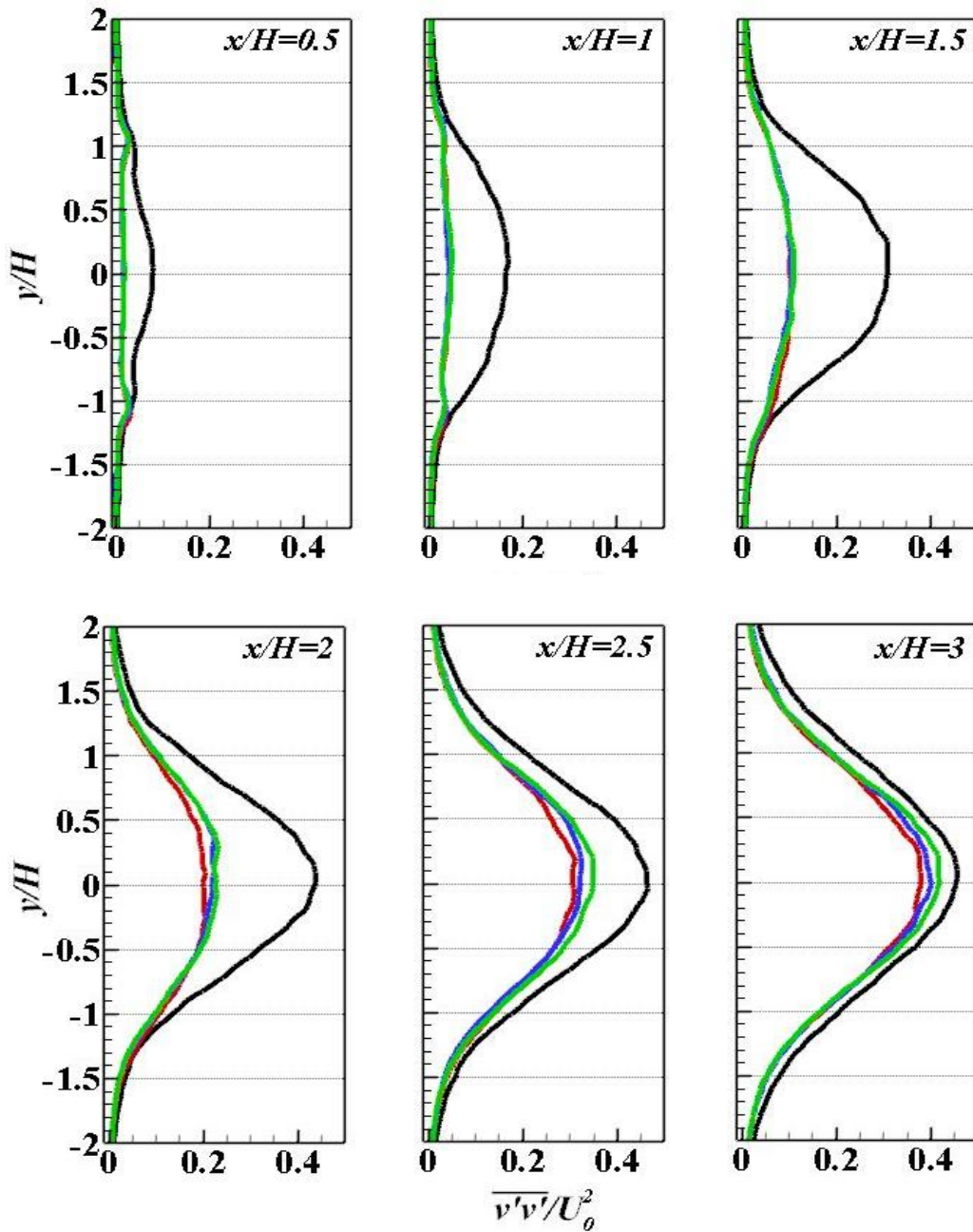


Figure 4.12 Normal Reynolds stress components in the wakes of the square cylinders. black line: solid; green line: porous 60 PPI; blue line: porous 40 PPI; red line: porous 20 PPI

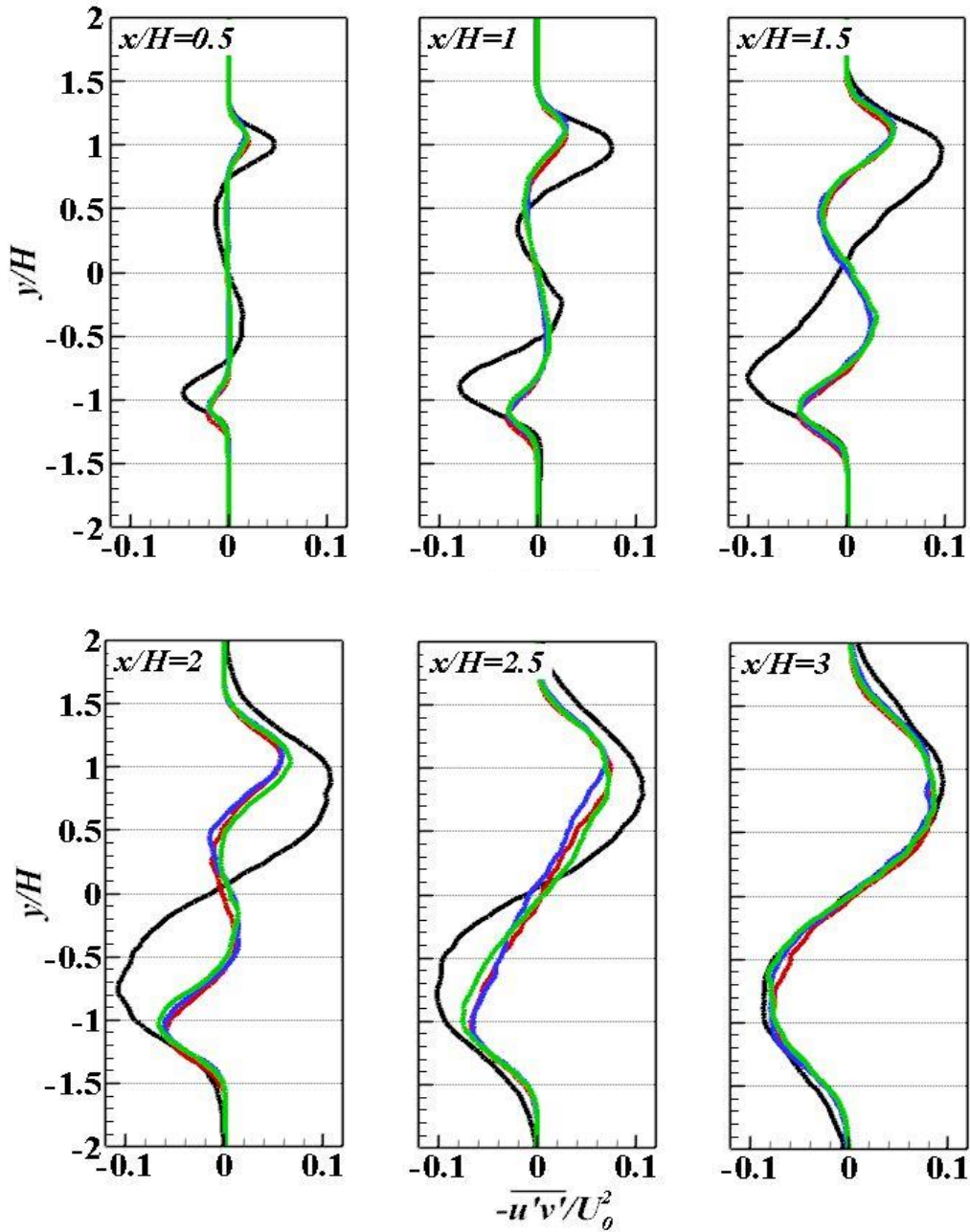


Figure 4.13 Shear Reynolds stress components in the wakes of the square cylinders. black line: solid; green line: porous 60 PPI; blue line: porous 40 PPI; red line: porous 20 PPI

4.4 Rectangular Cylinder

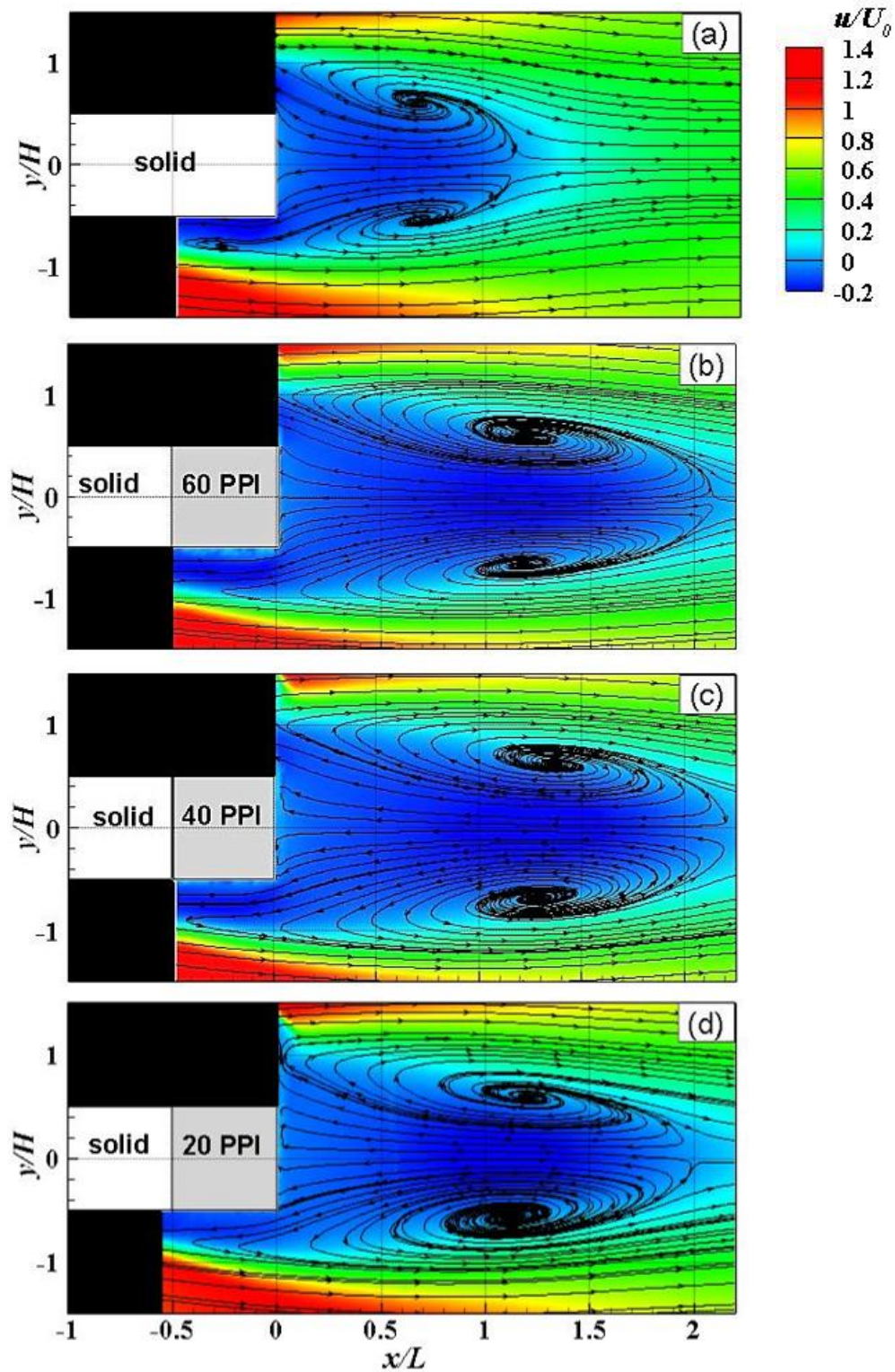


Figure 4.14 Time-averaged streamlines generated by rectangular cylinders; (a) bare cylinder, (b) cylinder treated with 60 PPI porous layer, (c) cylinder treated with 40 PPI porous layer and (d) cylinder treated with 20 PPI porous layer

Figure 4.14 demonstrates the time-averaged streamlines for the solid and porous-treated rectangular cylinders. It is observed that the recirculation zone for the solid rectangular cylinder, the reference model, terminates at $x/L \approx 1.15$. Here again, the existence of porous material at the downstream end of the cylinder shifts the vortex formation further downstream from the cylinder. The non-dimensional recirculation lengths for different porous cases expand and reach to a value between about 1.95 and 2.2. The furthest location of the vortex centres in respect to the trailing edge of the cylinder as well as centreline is noticed for the 40 PPI porous material. The displacement with respect to the reference model is from 0.7, 0.7 to 1.28, 1.37 and from -0.5, 0.6 to -0.7, 0.63 in stream-wise and cross-wise directions, respectively.

4.4.1 Velocity Components for Rectangular Cylinders

Figures 4.15 and 4.16 gives non-dimensional velocity distributions for the rectangular configurations in the stream-wise and cross-wise directions, respectively. From the u/U_0 profiles presented in the figure, a flat top hat profile is observed in the near-wake of the solid cylinder, which transforms into a parabolic profile at $x/L = 0.5$, immediately before the eyes of the vortex. The profile grows over the vortex region and then weakens until it becomes almost vertical line at $x/L = 2$, where the flow is nearly uniform. For the porous cases, the change from flat top hat profile to parabolic profile occurs more slowly at $x/L = 0.75$, increasing downstream in the vortex region. Unlike the square cylinder cases, the cylinder treated with the 20 PPI porous material shows the least decrease in the value of stream-wise velocity over the entire wake region. A reversed flow region begins at $x/L = 0.75$ in the cross-stream velocity profile for the solid cylinder. The reversed cross-stream velocity then reduces in value further downstream.

The emergence of the reversed flow in the v/U_0 profile downstream of the porous cylinders can be seen at $x/L = 1.5$. This phenomenon is consistent with the delay in the formation of the vortex structures, as seen in Figure 4.14.

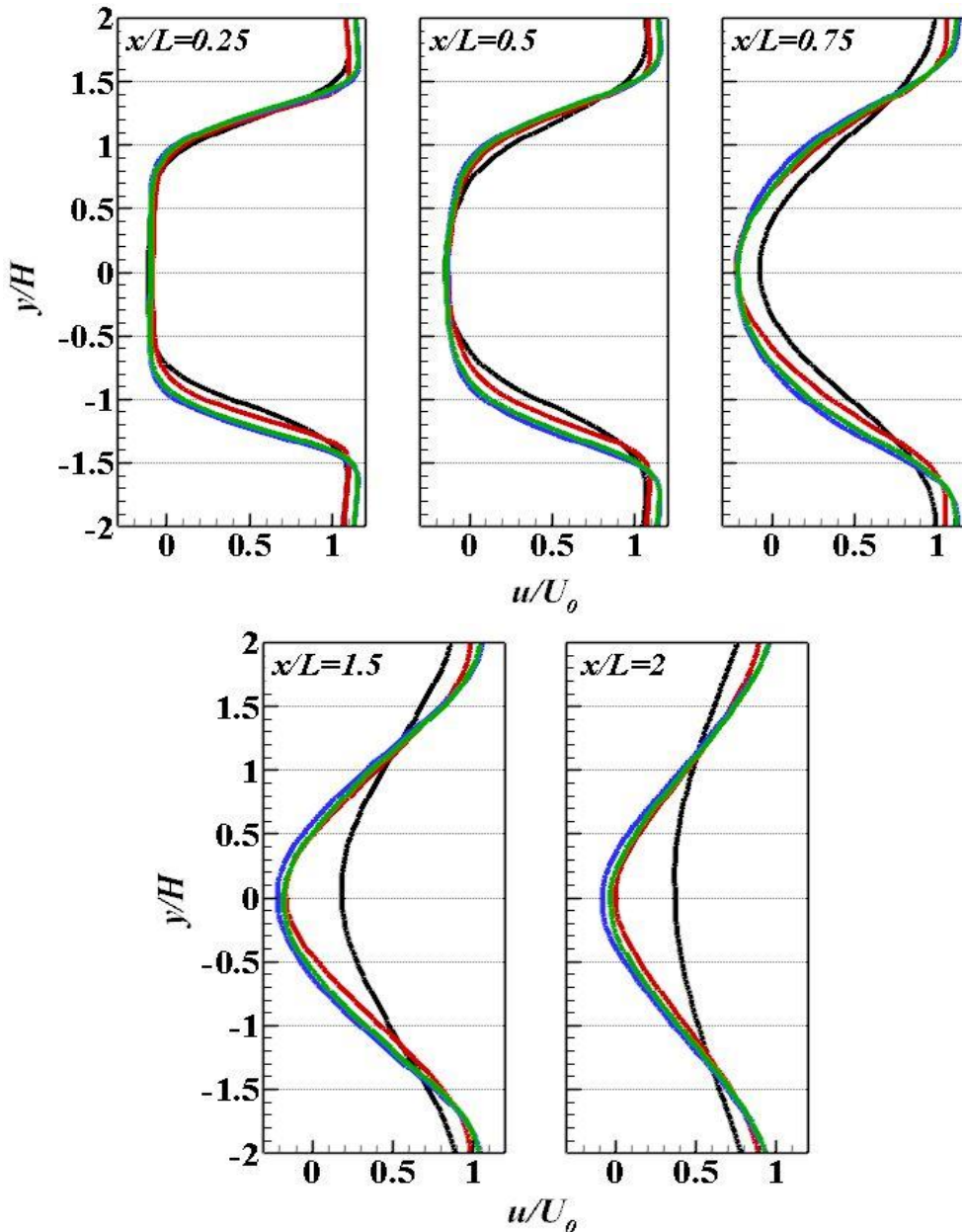


Figure 4.15 Mean stream-wise velocities at different axial locations from rectangular cylinder. black line: solid; green line: porous 60 PPI; blue line: porous 40 PPI; red line: porous 20 PPI

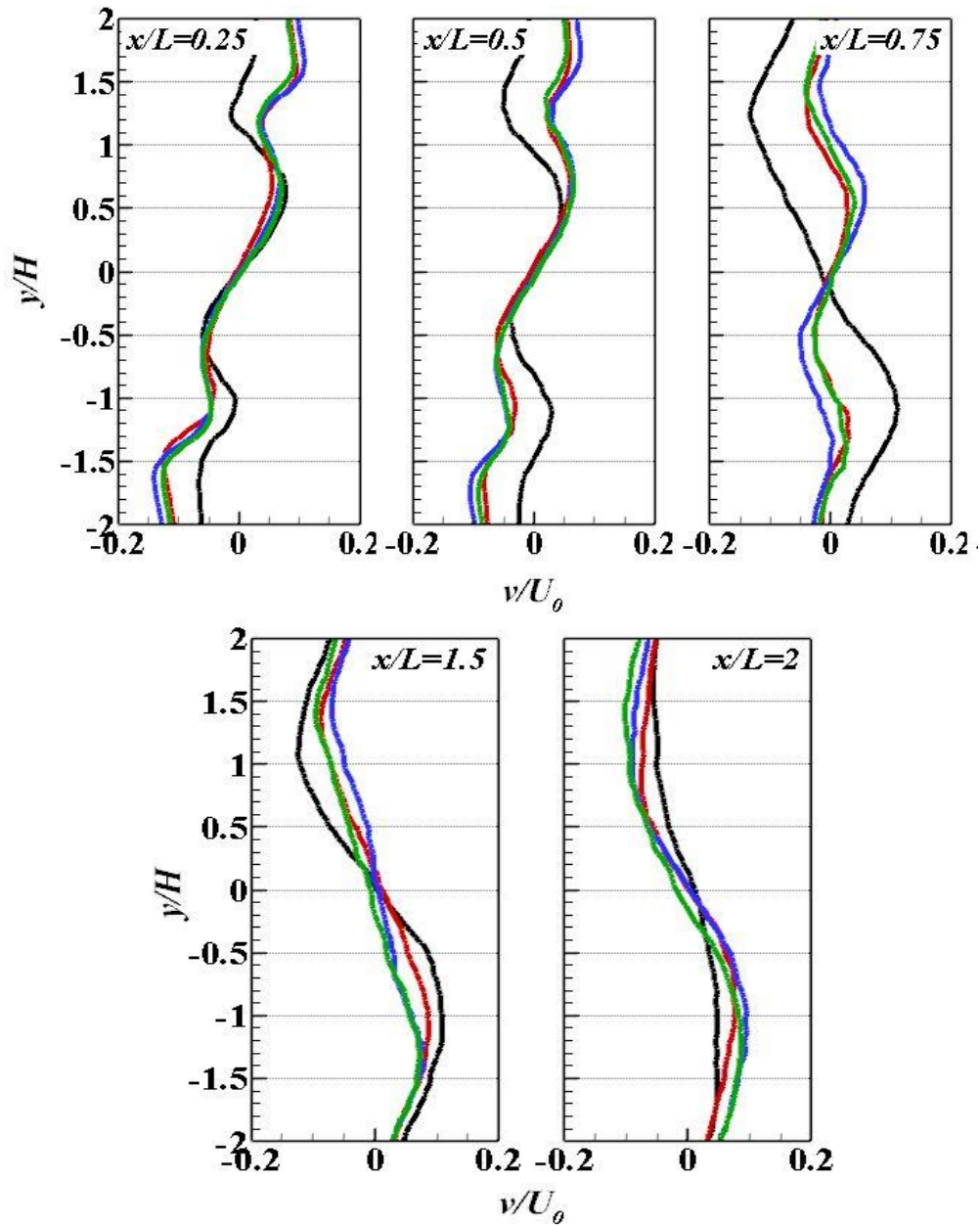


Figure 4.16 Mean cross-stream velocities at different axial locations from rectangular cylinder. black line: solid; green line: porous 60 PPI; blue line: porous 40 PPI; red line: porous 20 PPI

4.4.2 Reynolds Stresses for Rectangular Cylinders

Normal Reynolds stresses in the stream-wise and cross-wise directions and the shear Reynolds stress for the rectangular configurations are shown in Figures 4.17, 4.18

and 4.19. The value of $\overline{u'u'}$ for the solid case increases from $x/L = 0.5$ with the greatest growth occurring closely after the vortex centre location at $x/L = 0.75$. It then decreases towards downstream where the recirculation zone ends. The peak of the profile occurs within the shear layer at $y/H \approx +1.2, -1.1$ near the solid cylinder and reduces to $y/H \approx \pm 1$ further downstream. Here, in contrast to the circular and square cases, the peak location for the 20 PPI porous case is closer to that of the solid case. The peak location for the 40 PPI porous case, at $y/H \approx \pm 1.3$ in the near-wake and $y/H \approx \pm 1.2$ in the far wake, shows the greatest deviation from the solid case.

The profile of the $\overline{v'v'}$ component for the porous cases does not change appreciably with distance. The amplitude of the $\overline{v'v'}$ normal stress component is substantially reduced when a porous material is used. The reduction in the turbulent kinetic energy (TKE) in porous cases mostly arises from the reduction in the $\overline{u'u'}$ component in the near-wake, and the $\overline{v'v'}$ component in the far wake. Here, the shear stress ($-\overline{u'v'}$) is dominant after $x/L = 0.75$, and further downstream it behaves the same as in the wake induced by the bare rectangular cylinder. A reduction in shear stress ($-\overline{u'v'}$) at the shear layer in the near-wake can also be seen, which is greater than that in the square cylinder cases. The shear stress decreases remarkably in the far wake region, implying less production of turbulence.

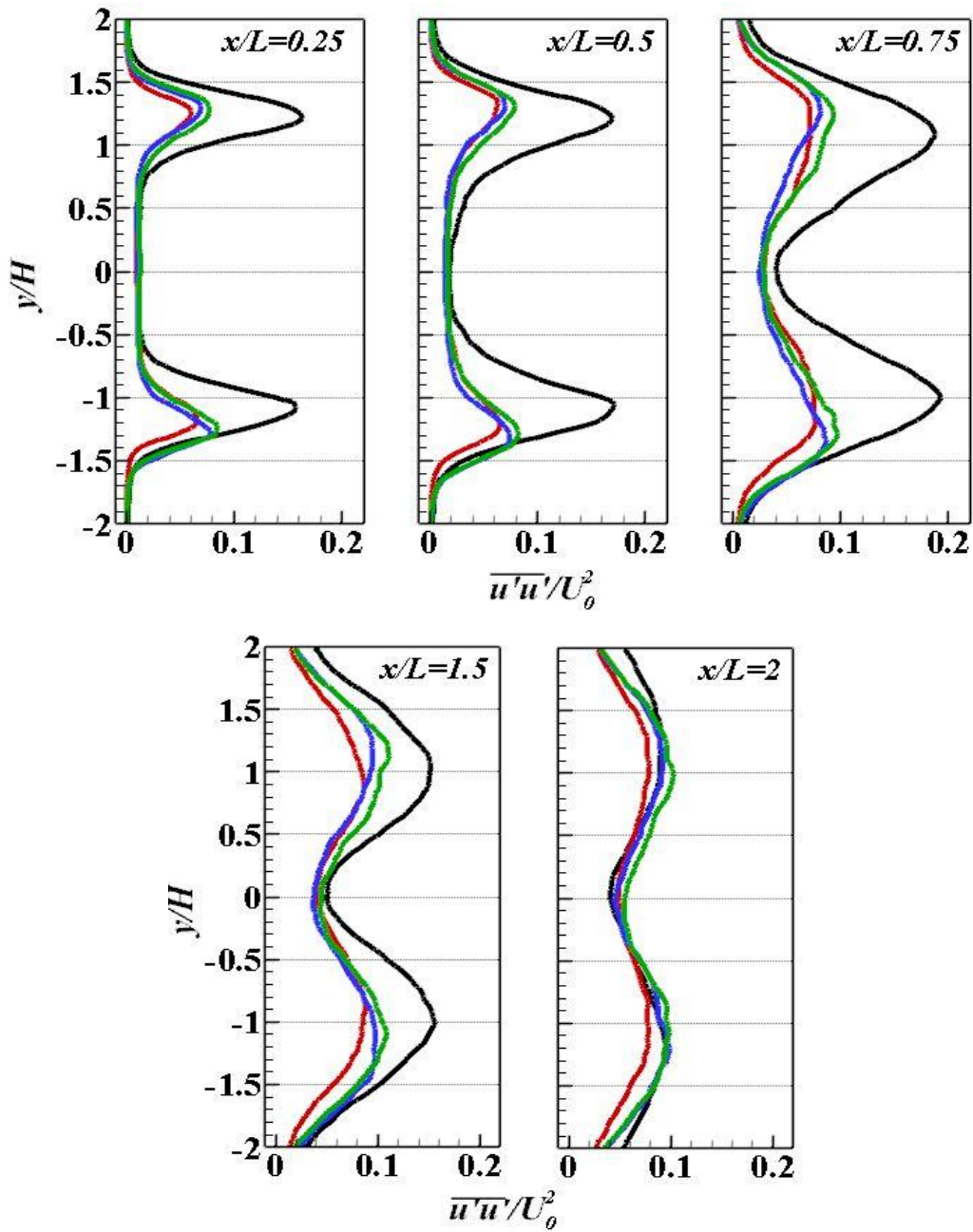


Figure 4.17 Reynolds stress components in the wakes of the rectangular cylinders. black line: solid; green line: porous 60 PPI; blue line: porous 40 PPI; red line: porous 20 PPI

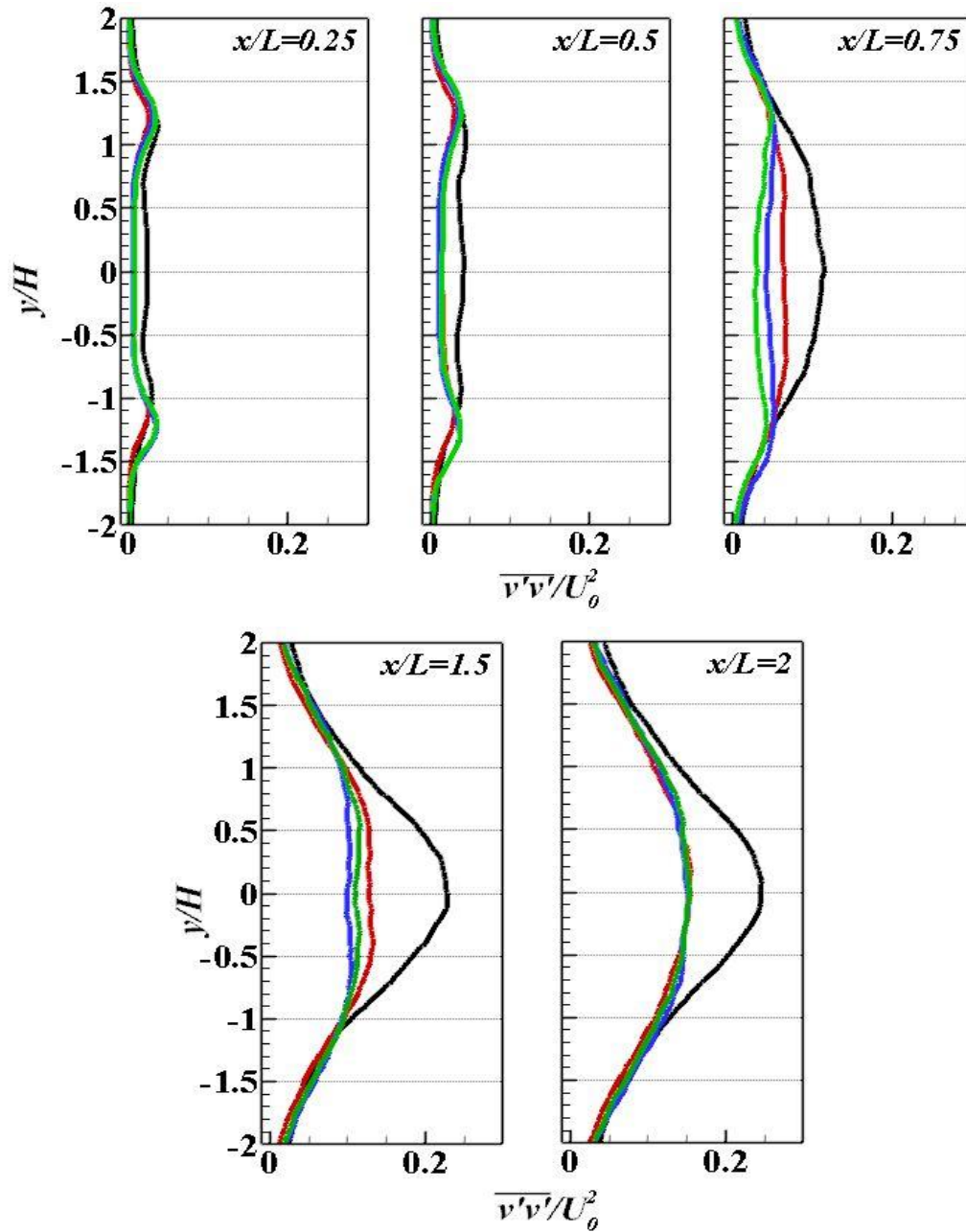


Figure 4.18 Reynolds stress components in the wakes of the rectangular cylinders. black line: solid; green line: porous 60 PPI; blue line: porous 40 PPI; red line: porous 20 PPI

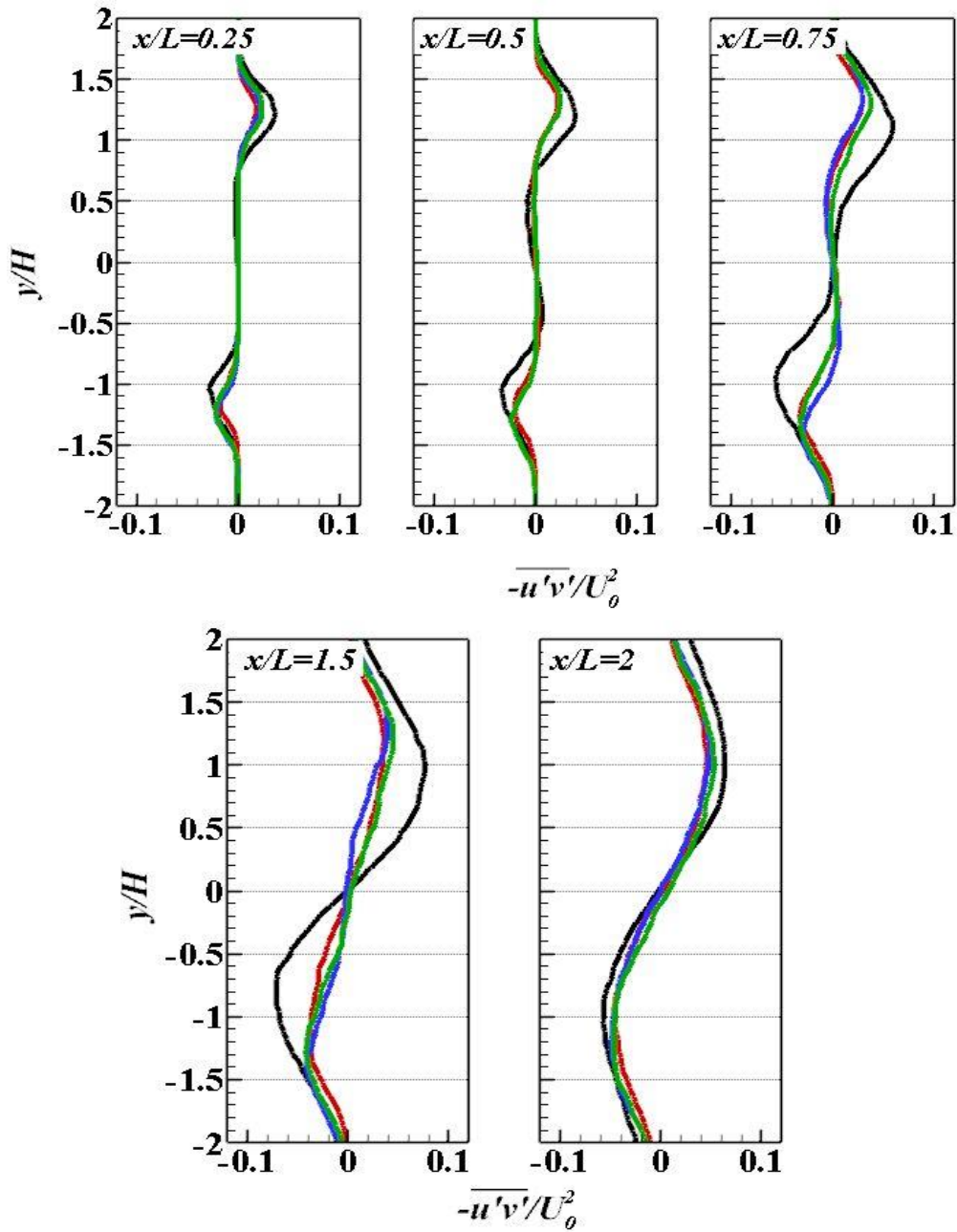


Figure 4.19 Reynolds stress components in the wakes of the rectangular cylinders. black line: solid; green line: porous 60 PPI; blue line: porous 40 PPI; red line: porous 20 PPI

4.5 Drag Coefficients from Experimental Results

The drag coefficients for solid and porous-treated cylinders were indirectly determined by using the integral momentum equation. Due to symmetry, the problem can be considered two-dimensional. The change in momentum is used to calculate the drag force and hence the drag coefficient. The upstream flow with the uniform velocity of U_0 moves around the cylinder, where its pressure reduces, thereby creates a low-pressure region downstream the cylinder, which causes the drag force. The velocity profile downstream the cylinder is no longer uniform and can be defined as $U(x, y)$, which merges into the external velocity U_0 at $y = \delta(x)$. By using a control volume around the cylinder, as shown in Figure 4.20, and the momentum integral relation, the drag force can be calculated.

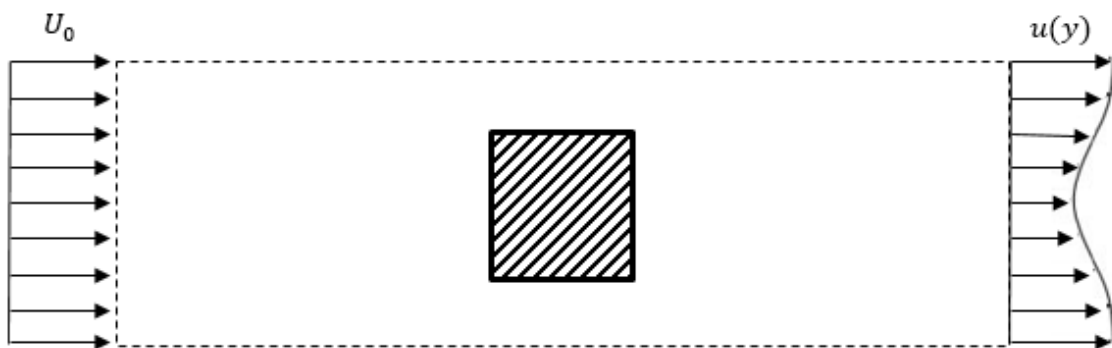


Figure 4.20 The control volume around the cylinder to calculate the drag coefficient based on the integral momentum equation.

The drag coefficient for the cylinder is calculated from the following equation as suggested by White (2011):

$$C_D = \frac{2}{L} \int_0^\delta \frac{u(y)}{U_0} \left(1 - \frac{u(y)}{U_0}\right) dy, \quad (4.2)$$

where C_D is the drag coefficient, L is the length of the cylinder, $u(y)$ is the velocity profile at the downstream end of the control volume and δ is where the flow velocity reaches the upstream flow velocity. The calculated drag coefficients for circular, square and rectangular cylinders based on the experimental data are presented in Table 4.1. The data shows that the maximum drag reduction of 32.5% is obtained for a circular cylinder when a 20 PPI porous layer replaces half the diameter of the cylinder. The minimum drag reduction for the circular cylinder is obtained with the porous material with 60 PPI. For the square cylinder, a maximum drag reduction of 13% and a minimum of 7.3% is obtained when the downstream half of the cylinder is replaced by porous materials with 20 PPI and 60 PPI, respectively. For the rectangular cylinder with the same treatment as the square case, the maximum reduction in drag coefficient is achieved with the 40 PPI porous material by about 12.5% and the porous material with 20 PPI gave the minimum drag reduction of about 8%.

Table 4.1 The drag coefficients for the flow around solid bare circular, square and rectangular cylinders and circular, square and rectangular cylinders with porous materials at their trailing halves calculated by the integral momentum method.

Circular cylinder	$C_{D, \text{circular}}$	Square cylinder	$C_{D, \text{square}}$	Rectangular cylinder	$C_{D, \text{rectangular}}$
Solid	0.83	Solid	1.50	Solid	1.12
60 PPI	0.62	60 PPI	1.30	60 PPI	1.01
40 PPI	0.60	40 PPI	1.36	40 PPI	0.98
20 PPI	0.56	20 PPI	1.39	20 PPI	1.03

4.6 Conclusions

The most discernible effect of the porous media is that compared with the wakes generated by the plain cylinders the circulation bubbles are displaced downstream in each of the cases considered. This effect is most apparent in the case of flow over circular cylinders. The most likely reason for this is that the fluid is able to enter the porous media on the upstream face of the cylinder. In the case of the square and rectangular cylinders the flows are modified only as a result of the porous media in the downstream half of the bodies. In the case of the circular cylinders, the downstream displacement of the circulation bubbles increases as the permeability increases. This effect is less apparent in the cases of the square and rectangular cylinders.

It is observed that the fluid penetrates the high permeability porous layer enveloping the circular cylinder, and there is implied evidence that this occurs in all of the cases studied. For example, the Reynolds stresses are much reduced by the presence of the porous media, and this is particularly apparent in the cases of the flows within about two diameters of the downstream edges of the bodies. It is likely that this is due to the fluid penetrating the porous media with the result that the turbulence is dampened.

CHAPTER 5

COMPUTATIONAL MODEL AND MATHEMATICAL FORMULATIONS

5.1 Introduction

Fluid flow problems have been traditionally analysed by performing experimental investigations, mainly in wind tunnels. The visualisations of the fluid flow together with complementary experimental findings inspired a number of mechanistic or constitutive models of fluid flow. The models were expressed mathematically, but they were subject to the conservation laws of mass, momentum and energy. There are engineering problems, which are large in size and wind tunnel experiments seem impossible or far too expensive to be practical. Here, one thinks of the design of supersonic aircraft, perhaps. In addition, even for a simple problem and a feasible experimental procedure, repetition of the experiments to test the effect of a range of variables is a laborious and expensive effort. Furthermore, the equations of conservations contain a system of coupled partial differential equations, which are impossible to solve analytically in anything but the simplest of problems. These limitations motivated the use of a faster and less expensive method to analyse physical phenomena. The establishment of comprehensive mathematical formulations and advent of computers resulted in the use of numerical simulations of the problems with the utilisation of Computational Fluid Dynamics (CFD).

In CFD, numerical solution techniques are developed to solve the system of coupled partial differential equations to produce quantitative predictions or analysis of fluid flow phenomena. The basic objective of this tool is to solve approximately the flow and basic equations that give us the movements and other characteristics of the flow. CFD plays an important role in modelling and design of fluid systems, as it is cost-effective and leads to shorter design cycles. The emergence of supercomputers and advancement of computer hardware resulted in more reliance on the numerical simulations and accelerated the CFD research in the past decade.

In the experimental part of this work, cylinders with circular, square and rectangular cross-sections have been tested. Experiments were carried out on solid aluminium cylinders, and these provided results that may be considered as benchmarks. Further sets of experiments were carried out on cylinders with the same geometries as those fabricated from solid material, but parts of them consisted of open cell porous media. Three different porous media were used for the porous component, each of which had a different permeability. The flow structures over the porous-treated and corresponding solid cylinders have been compared. Due to the limitations in time, it has been decided to use numerical investigations to expand the study.

The experimental work carried out in this research on the circular cylinders were used to validate the experimental set up based on the previous work. The results were also used for the validation of the numerical model in the present work. However, as extensive studies exist on porous-covered circular cylinders, this configuration was not considered for further numerical investigations. Moreover, results of the experiments for the square and rectangular cylinders showed similar effects of porous surfaces on the flow control. In addition, the experimental results for the square cylinder was obtained for a wider ratio

of stream-wise dimension to diameter, showing the entire recirculation region plus the following streamlined region. This provides sufficient data for the purpose of comparison of the numerical work with the experiments. Therefore, square cylinder was selected among these configurations to perform additional studies for further investigating the flow structure in the presence of a porous material. As one might anticipate, the 20 PPI porous material was found to have the most effect on the flow structure. Therefore, the 20 PPI porous material with a measured permeability equal to $4.64 \times 10^{-7} \text{ m}^2$ and a resistance loss coefficient equal to 1658 m^{-1} is used for the simulations.

This chapter discusses the numerical model and procedure for the simulation of the flow over square cylinders with and without porous treatment. A motivation to use numerical simulations was the ability of simulations in providing cost effective results. The primary aim was to implement and validate a numerical model to be used in the simulations of porous materials. Once the code is validated, various investigations can be performed on the geometry of interest without the need to constructing new geometries and running expensive experiments. Therefore, the effect of different dispositions of porous material on the flow could be investigated. Another motivation was to gain more insight into the flow behaviour than what we have obtained from the experiments. Additional information about the flow structure such as boundary layer data and pressure field was sought.

In the next sections, selected configurations for the simulation studies are presented. Governing mathematical equations describing fluid flow around solid objects and inside and around porous materials as well as the methods for solving the equations are discussed. Details of the three-dimensional numerical model and the turbulence model used in this research for the study of the flow around the cylinders are also presented. The

numerical procedure has been implemented using the CFD code, CFX. The code is validated against the experimental data presented in Chapter 4.

5.2 Bluff Body Configurations

Chapter 5 presented experimental results for a bare square cylinder and square cylinders with porous materials that formed their trailing halves. These configurations are studied in more detail using numerical simulations. Moreover, the flow over porous-treated square cylinder is further investigated by replacing the leading-half of the square with porous material. The motivation behind the disposition of porous material was to investigate and compare the flow fields and drag coefficients. The idea was that when the porous material is located at the upstream half of the cylinder, the flow penetrates the porous layer in the leading edge and loses its velocity. Hence, the flow strikes the solid part at a lower velocity. In addition, the change in the separation point and shorter solid length affects the recirculation on the upper and lower edges of the cylinder, which in turn may affect the large recirculation bubbles in the wake of the cylinder. This idea is explored in Chapters 5 and 6. The configurations considered for the simulations are presented in Figure 5.1.

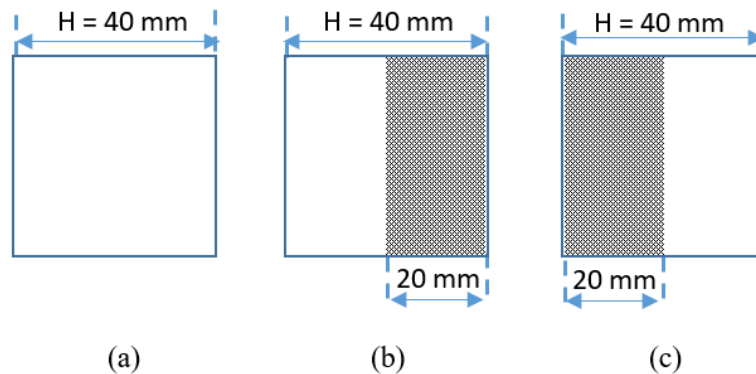


Figure 5.1 The square cylinders used in the numerical simulations; a) bare cylinder used as the reference, b) the square cylinder treated with 20 PPI porous material at its trailing half, c) the square cylinder treated with 20 PPI porous material at its leading half.

5.3 Numerical Procedure

The computational fluid dynamics (CFD) code, ANSYS CFX is used to simulate the flow over cylinders of square cross-sections with and without porous material. The simulations are performed at a Reynolds number of 5.3×10^4 based on the height of the cylinder (H) and the free stream flow velocity (U_0). Full three-dimensional computations are performed for flow over the cylinders. SST turbulence model is implemented and is verified by comparison to the PIV experimental data presented in Chapter 4. The decision to use SST turbulence model has made upon examining two different turbulence models: $k - \varepsilon$ and SST from Reynolds Averaged Navier Stokes Equations (RANS). Comparing the results revealed that flow prediction by the SST model is closer to the results obtained from the experiments. This observation agreed with findings from Ünal *et al.* (2010) who concluded that SST provides better agreement with experimental data when they evaluated four RANS-based turbulence models for the flow over a circular cylinder. This section introduces the formulations that are used in ANSYS CFX to model the solid, fluid and porous materials. The governing flow equations and the methodology behind RANS turbulence models and SST model in particular are presented in detail.

5.3.1 Mathematical Formulations

For the cases investigated in this research, an incompressible viscous flow of a Newtonian fluid is considered. This type of flow is governed by the three dimensional Navier-Stokes equation. The conservation of mass is governed by Eq. (5.1) and Eq. (5.2) accounts for the conservation of momentum in the Cartesian coordinates for constant density and viscosity when gravity effects are neglected.

$$\frac{\partial u_i}{\partial x_i} = 0, \quad (5.1)$$

$$\frac{\partial u_i}{\partial t} + \frac{\partial u_i u_j}{\partial x_j} = -\frac{1}{\rho} \frac{\partial p}{\partial x_i} + \nu \left(\frac{\partial^2 u_i}{\partial x_i \partial x_j} \right), \quad (5.2)$$

where, $u_i (i = 1, 2, 3)$ are the velocity components in the direction of x , y and z , ρ is the fluid density and ν is the fluid kinematic viscosity.

- **Porous Material**

The isotropic momentum loss model was used to model the flow in porous media in ANSYS CFX. The model consists of a fluid domain together with a model for momentum loss, which represents the effects of porosity. All other terms in the governing equations remains unchanged. Hence, the formulation is called the superficial velocity formulation. The volume effect of porosity has been included, in which a porous domain has been created and the loss model details has been set on the domain details. The formulation of the momentum loss within an isotropic region based on the permeability and loss coefficients is:

$$\bar{M} = -\frac{\mu}{k} \bar{V} - \frac{1}{2} \rho c |\bar{V}| \bar{V}, \quad (5.3)$$

where, μ is the dynamic viscosity of the fluid, k is the porous media permeability and c is the quadratic loss coefficient of the porous material. The linear term of the momentum source formula accounts for viscous losses and the quadratic part of the equation represents inertial losses. The permeability and loss coefficients used in the simulations were $4.64 \times 10^{-7} \text{ m}^2$ and 1658 m^{-1} , respectively, obtained from the experimental

results discussed in section 3.3.2 of Chapter 3. In addition, the interface between the porous layer and fluid was manipulated by considering a continuity in the velocity and stress terms at the interface.

5.3.2 Shear Stress Transport (SST) Turbulence Model

The flow of fluids in our daily life are mainly turbulent. Examples are flow around bluff bodies such as cars, aircrafts, ships and buildings. The boundary layer and the wake around and downstream of these bluff bodies are turbulent. Although no particular definition exists for turbulent flow, a number of features is attributed to these types of flows (Pope 2000). Turbulent flows are irregular and chaotic and occur at high Reynolds numbers, they are different in internal and external flows. In addition, turbulent flows are always three-dimensional, unsteady and random. The flow contains a wide range of scales or eddy sizes. The largest turbulent eddies extract their energy from the mean flow and this energy is transferred to smaller eddies. The process continues to form smaller eddies in which the flow is viscous, and which ultimately results the energy transferred to the large eddies being dissipated as thermal energy. This transfer of energy from large eddies to smaller ones is the so-called cascade process stemming from the dissipative nature of turbulent flow (Pope 2000). The combination of velocity gradients and the formation of eddies in turbulent flows result in an increase in the rate of exchange of momentum, and as a result an effective or turbulent diffusivity is defined. The increased momentum exchange in a boundary layer, for example, results in a delay in the separation of flow around cylinders. Turbulent flows are governed by the Navier-Stokes equation (Eq. 5.2). Numerical solution to the Navier-Stokes equation requires both a very fine mesh to resolve all turbulent scales and fine resolution in time to account for the unsteady nature of turbulent flow. Therefore, it is preferred to utilise ensemble averaging in which the

instantaneous variables such as velocity and pressure are decomposed into a mean value and a fluctuating value. This procedure leads to Reynolds Averaged Navier-Stokes (RANS) equations. Details on the RANS equations are given in Appendix B, which can also be found in Menter (1994), Wu *et al.* (2014), Craft and Launder (1996).

The Shear Stress Transport model is a Reynolds Average Navier-Stokes (RANS) model, which is a combination of $k - \omega$ and $k - \epsilon$ models (see Davidson (2017) for details on the numerical models). The SST model uses $k - \omega$ model near the wall and $k - \epsilon$ model in the outer portion of boundary layer as well as outside the boundary layer region. The model utilises a blending function to perform the transition from the standard $k - \omega$ model in the inner boundary layer to a high Reynolds number version of the $k - \epsilon$ model in the outer region of the boundary layer. It contains a modified turbulent viscosity formulation to account for the transport effects of the principal turbulent shear stress. The SST model has been modified over the years to better reflect certain flow conditions (Davidson 2017). The final formulation of the SST model reads:

$$\begin{aligned} \frac{\partial k}{\partial t} + \frac{\partial}{\partial x_j} (\bar{u}_j k) &= \frac{\partial}{\partial x_j} \left[\left(v + \frac{v_t}{\sigma_k} \right) \frac{\partial k}{\partial x_j} \right] + P^k - \beta^* k \omega, \\ \frac{\partial \omega}{\partial t} + \frac{\partial}{\partial x_j} (\bar{u}_j \omega) &= \frac{\partial}{\partial x_j} \left[\left(v + \frac{v_t}{\sigma_\omega} \right) \frac{\partial \omega}{\partial x_j} \right] + \alpha \frac{P^k}{v_t} - \beta \omega^2 \\ &+ 2(1 - F_1) \sigma_{\omega 2} \frac{1}{\omega} \frac{\partial k}{\partial x_i} \frac{\partial \omega}{\partial x_i}. \end{aligned} \quad (5.4)$$

The empirical functions in the equations are defined as:

$$F_1 = \tanh(\xi^4), \quad (5.5)$$

$$\xi = \min \left[\max \left\{ \frac{\sqrt{k}}{\beta^* \omega d}, \frac{500\nu}{d^2 \omega} \right\} \frac{4\sigma_{\omega, k-\varepsilon} k}{CD_\omega d^2} \right], \quad (5.6)$$

$$CD_\omega = \max \left\{ 2\sigma_{\omega, k-\varepsilon} \frac{1}{\omega} \frac{\partial k}{\partial x_i} \frac{\partial \omega}{\partial x_i}, 10^{-10} \right\}, \quad (5.7)$$

$$v_t = \frac{a_1 k}{\max(a_1 \omega, |\bar{s}| F_2)}, \quad (5.8)$$

$$\eta = \max \left\{ \frac{2k^{1/2}}{\beta^* \omega d}, \frac{500\nu}{d^2 \omega} \right\}, \quad (5.9)$$

where, d is the distance to the closest wall node. The value of F_1 is equal to one near the walls and equal to zero far from the walls. The constants in the SST model are:

$$\beta^* = 0.09, \quad a_1 = 0.3,$$

$$\alpha_{k-\omega} = 5/9, \quad \beta_{k-\omega} = 3/40, \quad \sigma_{k, k-\omega} = 0.85 \quad \sigma_{\omega, k-\omega} = 0.5,$$

$$\alpha_{k-\varepsilon} = 0.44, \quad \beta_{k-\varepsilon} = 0.0828, \quad \sigma_{k, k-\varepsilon} = 1 \quad \sigma_{\omega, k-\varepsilon} = 0.856$$

SST turbulence model performs well in adverse pressure gradient flows. When the boundary layer tends to separate due to a changing pressure gradient, the SST model is recommended (Davidson 2017). The model is capable of accurately predicting the

pressure-drop, boundary layer velocity, and drag forces in most industrial applications (Eisfeld 2006, Menter 2009).

5.4 Computational Model Configuration

The first step in the pre-processing stage is to define a suitable geometry representing the problem under study. Defining the geometry can be achieved through computer aided design (CAD) or other available software specific to geometry creation. In addition to creating representations of the cylinders, it is necessary to define a domain enclosing the models representing the fluid that flows around and over the models. In creating the domain, the distance between the boundaries and the model must be specified. The boundaries must be sufficiently distant from the cylinder to prevent any effects of the boundaries on the flow domain and close enough to ensure that the computational time is reasonable given the computational resources available. The geometries considered in this work with and without porous material are created using ANSYS DesignModeler, an interface specifically provided for simulation.

The size of the computational domain in the stream-wise, cross-stream and span-wise directions shall be selected so that it represents the surrounding area and reflects the boundary conditions. A review of the literature shows that the size of a computational domain depends on the cylinder configuration and the numerical model used (Jue 2004, Valipour *et al.* 2014, Cao and Tamura 2016). Based on the applied domain sizes, a range of sizes has been tested for the current computations. The results obtained in each case were compared with the work in literature until the lowest deviations were achieved when the corresponding size was selected for the simulation of the test cases. The domain size tests have been performed in conjunction with a grid independency check, discussed in the next section. Eventually, a distance of $10H$ between the domain inlet and the centre

of square cylinders, and $21H$ from the outlet of the domain to the centre of cylinders provided the most reliable results.

The span-wise length is also an important concern, as it should provide the highest accuracy while maintaining the lowest possible computational cost. A span-wise length of 4 times the square length ($4H$) is opted in this work as it is commonly used in literature, for example Cao and Tamura (2016), Boileau *et al.* (2013) and Sohankar *et al.* (2000). The finalised dimensions of the computational domain are given in Figure 5.2 by showing the side view and top view of the domain.

Figure 5.3 shows a three-dimensional view of the entire computational domain enclosing a square cylinder treated with porous material at its leading half as an example of the numerical models in the DesignModeler environment. The horizontal and vertical planes passing through the sides of the square cylinder are the dividing planes for the construction of a structured mesh.

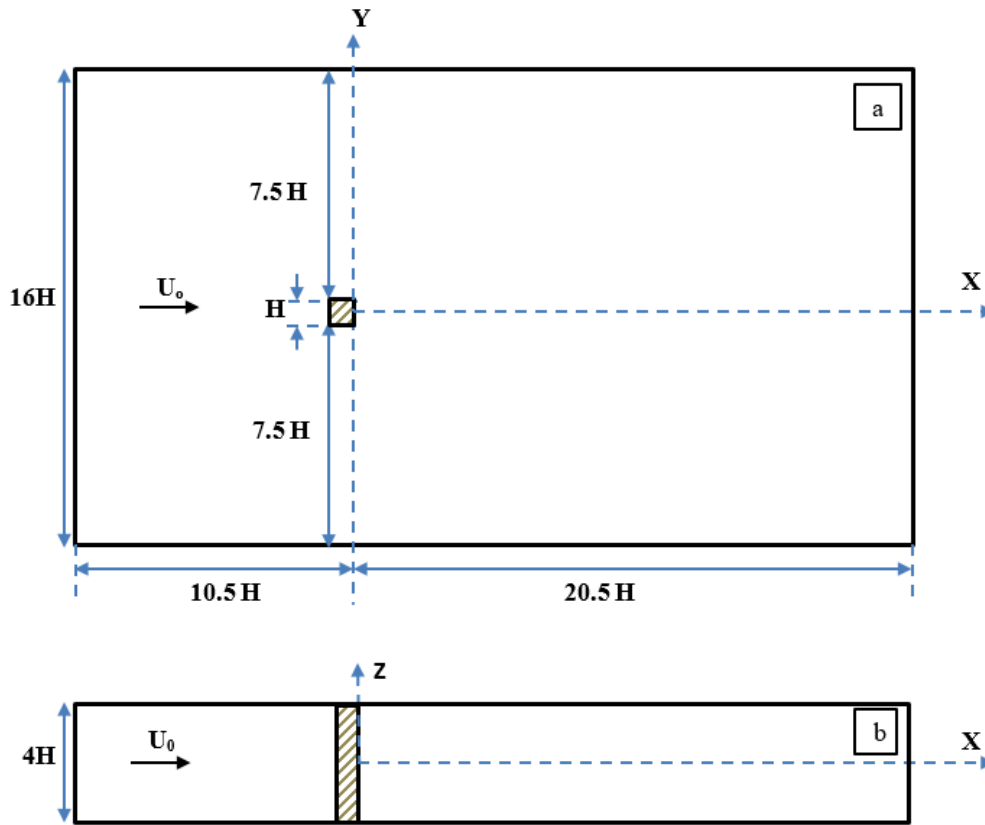


Figure 5.2 Schematic of the computational domain showing a) side view and b) top view containing the dimensions of the domain.

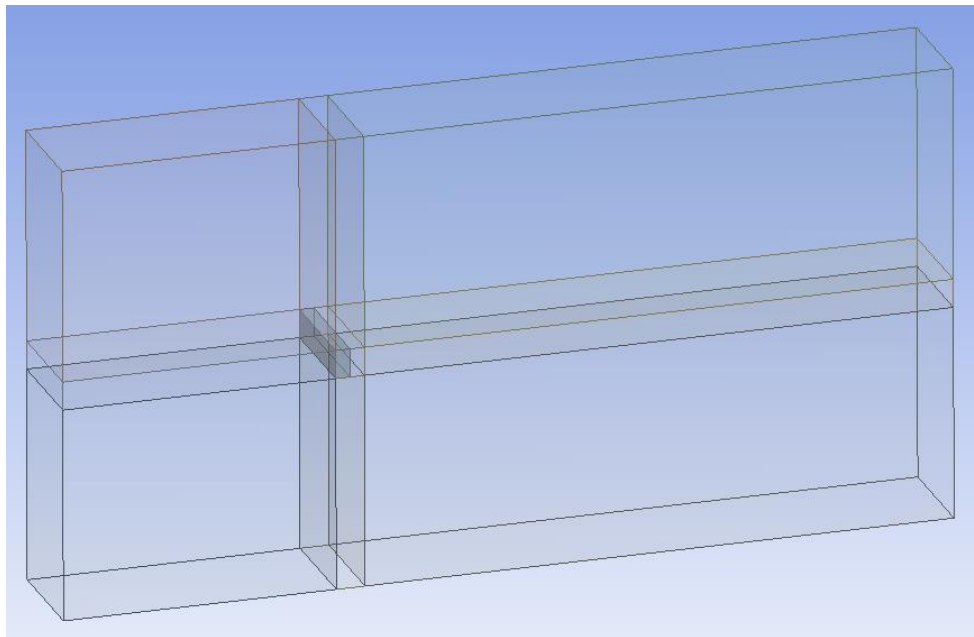


Figure 5.3 Perspective view of the model geometry in DesignModeler showing the square cylinder with its leading half comprising porous material.

5.5 Grid Generation

After creating the geometry, a suitable mesh has to be constructed. The meshing operation discretises the entire computational domain into sub-domains over which the governing equations are approximated. The generated discrete elements include nodes over which the flow parameters are resolved. The number of elements and nodes are key factors in the quality of the results and the computational costs. Efforts have to be made to establish a mesh with sufficient elements and nodes to capture the flow structures while minimising the numerical costs.

Finding the right balance between the accuracy of the results, stability of the simulation and the speed is challenging. Simulations with highly coarse meshes are time-efficient, yet may not return the correct solution depending on the complexity of the geometry. Overly fine meshes are not only time consuming but may also distort the solution depending on the turbulence model that is being used. In addition, turbulence models have restrictions on cell sizes in the wall region in regard to suitable values of the so called y -plus, the dimensionless wall distance presented in Eq. 5.14. Therefore, a well-constructed mesh has to be generated to ensure the quality of the solution. Accordingly, a reasonably coarse global mesh is commonly generated while paying more attention to certain areas of the geometry where the gradients are high. On this ground, the mesh near the walls and sharp edges needs to be refined to increase the fidelity of solutions in these areas.

Structured meshing as a common meshing used in bodies with a simple geometry, is implemented in the present simulations because it provides better convergence and higher resolution. Meshing of the computational domain is performed using the automated high-performance ANSYS Meshing. Both the DesignModeler and ANSYS

Meshing are included in ANSYS Workbench platform, which is fully integrated with CFX.

5.5.1 Mesh Structure at the Near Wall Region

In turbulent flows, the velocity fluctuations within the turbulent boundary layer can be a significant percentage of the mean flow velocity, therefore it is crucial to accurately capture these fluctuations. The influence of walls on the turbulent flow field can be discerned from the different regions in the turbulent boundary layer. In the viscous sub-layer, the inertial forces are tautologically negligible to viscous forces. Here, the flow exhibits laminar characteristics and hence the name Low-Reynolds number (low-Re) region applies. Inside the boundary layer and at the surface of a solid wall, the velocity is zero (no-slip condition). The flow velocity, following a log-law profile, increases in a normal direction to the wall. The flow velocity eventually reaches to that of the free stream at the edge of the boundary layer. In the log-law region, also known as high-Reynolds number (high-Re) region, inertial forces dominate and turbulent stresses increase in significance. In theory, full resolution of the flow inside the boundary layer requires a very fine mesh near the wall. However, very fine meshes suggest high computer power and additional computational time, which is not always possible, nor necessary. Turbulent models involve some approaches to capture the boundary layer with a certain accuracy without the need to an extremely fine mesh.

A Reynolds averaging approach using turbulence models will provide us with an estimate of the increased levels of stress within the boundary layer, termed the Reynolds stresses. A dimensionless parameter, y -plus (y^+) is commonly considered to control the mesh refinement in the near-wall region. y -plus represents the normal distance of the grid points from the wall and is calculated as follows. The y -plus needs to be in an acceptable

range for a particular turbulence model to be valid. This is to ensure that the mesh is consistent and the boundary layer region is correctly represented.

$$y^+ = \frac{\rho U_\tau \Delta y}{\mu}, \quad (5.10)$$

in which Δy is the wall adjacent grid height and U_τ is the frictional velocity defined as:

$$U_\tau = \sqrt{\frac{\tau_w}{\rho}}. \quad (5.11)$$

τ_w is the wall shear stress defined as:

$$\tau_w = \frac{1}{2} \rho c_f U_0^2. \quad (5.12)$$

c_f accounts for the skin friction coefficient. For external flows, an empirical estimation of the skin friction coefficient can be given as (White 2015)

$$c_f = 0.058 Re^{-0.2}. \quad (5.13)$$

In the present simulation a flow separation is expected, therefore resolving the viscosity dominated sub-layer needs to be done by the low-Re method to consider the viscous effects. The low-Re method is employed in SST model when the flow near a wall

is to be modelled. In other words, the SST model does not use any mathematical formulas to represent the boundary layer flow, but fully resolves the flow near to the wall. For the SST model to accurately resolve this region, an appropriate mesh resolution is required, especially where a separation in flow is expected. Here, the y -plus value needs to be on the order of around 1 ($y^+ \approx 1$) to ensure the laminar sub-layer is captured. However, the overall resolution of the boundary layer is the key to high quality results and is sometimes more important than achieving a certain value for y -plus. Therefore, when refining the mesh near wall region, the number of grids covering the boundary layer is an important factor that has to be taken into account. A minimum of ten grid cells in the boundary layer is required and twenty cells is desirable (ANSYS 2015), which has been carefully monitored in the present meshing.

To generate an acceptable resolution in the boundary layer, a function called sizing function has been used in the present work. The sizing function has been applied on the edges of the fluid domain, dividing plates and the sides of the square cylinders to control the growth of the cell heights from the cylinder walls to the outer region. To utilise this function, each edge has been divided into a certain number of divisions with a bias type to put greater number of divisions closer to the cylinder walls. The bias factor controls the growth of the cells from the walls towards the outer boundary. When selecting the bias factor, a smooth growth must be ensured such that the free-stream flow approaching the cylinders is not disturbed by the mesh and therefore does not experience a sharp change. The same applies to the downstream of the cylinder to enable accurate prediction of the wake data. Finally, a very fine mesh is applied adjacent to the cylinder wall to ensure the boundary layer is accurately captured. The size of the grids then gradually increases from the wall to build a courser mesh further from the wall.

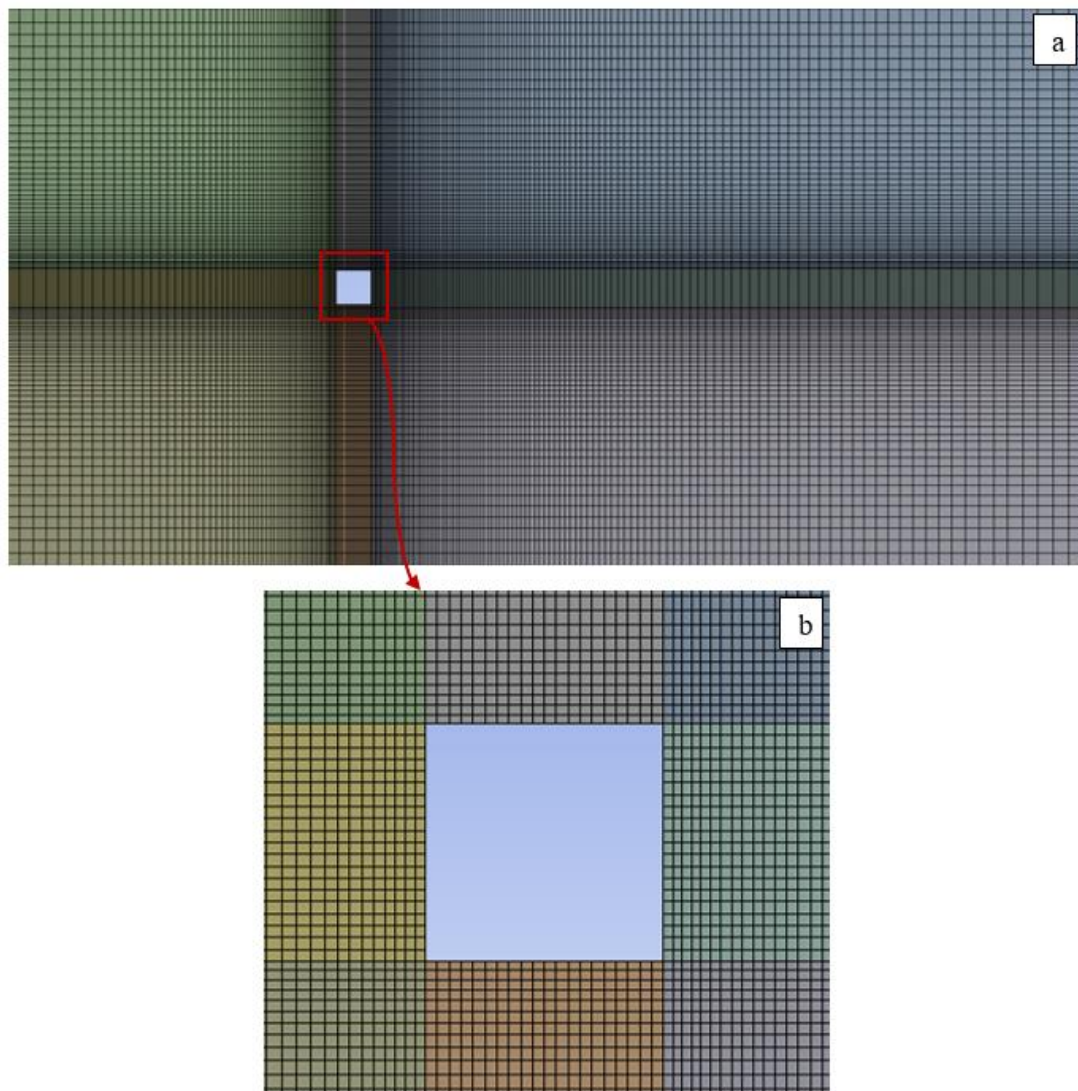


Figure 5.4 Side view of the structured mesh generated for the bare square cylinder; a) whole domain, b) enlarged view showing the finer mesh around the cylinder.

The growth of the grid can be observed in Figures 5.4 (a) and 5.5 (a), where the generated meshes for the computational domain containing the solid square cylinder and the leading-half porous cylinder are shown. As can be seen in the figures, a finer mesh is applied around the cylinders, of which the enlarged views are shown in Figures 5.4 (b) and 5.5 (b). In the span-wise direction, the sizing function without any growth factor has been used to uniformly distribute the grid cells with an interval of $0.13 H$. For the porous

cases, the mesh lines in the porous region should be aligned with the mesh lines outside the porous medium, so that the grids at the interface of the porous material and the surrounding domain match each other. The connection of the grid cells can be clearly seen in Figure 5.5 (b) for the leading-half porous cylinder.

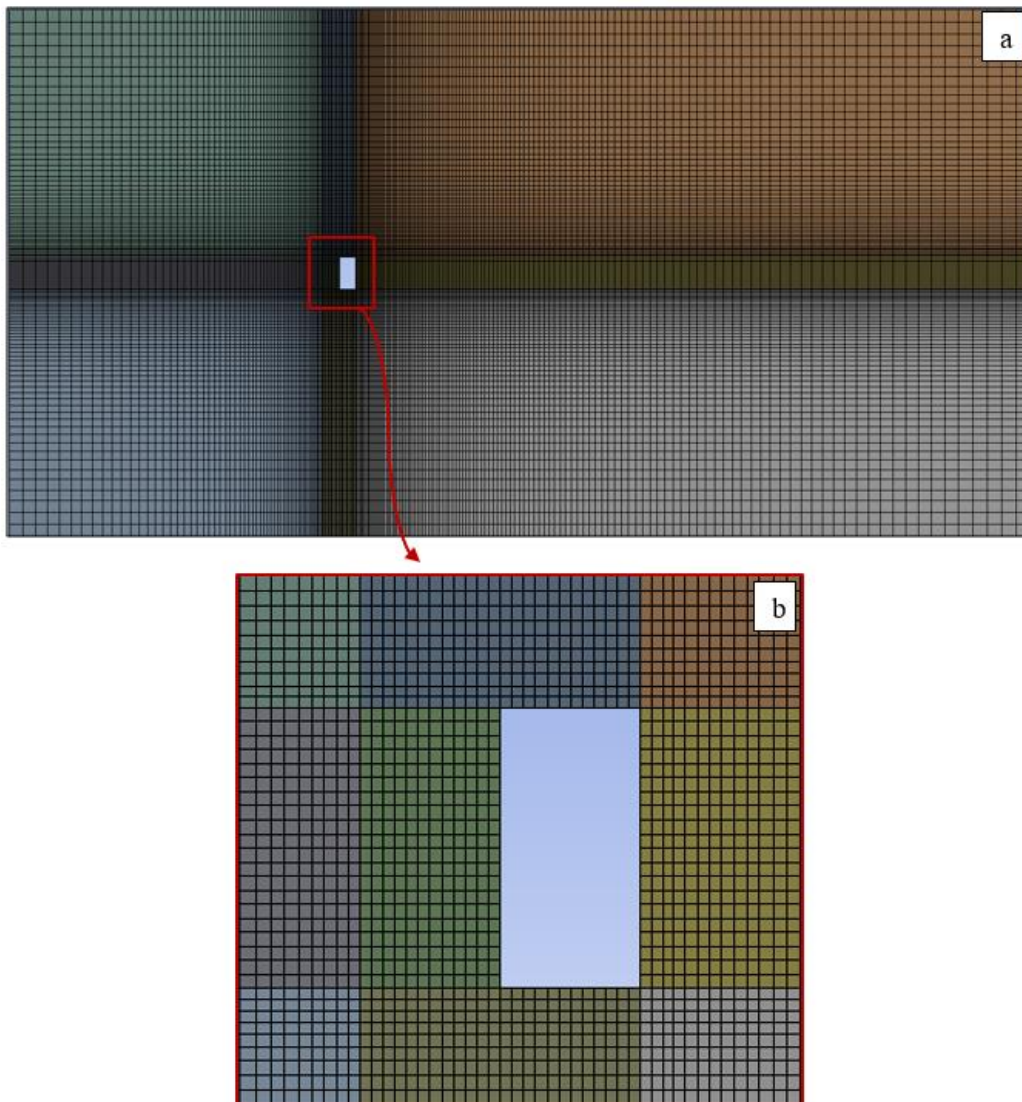


Figure 5.5 Side view of the structured mesh generated for the square cylinder with porous material at its leading half: a) whole domain, b) enlarged view showing the finer mesh around the cylinder.

The mesh quality analysis have been done to ensure that the grids are of a sufficient quality not to affect the final solution. This is possible within the ANSYS meshing that quantifies properties of the mesh such as skewness and aspect ratio in the mesh metrics section. The skewness is a measure of the distortion of a selected element compared to its ideal shape (ANSYS 2015), which is hexahedron in the present work. The value of skewness is between zero and one, zero being the excellent quality indicating an equilateral cell and one the poorest quality indicating a completely degenerate cell. Checking the skewness ensured a complete equilateral shape for this mesh study with a zero standard deviation. In addition, aspect ratio defined as the ratio of the longest side of a grid to its shortest side in a quadrilateral mesh (ANSYS 2015) was checked. The aspect ratio of a perfect square is one, which means both sides are equal. The smoothness in the change in aspect ratio for the present simulations has been ensured by checking the locations where the highest aspect ratios occurred. The maximum value of aspect ratio for the present mesh validation study found to be 15 for the bare cylinder and 12 for the porous-treated cylinders.

5.6 Computational Setup

An element-based finite volume method is used in ANSYS CFX in which the spatial domain is first discretised by the use of mesh. Then, finite volumes are constructed using the mesh that conserve the quantities of mass, momentum and energy. For the code to solve the problem, a CFD analysis containing all the details of the problem under study must be set up. The set up includes the introduction of analysis type, parameters related to the domain and the objects inside the domain, initial and boundary conditions, time step in transient solution, solver and output controls, etc. The fluid is set up to be air at 25 degrees Celsius and atmospheric pressure. The porous domain in the porous cases is

defined by introducing the permeability and resistance loss coefficient obtained from the experiments described in Chapter 4. The 20 PPI porous material is used for the simulations with a measured permeability equal to $4.64 \times 10^{-7} \text{ m}^2$ and a resistance loss coefficient equal to 1658 m^{-1} .

The next step is to define the solution schemes for the solver including the advection scheme and transient scheme for unsteady simulations. As a second order scheme is recommended for most transient simulations for the approximation of the time derivatives (ANSYS 2015), a high resolution advection scheme with a second-order backward Euler transient scheme have been chosen in the current simulations. In transient simulations, a time step has to be defined. The choice of time step size is another key parameter for the accuracy of the results. Although there is not a fixed formulation to determine the time step, a time step as the initial estimate must be determined to start the simulation. There are some guidelines available for the numerical codes for the estimation of the initial time step. For example, when using high resolution advection scheme, a time step of approximately 1/4 to 1/3 of the physical time step is recommended (ANSYS 2015). The physical time step is a fraction of a length scale divided by a velocity scale. In external flows, a reasonable approximation of time step is:

$$\Delta t \approx \frac{L_c}{U_0}. \quad (5.14)$$

In equation 5.18, Δt is the physical time step, L_c is a characteristic geometric length and U_0 is the free stream velocity. In the present simulations, the size of square side (H) was considered as the characteristic length, which gives a physical time step of 0.002. Therefore, a time step of 0.0006 has been applied as the first estimate for all the cases considered in this work.

Another method to make an initial estimate of the time step is by the frequency of vortex shedding. If the frequency in a certain fluid flow problem is known, the highest frequency should be resolved with at least 10-20 time steps per period (Menter *et al.* 2002). The frequency can be estimated by the Strouhal number that is defined as:

$$f = \frac{StU_0}{L_c}, \quad (5.15)$$

where, St is the Strouhal number and f is the frequency of the vortex shedding. The Strouhal number for a bare square cylinder is approximately 0.13 in a flow that has a Reynolds number of order between 10^3 to 10^5 , based on the available data in literature, such as Minguez *et al.* (2011), Lyn *et al.* (1995) and Vickery (1966). The Strouhal number of 0.13 gives a frequency of 65 for the current work and hence a size of around 0.0007s could be used as the first estimation of the time step for the bare cylinder, which is close to the size estimated based on the physical time step.

To assess the influence of the time step size on the results of the current simulation, a systematic reduction of the time step has been used and the simulation repeated to assess the results. After several attempts, a time step of 0.0001s resulted in a good agreement between the simulation results and the available data in literature for the solid case. Therefore, this time step was selected for all the case studies for the time duration on which the results are averaged.

5.6.1 Boundary Conditions

The partial differential equations obtained from conservation laws are identical for a particular type of flow irrespective of the flow domain. The boundary conditions act as

the constraints and establish the uniqueness of the flow field for a specified problem. There exist two types of boundary conditions in numerical simulations: physical boundary conditions, which are imposed by the physical processes at the bounding surfaces of the flow domain and artificial boundary conditions, which are specified at the boundaries of computational domain (Wilcox 2006). In simulations of flow over a cylinder, the solid surface of the cylinder represent the natural physical boundary. Flow is unbounded, so that the flow domain is infinite. However, numerical simulation requires a finite computational domain, hence artificial boundary conditions are applied, and appropriate values of flow parameters are specified based on physical reasoning.

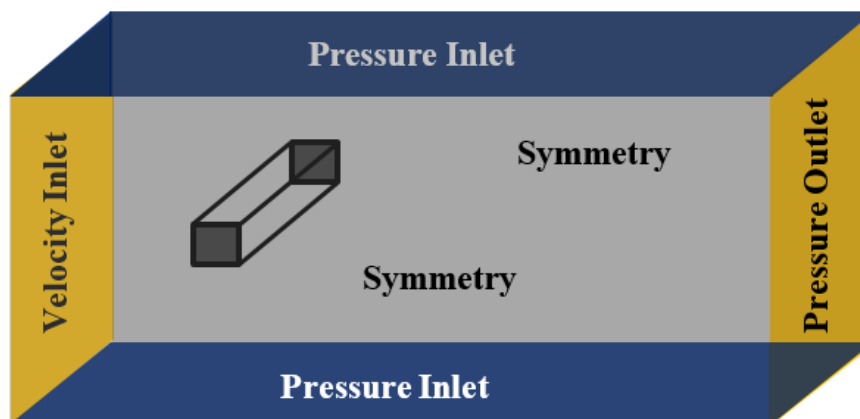


Figure 5.6 The conditions used on the boundaries of the domain encasing all the cases studied.

Boundary conditions on physical boundaries are straightforward. For viscous flow, relative velocity at the solid surface is zero, which is called no-slip boundary condition. Therefore, the boundary condition at the cylinder surface set as no-slip boundary condition. Conditions on the fluid boundaries can take variety of forms in ANSYS CFX setup interface including inlet, outlet, symmetry and opening. Details of the inlet and

outlet boundary conditions can be set as either velocity, specified pressure or mass flow rate. For the numerical model to represent the physical problem, proper boundary conditions for the fluid boundaries need to be defined. Although simple configurations are studied in the present work, it has to represent the conditions of an experimental model. The boundary conditions are set to ensure the same conditions present in the wind tunnel tests carried out in this study and presented in Chapter 3. The boundary conditions on the fluid domain are depicted in Figure 5.6.

The upstream boundary where the fluid begins to flow towards the cylinders is the inlet boundary at which the mean flow velocity is uniform. The inlet boundary is designated as a velocity inlet. The inlet velocity has a value of 20 m/s in the stream-wise direction ($U_0 = 20$ m/s) and is zero in other directions. This velocity corresponds with the Reynolds number of around 5.3×10^4 based on the following formulation:

$$Re = \frac{\rho U_0 H}{\mu}, \quad (5.16)$$

where, ρ and μ are the fluid density and dynamic viscosity, respectively. This condition has chosen to be equivalent to the experimental inlet condition of the present work. The downstream end of the fluid domain where the fluid exits the domain is the outlet boundary. A pressure outlet condition was assigned for the outlet boundary with a zero relative pressure. Symmetry boundary condition was used as the boundary conditions for the span-wise ends. In the symmetry boundary condition, the normal velocity at the boundary and the flux of all quantities across the boundary are assumed zero. It can be interpreted as a slip wall in viscous flows (ANSYS 2015). The symmetry condition enforces a parallel flow and is frequently used in CFD codes at the span-wise end

boundary conditions when the approaching flow direction is parallel to them (Vaz *et al.* 2007). For the upper and lower boundaries, pressure inlet boundary conditions were imposed. This boundary condition was selected because the pressure gradient in the stream-wise direction is negligible and hence a constant pressure is required in those boundaries. The relative pressure was set as zero, to ensure that the flow pressure on the upper and lower boundaries remains equal to the outlet pressure. In addition, zero gradient boundary condition has been selected as the condition for turbulence and flow direction, because it prescribes the gradient of the field on the boundary to zero.

5.7 Solution Convergence and Mesh Independency Analysis

Fluid flow problems are nonlinear in nature and the governing Navier-Stokes equations can only be solved analytically by imposing restrictive conditions. Therefore, the solutions have to be calculated in an iterative manner. In the first iteration, the flow parameters are calculated based on an initial estimate. The calculations continue in each of the iterations until the error in the solved equations is smaller than a predetermined value. The termination criterion is usually based on the residuals of the corresponding equations. This is the first criterion in the convergence of a CFD code solution to a problem. It must be ensured that the rms error values of the solution residuals have reached a value below 10^{-4} . In addition to the residuals, convergence of a solution is evaluated by monitoring the behaviour of target variables such as lift, drag, pressure drop, etc. The solution is converged when the variables reach a constant value or oscillate around a constant value, so that further iterations have a negligible effect on the monitored points. Finally, the integral balances of mass, momentum and energy must be examined to ensure that the domain has solution imbalances of less than 1%. Smaller residual termination point can be used if the target variables and integral imbalances do not reach

the desired values. The above procedure results in a converged solution for a particular mesh that have been used. The next step is to confirm that the solution is not influenced by the mesh resolution.

Regardless of the type of mesh, it is essential that the mesh is sufficiently fine not to compromise the solution. Hence, a mesh refinement is essential. Mesh refinement is to ensure the solution is independent of the selected mesh. The mesh independency study consists of constructing a mesh in the domain that is being simulated and monitoring a parameter of interest. Once the solution becomes stable and the values of monitored points are in a reasonable range, more refinement is being done to evaluate any changes in the results. The global mesh is continuously refined until the change in the monitoring points is within the acceptable discretization error on a particular simulation and more refinement has a negligible effect on the solution.

The computational grid for all the bare and porous cases in the current study is structured and hexahedron in shape. For the grid independency study, the grid size that initially used for the bare square cylinder was 4.70×10^5 elements, with which reasonable results obtained. Mean drag coefficient and rms value of lift coefficient and the pressure coefficient at the base point, the centre point at the leeward edge of the cylinder (shown in Figure 6.11), are examined. The pressure coefficient was calculated from the following equation,

$$C_p = \frac{P - P_0}{2\rho U_0^2}, \quad (5.17)$$

where, C_p is the pressure coefficient, P is the pressure at the point at which pressure coefficient is being evaluated, P_0 is the pressure in the freestream, U_0 is the free stream velocity.

As a common practice, the global mesh increased by about 1.5 times and the values of monitor points recorded and the process repeated one more time to compare the values from the three meshes. The difference in the monitored points from the second mesh with 6.58×10^5 elements from the first mesh is 1.89%, 9.13% and 1.46% for $C_{d, \text{mean}}$, $C_{l, \text{rms}}$ and $C_{p,b}$, respectively. These values reduces to 0.18%, 1.55% and 0.36% when the mesh is increased to 9.60×10^5 . As no significant effect can be seen when the mesh increased to the third mesh, the second mesh was selected to reduce the computational time. The statistics for all the meshes are presented in Table 5.1.

Table 5.1 Mean values of drag and base pressure coefficients and the rms value of the lift coefficient for the flow around solid square cylinder.

Total number of elements	$C_{d, \text{mean}}$	$C_{l, \text{rms}}$	$C_{p,b}$
4.70×10^5	2.167	1.238	-1.365
6.58×10^5	2.208	1.351	-1.385
9.60×10^5	2.212	1.372	-1.390

The grid independency study for the porous cases started with the total grid elements of 5.93×10^5 . As the porous edges in this simulation are introduced as interfaces and not walls, the values of drag and lift coefficients cannot be directly obtained in the solution process. Therefore, another variable had to be chosen for monitoring. The stream-wise velocity on the centreline at $x/H=0.5$ was selected as the monitoring point.

The same process as the solid case repeated for both the trailing-half and leading-half porous cases, which is presented in Tables 5.2 and 5.3. Comparing the results, increasing the mesh from 7.12×10^5 elements to 9.69×10^5 elements resulted in a negligible difference in the monitored values for both cases. Any further refinement is not likely to affect the values and therefore the solution can be considered sufficiently independent from the mesh.

Table 5.2 Base pressure coefficient and mean stream-wise velocity at $x/H=0.5$ on the centreline for the flow around leading-half porous square cylinder.

Total number of elements	$C_{p,b}$	u_c at $x/H=0.5$
5.93×10^5	-1.341	0.108
7.12×10^5	-1.448	0.038
9.69×10^5	-1.452	0.011

Table 5.3 Base pressure coefficient and mean stream-wise velocity at $x/H=0.5$ on the centreline for the flow around trailing-half porous square cylinder.

Total number of elements	$C_{p,b}$	u_c at $x/H=0.5$
5.93×10^5	-1.152	-0.284
7.12×10^5	-1.225	-0.212
9.69×10^5	-1.230	-0.181

5.8 Model Verification through Comparison with Experimental Data

Steady RANS performs an averaging in time that leads to a statistically steady description of the turbulent flow. Although the flows investigated are unsteady in nature,

the results of a steady RANS simulation can be compared to the wind tunnel's results as the flow conditions of a wind tunnel is time-averaged (Franke *et al.* 2011). Therefore, in this study, the numerical model is validated through comparison between the SST steady results and the experimental results presented in Chapter 5. More verification of the model is presented in Chapter 6 by comparing the unsteady RANS results with available data in the literature.

Figure 5.7 shows a comparison between the stream-wise velocities obtained from steady SST modelling and time-averaged wind-tunnel experiments at three axial locations ($x/H = 0.5, 1.5, 2.5$) downstream a bare square cylinder. It is observed that in the near wake of the bare cylinder, the SST model predicts the velocity profile close to the profile obtained from the wind tunnel. However, in the far wake, although showing similar parabola-like profile, the velocity values around the centreline predicted by SST model are less than that from the experiments. These values far from the centreline are predicted to be higher than experimental results. It should be noted that the profiles obtained from experiments are not symmetric around the centreline and are slightly shifted upwards, while the numerical results are symmetric. This is the reason why the profiles do not coincide with each other for example at $x/H = 0.5$. The cross-stream velocity profiles from both the RANS modelling and experiments are shown in Figure 5.8. Good agreement is seen between the experimental and numerical results. In the far wake, the numerical model slightly under predicts the velocity values.

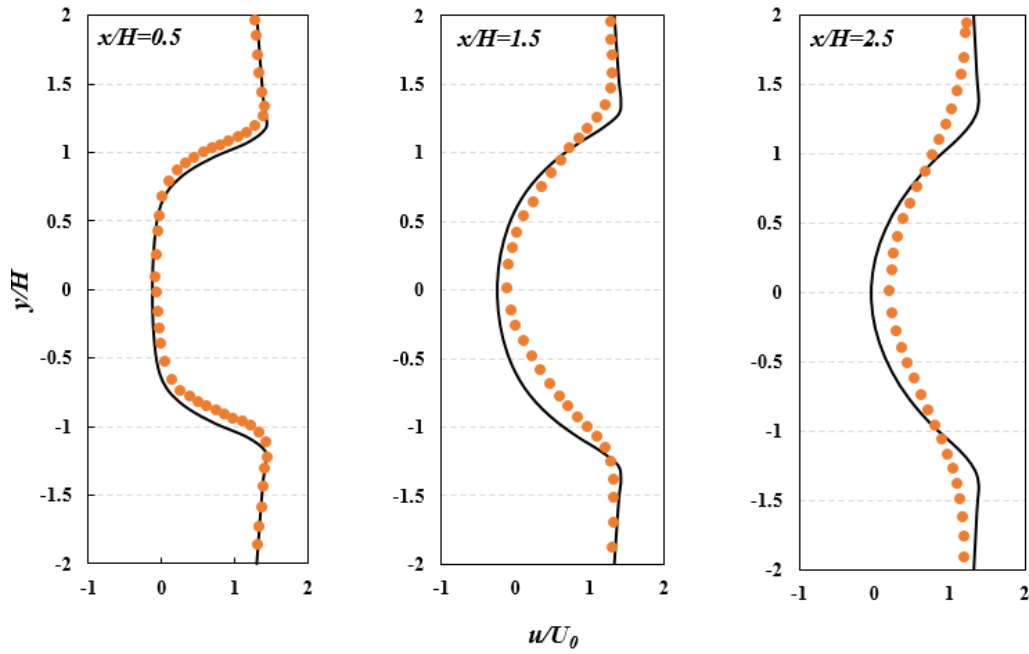


Figure 5.7 Stream-wise velocities at different axial locations in the wake region for the bare square cylinders; Black solid line: steady RANS, Orange dotted line: time-averaged experimental results.

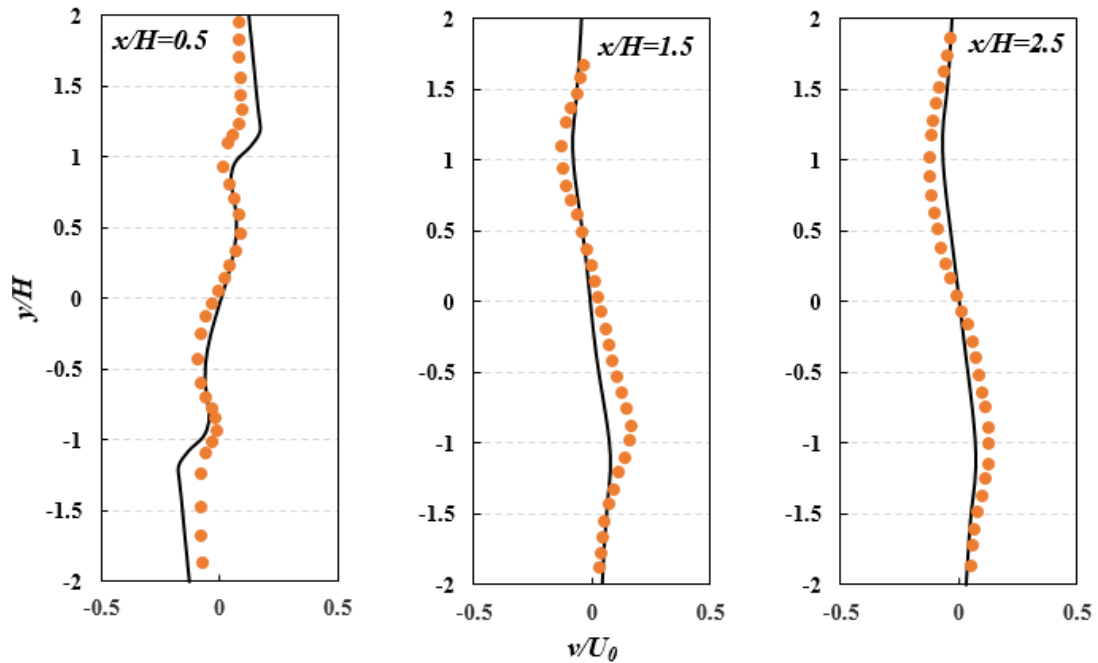


Figure 5.8 Cross-stream velocities at different axial locations in the wake region for the bare square cylinders; Black solid line: steady RANS, Orange dotted line: time-averaged experimental results.

The stream-wise and cross-stream velocity profiles for a cylinder treated with porous material at its trailing half are presented in Figures 5.9 and 5.10 in which the results of the SST model and PIV experiments at $x/H = 0.5, 1.5, 2.5$ are compared. At $x/H = 0.5$ and 1.5 , the SST model is successful in accurately predicting the stream-wise velocity. The slight difference in the profile at $x/H = 0.5$ along the centreline is due to the symmetry in the velocity curves from the simulation, while the profile from experiments is not symmetric. At $x/H = 2.5$, a small deviation from the experimental profile is observed for the stream-wise velocity. In addition, the prediction of the cross-stream velocity by the SST model is accurate at $x/H = 0.5$. However, at $x/H = 1.5, 2.5$, the SST model under predicts the cross-stream profiles downstream the trailing-half porous cylinder. Generally, good agreement can be observed between the two results. However, the numerical model provides more accurate profiles in the near wake downstream the porous-treated cylinders.

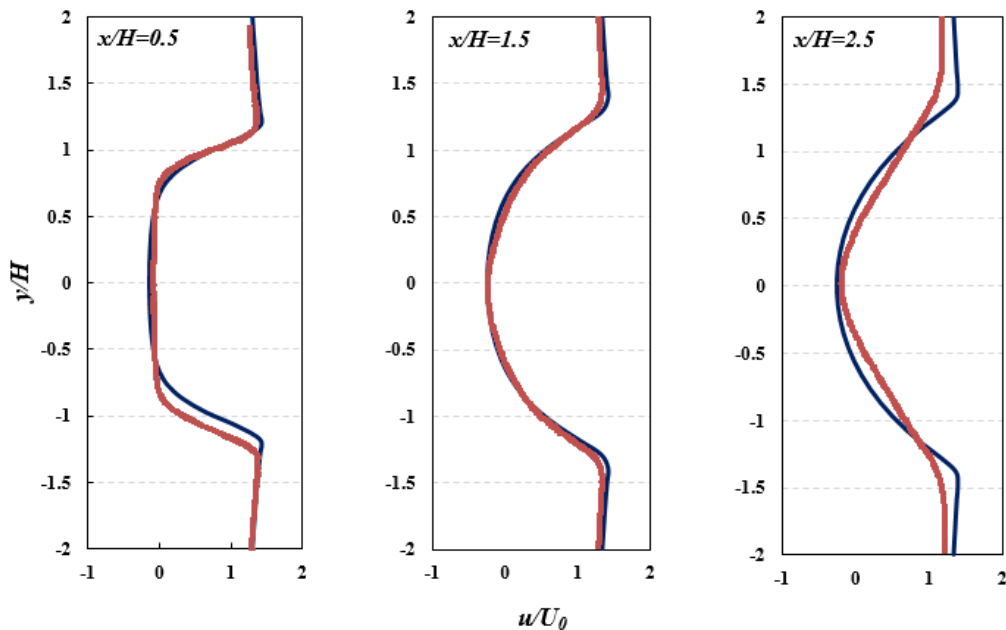


Figure 5.9 Stream-wise velocities at different axial locations in the wake region for the trailing-half porous square cylinders; Dark blue line: steady RANS, Red line: time-averaged experimental results.

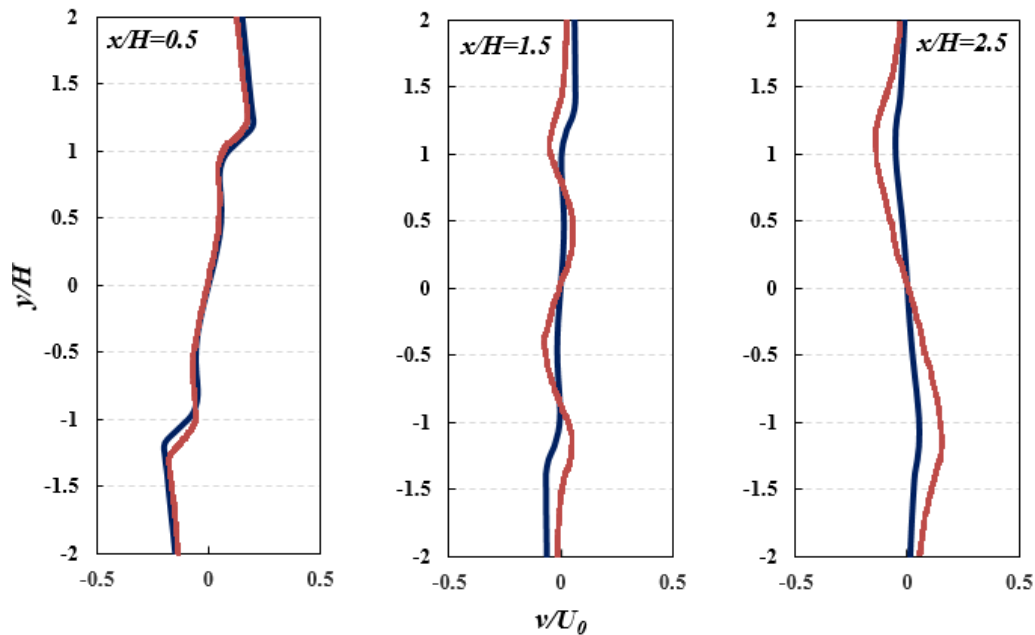


Figure 5.10 Cross-stream velocities at different axial locations in the wake region for the trailing-half porous square cylinders; Dark blue line: steady RANS, Red line: time-averaged experimental results.

5.9 Conclusions

A numerical procedure has been developed to conduct three-dimensional simulations of square cylinders with and without porous material as a passive flow control method. The simulations have been performed in the CFD code, ANSYS CFX by the use of RANS modelling. Among the RANS models, the SST model was selected due to its ability to better predict the boundary layer profile and pressure gradients. The methodology and considerations in developing numerical models have been discussed in detail. Moreover, the computational domain, process of grid generation and numerical set up have been described. The effect of grid resolution was tested for all the cases under study and a grid that provides the highest accuracy, while maintaining the lowest cost has been selected for each case.

The steady RANS simulations with SST turbulence model have been evaluated against the experimental data obtained from PIV technique. The comparison revealed that the SST model shows good agreement when applied in the steady state analysis of square cylinder's wake region. The agreement between the two results indicates the validity of the numerical model used. Having gained confidence in the numerical model, transient simulations have been performed to further study the unsteady flow over the square cylinders, which are presented in the next chapter.

CHAPTER 6

NUMERICAL RESULTS AND DISCUSSION

6.1 Introduction

Preceding chapter has presented the configurations for the treatment of square cylinders with porous materials for the simulation studies. Two porous dispositions have been considered for the square cylinder. One of them composed of solid material at the upstream half and porous material at the downstream half of the cylinder as what studied in experiments, called trailing-half porous hereinafter. The second, was modified so that its upstream half consisted of porous material, referred to as leading-half porous in the subsequent parts of this research. This is equivalent to rotating the first porous model by 180 degrees. Porous medium of permeability equal to 4.64×10^{-7} has been selected for the simulations as the most permeable material used in the experiments with the highest effect on the flow field. The numerical method developed during the course of this research to model the solid and porous-treated square cylinders has been presented and discussed in the previous chapter.

Due to the time-varying nature of the real flows, particularly at high Reynolds numbers, the analysis of the flow over time provides a better understanding of the phenomena. This chapter presents the simulation work and numerical analysis studies

undertaken in the transient condition using unsteady RANS (URANS). The total time of each simulation was one second, of which the results for the last 0.8 seconds was used for the calculation of the mean values. This corresponds to 50 cycles of vortex shedding. The flow parameters for the porous-treated cylinders are compared with each other and with the solid bare cylinder both qualitatively and quantitatively.

6.2 Validation of the URANS Results with Available Data

In the preceding chapter, the simulation results of this research in steady state condition were compared and validated with the experimental results of this work obtained from a series of PIV experiments. In this section, the transient results of the numerical simulation are quantitatively validated against the available data in the literature. Because no previous data is available on the flow over the porous-treated cylinders studied in this work, comparison is performed only for the solid bare cylinder. Velocity profiles in the wake of the bare cylinder is presented. The velocity profiles at the shear layer region of the cylinder is also presented to compare the boundary layer behaviour.

The results obtained for the transient flow over the solid square cylinder is compared with the experimental and numerical work of other scholars. In Figure 6.1, the normalised time-averaged stream-wise velocity at the centreline downstream solid square cylinders are shown. In the figure, the results of the present work is compared with the experimental results of Durão *et al.* (1988) at a Reynolds number of 14000 and the numerical results of Trias *et al.* (2015) at a Reynolds number of 22000. The results of Trias *et al.* (2015) has been obtained using DNS simulation, which is known as being the most accurate turbulence model at present (Bai *et al.* 2016). As seen, closer to the cylinder, up to $x/H \approx 1$, velocity profile of the present work is in a very good agreement

with the results obtained by DNS model. However, further downstream from the cylinder, although slightly over predicted, a better agreement is observed with the experimental result. The deviation in the results is inevitable considering that the studies have been performed in different Reynolds numbers.

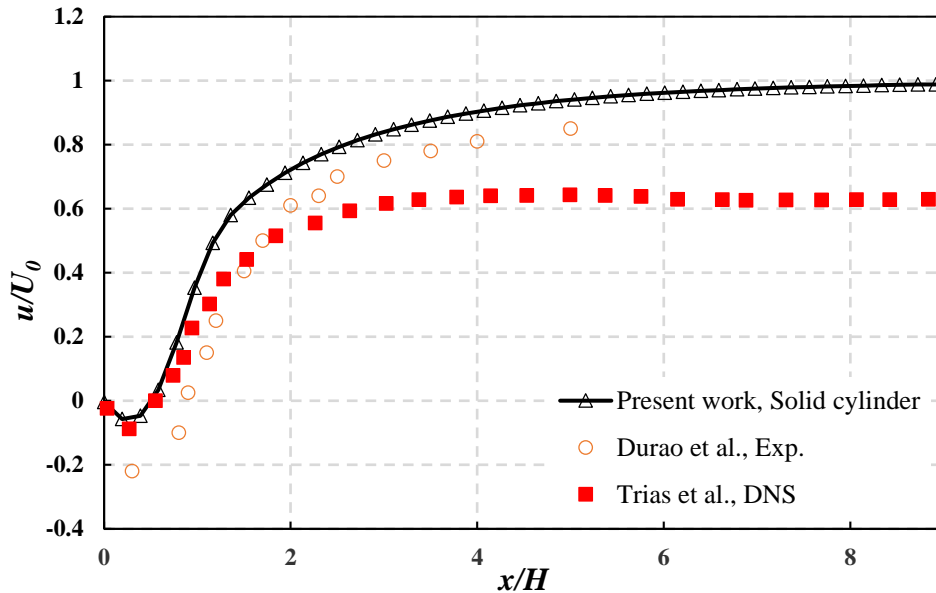


Figure 6.1 Profiles of the time-averaged stream-wise velocity at the centreline downstream the solid square cylinder. Comparison is made between the experimental results of Durão *et al.* (1988) and averaged numerical velocity profile of Trias *et al.* (2015).

The normalised time-averaged stream-wise velocity profiles on and above the upper wall of the square cylinder at two axial locations ($x/H = -0.625, -0.375$) are shown in Figures 6.2 and 6.3. The results are compared with the LES work of Mínguez *et al.* (2011) and DNS work of Trias *et al.* (2015). The axial locations considered for this comparison correspond to $x/H = \pm 0.125$ in their work. The reversed flow near the wall around the upstream corner of the square cylinder $x/H = -0.625$, is predicted to be less intense than that predicted by Mínguez *et al.* (2011). However, far from the wall good agreement can be seen between the two results. At $x/H = -0.375$, The reversed flow near the wall is less intense than that from both the numerical results. Overall, the stream-

wise velocity profile is closer to the DNS result of Trias *et al.* (2015) within the boundary layer and closer to the LES result of Minguez *et al.* (2011) beyond the boundary layer.

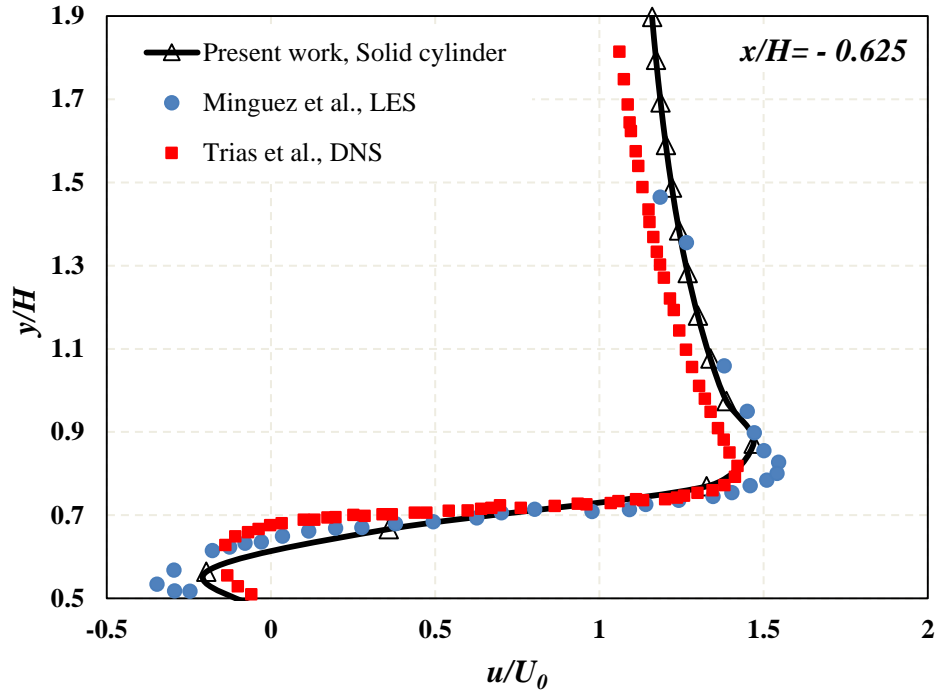


Figure 6.2 Profiles of the time-averaged stream-wise velocity at $x/H=-0.625$. Comparison is made between the numerical results of (2011) and Trias *et al.* (2015).

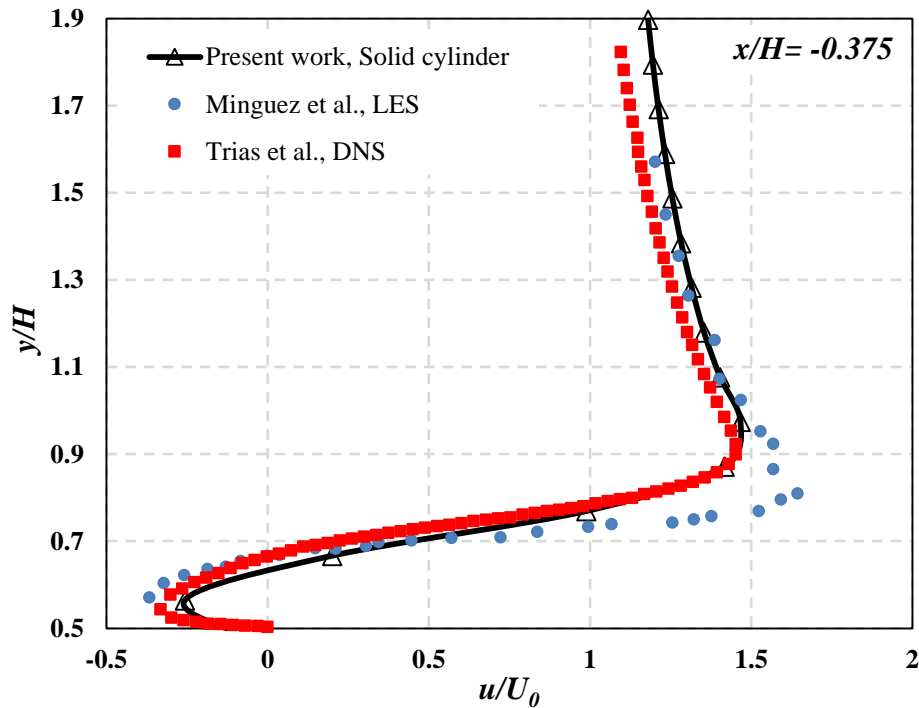


Figure 6.3 Profiles of the time-averaged stream-wise velocity at $x/H=0.625$. Comparison is made between the numerical results of Minguez *et al.* (2011) and Trias *et al.* (2015).

6.3 Velocity Streamlines

The time-averaged velocity streamlines generated by the solid square cylinder and square cylinders with their trailing and leading halves comprised of porous materials are shown in Figure 6.4. As expected, the incoming laminar flow separates at the top and bottom corners of the leading edges of both the bare and the trailing-half porous cylinders. The separation of the flow for leading-half porous cylinder occurs at the corners of the interface of solid and porous parts. The flow then subjects to transition to turbulence in the shear layers separated from the cylinders walls, resulting in the formation of the well-known von Karman vortex street in the wake of the cylinders. The motion of the flow is quantitatively presented in Figures 6.7 to 6.10 by the distribution of the velocity profiles in the shear layer region and in the wakes of all the cylinders.

As previously demonstrated in the experimental results, a delay in the formation of vortices is seen for the cylinder with porous treatment at its downstream half. Therefore, a larger recirculation length ($x/H \approx 1$) is observed for the trailing-half porous cylinder compared to the bare cylinder ($x/H \approx 0.6$). However, the formation of large vortices downstream the cylinder is not significantly affected when the cylinder is treated with porous material at its leading half. Accordingly, the recirculation length in the leading-half porous cylinder is only slightly larger than that in the solid case.

A closer look at the streamlines (Figure 6.4 (a)) reveals that for the solid bare cylinder, recirculation regions form after the separation, spreading along the upper and lower surfaces of the cylinder. In addition, two smaller recirculation regions is observed at the downstream corners of the cylinder, consistent with what Cao and Tamura (2016) found in their LES simulation using structured grids. Finally, two large vortices of the opposite signs are identified downstream the cylinder.

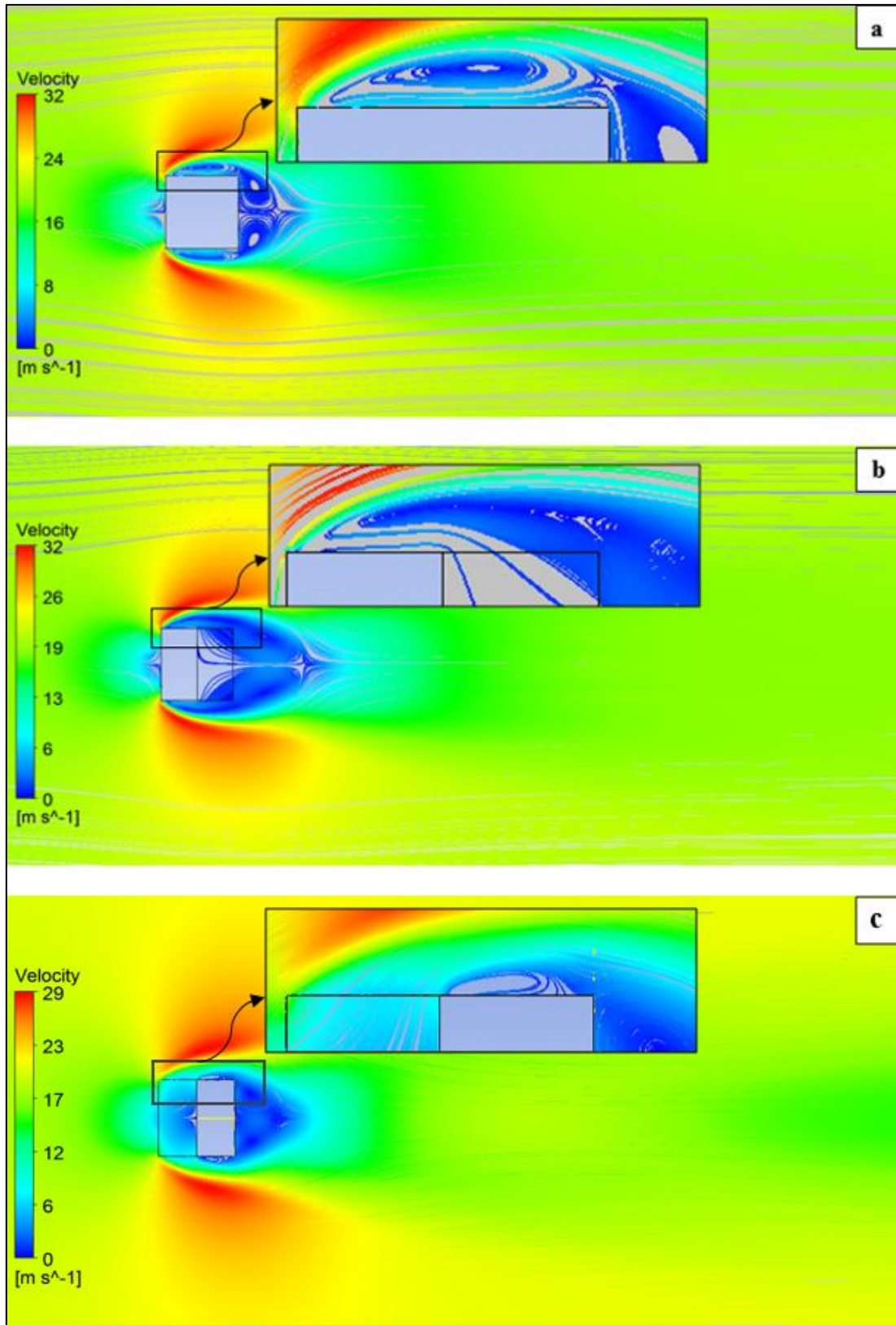


Figure 6.4 Time-averaged velocity streamline generated by square cylinders; (a) bare cylinder, (b) cylinder treated with 20 PPI porous layer at the trailing half, (c) cylinder treated with 20 PPI porous layer at the leading half.

Different to the solid cylinder, no recirculation occurs either on the upper and lower surfaces or around the downstream corner of the trailing-half porous cylinder magnified in Figure 6.4 (b). Here, the flow penetrates the porous material and two large recirculation bubbles form starting from the upstream corners extending to the downstream of the cylinder. This observation is perhaps different from what really happens inside the porous material, as the flow structure within the pores of the porous material is not captured by the present simulation.

The flow in the case of the leading-half porous cylinder (Figure 6.4 (c)) behaves similar to the solid bare cylinder. Recirculation occur on the upper and lower surfaces of the solid part after the flow separates from the upstream corners of the solid material. However, no secondary recirculation is observed on the surfaces, which can be due to the short length of the solid surface. Eventually, a pair of counter-rotating vortices is identified downstream the cylinder.

6.4 Vorticity Contours

Figure 6.5 shows the contours of instantaneous vorticity magnitude for the solid square cylinder and square cylinders with porous materials at their leading and trailing halves. The three contour plots show differences in terms of flow structures. The development of the Karman vortex street for all the cases are clearly seen in the figure. The length of the shear layer separating from the trailing-half porous cylinder is greater than that separating from the solid cylinder. The greater shear layer length indicates slower development of the eddy content in the wake following boundary layer detachment. This is because the flow around the trailing-half porous cylinder remains closer to the surface of the cylinder. Consequently, the temporal disturbances in the shear layer occurs at a further distance downstream the cylinder. Therefore, the pressure

gradient around the cylinder is lower, (Also shown in Figure 6.11), which results in less drag and lift forces. For the leading-half porous cylinder, the wake length is nearly the same as the solid cylinder. However, the vorticity contour is almost symmetric in close proximity of the cylinder, implying less instability.

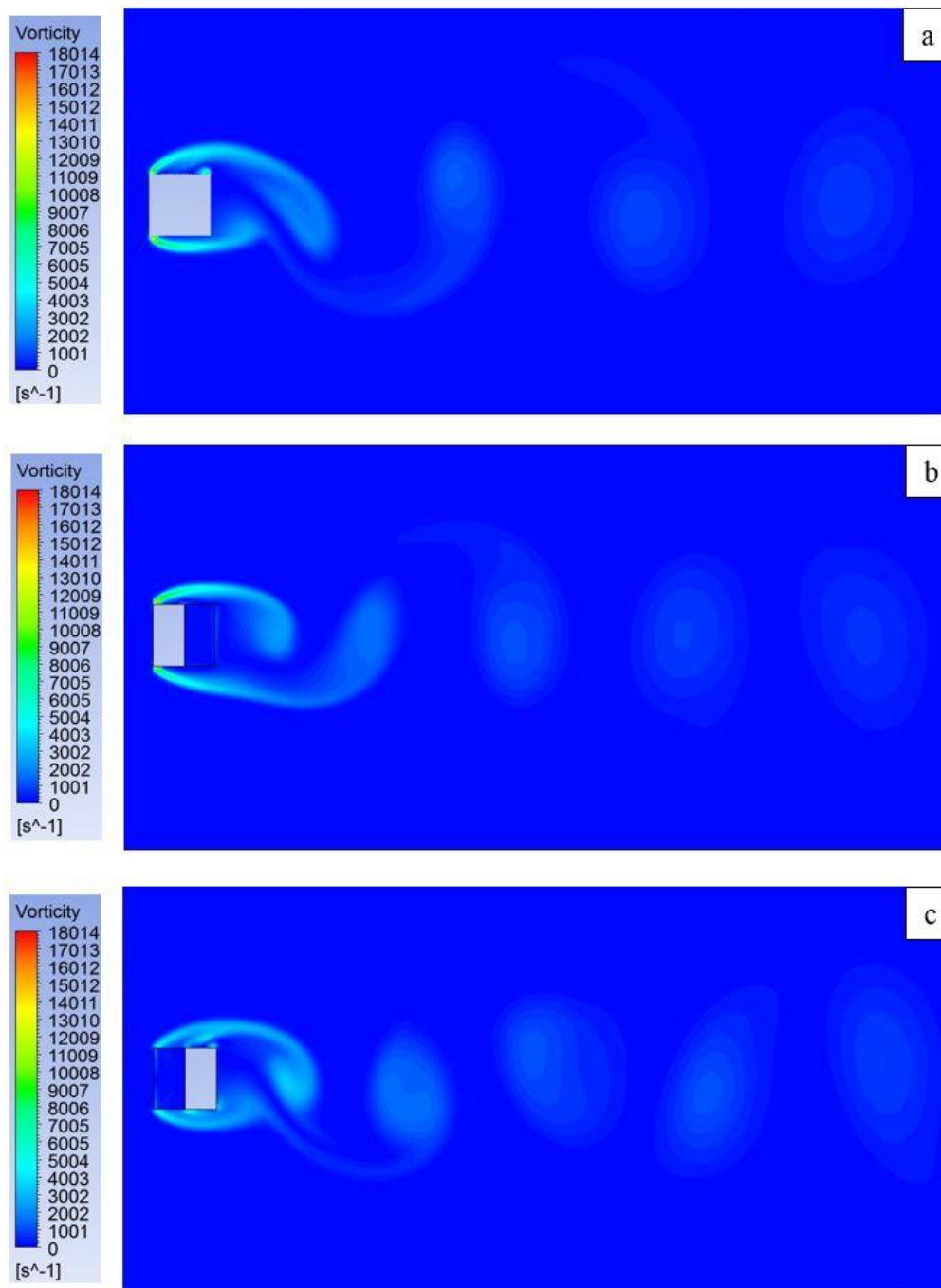


Figure 6.5 Contours of instantaneous vorticity magnitude in the wake of the square cylinders; (a) bare cylinder, (b) cylinder treated with 20 PPI porous layer at the trailing half, (c) cylinder treated with 20 PPI porous layer at the leading half.

6.5 Velocity Components

Velocity profiles in the stream-wise and cross-wise directions for the bare and porous-treated cylinders are presented and compared with each other. The velocity profiles are presented in the wake of the cylinders as well as the near wall region to study the structures developing when the fluid flows over the different cylinders. The coordinate system and axial locations at the near wall region and in the wake are given in Figure 6.6, consistent with the coordinate system considered in the experiments (Figure 3.4).

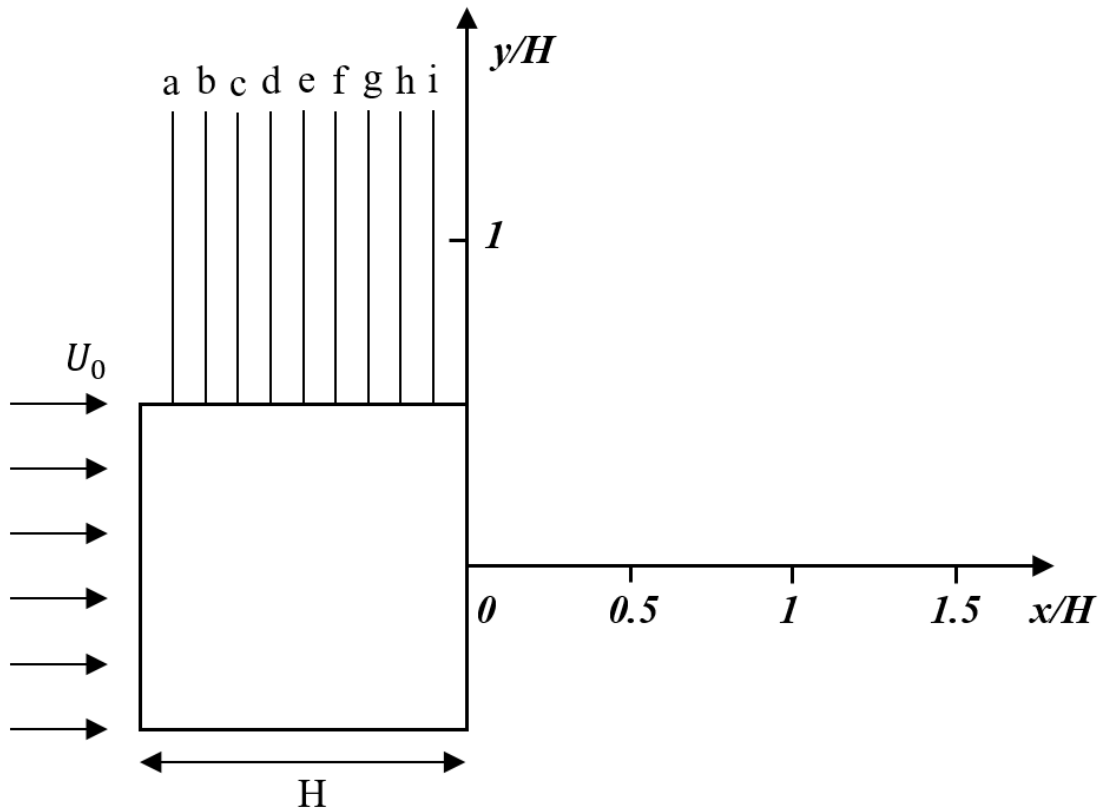


Figure 6.6 Axial locations around the cylinder used in Figures 6.7 to 6.9; a: $x/H = -0.9$, b: $x/H = -0.8$, c: $x/H = -0.7$, d: $x/H = -0.6$, e: $x/H = -0.5$, f: $x/H = -0.4$, g: $x/H = -0.3$, h: $x/H = -0.2$, i: $x/H = -0.1$.

6.5.1 Velocity Components in the Shear Layer Region

The stream-wise development of the flow around the cylinders can be explored in detail by studying the velocity profiles at the close proximity of the cylinder walls. Such study gives insights about the formation of boundary layer and the development of the shear layer in each case. For this purpose, the time-averaged stream-wise velocity profiles from leading edge ($x/H = -0.9$) to trailing edge ($x/H = -0.1$) along the vertical direction on the upper surface of all the cylinders are plotted in Figure 6.7.

The change in the sign of the stream-wise velocity for the solid cylinder starts from ($x/H = -0.6$) and extends to the end of the wall. This negative velocity region confirms the existence of the smaller recirculation bubbles at the downstream corner, illustrated in Figure 6.4. The maximum stream-wise velocity for the solid cylinder is around $1.5 U_0$ above the shear layer, which is the same as what Minguez *et al.* (2011) obtained from their LES simulation. The minimum value inside the shear layer region varies from $-0.16 U_0$ and $-0.26 U_0$. This variation is from $-0.15 U_0$ to $-0.4 U_0$ in the work of Minguez *et al.* (2011).

A reversed flow can be detected for the trailing-half porous cylinder starting from ($x/H = -0.8$) to the end of the upper wall, indicating the existence of recirculation bubbles. The boundary layer for the trailing-half porous cylinder grows faster than the other two cylinders. This faster growth can be observed in the peak of the velocity shifted away from the wall. Among all the cylinders, the trailing-half porous cylinder has the biggest stream-wise velocity of around $1.6 U_0$ which occurs at ($x/H = -0.4$). The minimum value within the shear layer region varies from $-0.07 U_0$ and $-0.19 U_0$.

The leading-half porous cylinder shows positive stream-wise velocity values in the porous part decreasing towards the downstream end of the cylinder wall. A small negative

velocity region can be identified (more evident in the cross-stream velocity profile in Figure 6.8) at the downstream half of the cylinder indicating the small recirculation at the top wall. The maximum stream-wise velocity for the leading-half porous cylinder is around $1.4 U_0$ above the shear layer. The minimum value inside the shear layer region varies from $+0.4 U_0$ and $-0.05 U_0$.

Figure 6.8 compares the time-averaged cross-stream velocity profiles in the near wall region for the solid cylinder and cylinders with porous materials at their leading and trailing halves. The peak of the profile for the cross-wise velocity component correspond to the edge of the shear layer between the wall and the freestream flow. At $x/H = -0.9$ and $x/H = -0.8$ (around the upstream edge), the leading-half porous cylinder shows a narrower shear layer compared to the other two cases. Further downstream the cylinders, the shear layer width is almost the same for the all cases.

For the solid case, starting from the upstream edge ($x/H = -0.9$), the cross-wise velocity profile shows a sharp decrease in its value, which continues over the length of the wall up to $x/H = -0.6$, after which experiences a slight reduction. The cross-stream velocity for the solid cylinder has a maximum value of around $0.9 U_0$ at the edge of the shear layer and a minimum value of $-0.13 U_0$ within the recirculation region. These values are respectively $1.0 U_0$ and $-0.25 U_0$ in the LES work of Minguéz *et al.* (2011).

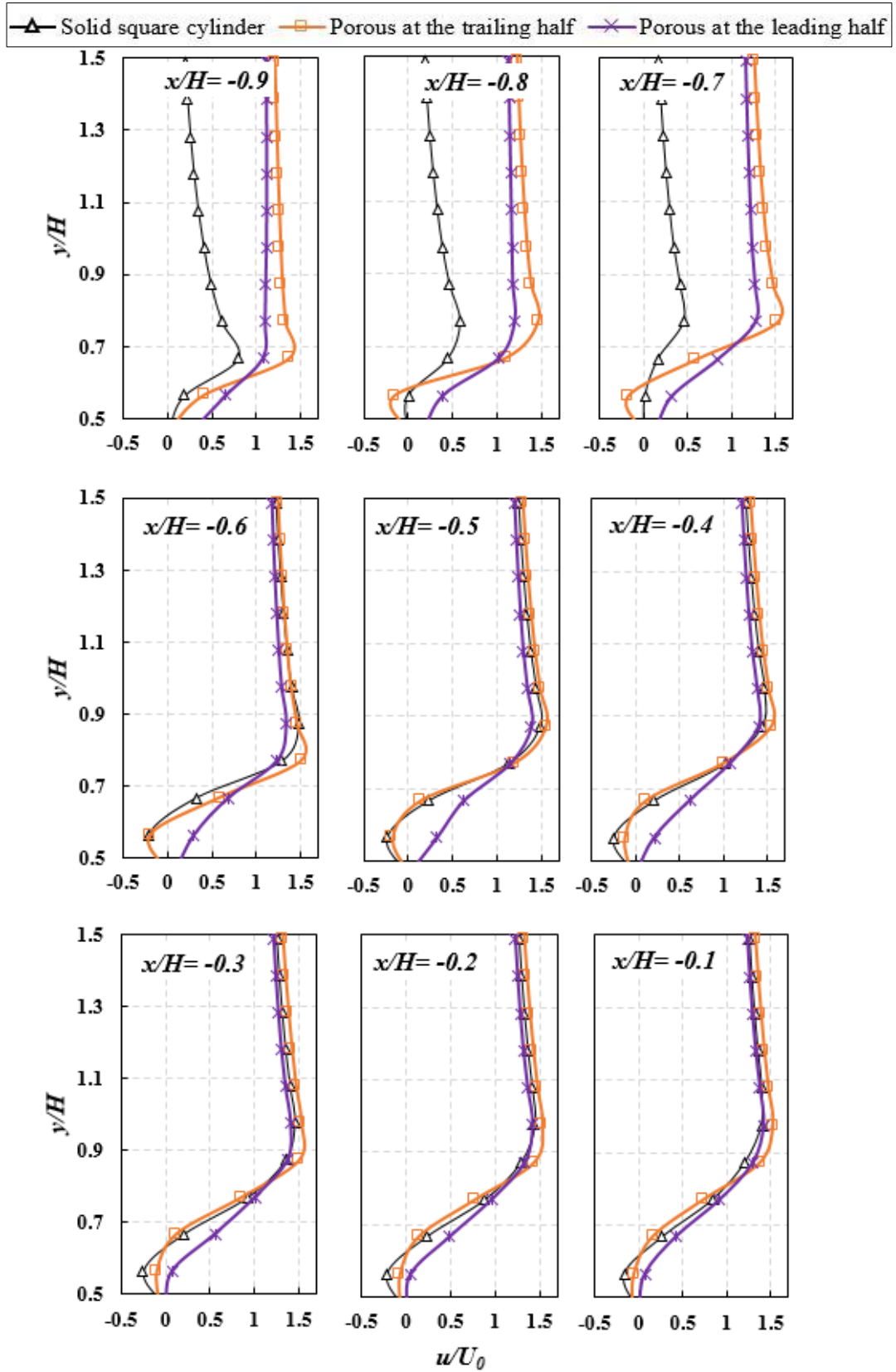


Figure 6.7 Time-averaged stream-wise velocities at different axial locations in the shear layer region for the bare and porous-treated square cylinders.

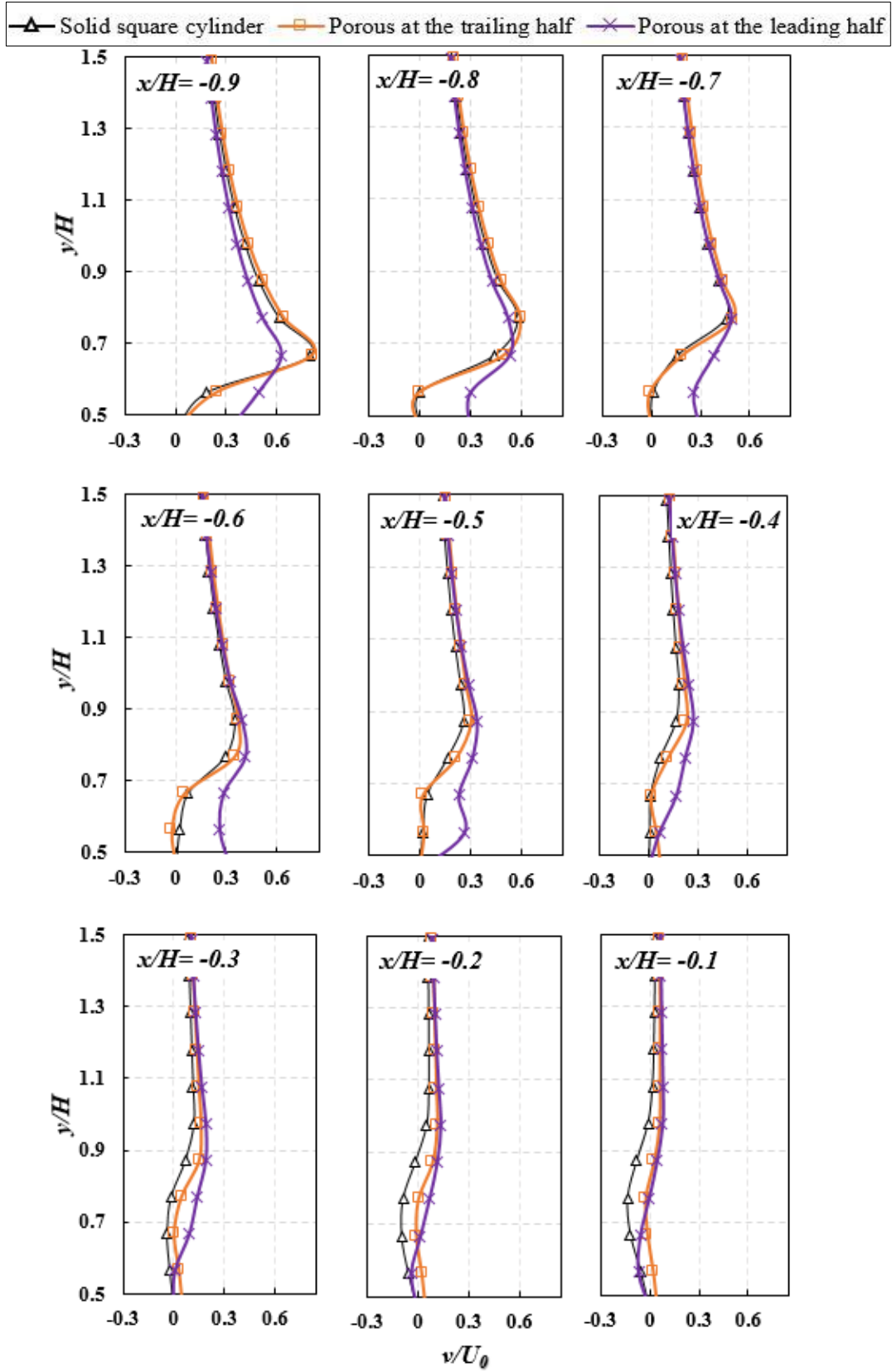


Figure 6.8 Time-averaged cross-stream velocities at different axial locations in the shear layer region for the bare and porous-treated square cylinders.

The velocity profile for the trailing-half porous cylinder is almost the same as the solid cylinder in the upstream half of the cylinder ($x/H = -0.9$ to -0.6), where the wall is solid. After this point, where the porous material replaces the solid material (i.e., $x/H = -0.5$) the profile, although keeping a similar trend as the solid one, shows lower values in the whole region. The smaller values are specifically evident closer to the wall in the shear layer region. The maximum cross-stream velocity is approximately $0.9 U_0$ at the edge of the shear layer and the minimum is $-0.1 U_0$ inside the shear layer region.

The leading-half porous cylinder, however, shows a different behaviour in the shear layer region over the length of the upper wall. Here, unlike the other two cases, the cross-stream velocity has a positive value at the upstream location. This is because of the fluid flowing out of the porous material. Then it gradually loses its value over the length of the wall where the cylinder is comprised of porous material and reaches to zero when the cylinder becomes solid. The profile retains its shape over the solid part from $x/H = -0.4$ to the downstream end of the cylinder, $x/H = -0.1$. The cross-stream velocity has a maximum value of $0.62 U_0$ at the edge of the shear layer and a minimum value of $-0.07 U_0$ within the shear layer zone.

6.5.2 Velocity Components in the Wake

The profiles of stream-wise velocity at selected locations (i.e. $x/H = 0.25, 0.5, 1, 2, 3$ and 4) are shown in Figure 6.9. The solid cylinder and leading-half porous cylinder show similar stream-wise velocity profile in the near wake region up to $x/H = 1$, although at $x/H = 0.5$, the leading-half porous cylinder shows smaller values near the wake centreline. Starting from $x/H = 1$, after the the recirculation region, the solid cylinder shows a fast recovery in its stream-wise velocity until it reaches a relatively

constant profile after $x/H = 3$. However, the leading-half porous cylinder slowly recovers its velocity from $x/H = 1$ and shows negligible changes in the profile from $x/H = 2$ to $x/H = 4$. This agrees with the plot of the velocity at the centreline as depicted in Figure 6.10, noticing that the velocity gains its value after $x/H = 4$ and reaches to its maximum value of 0.8 relative to the freestream velocity.

For the trailing-half porous cylinder, as expected based on the experiments, a larger negative velocity region indicating reversed flow is observed in the near wake up to $x/H = 0.5$, which suggests a longer recirculation length. From $x/H = 1$, the velocity begins to recover its value and reaches that of the leading-half porous cylinder at $x/H = 2$ near the centreline. Further downstream the trailing-half porous cylinder, from $x/H = 3$, the velocity profile becomes closer to that of the solid case near the centreline and similar to that of the leading-half porous cylinder further away from the centreline.

To assess the wake behaviour of different case studies, their mean centreline stream-wise velocity component is compared in Figure 6.10. The recirculation region is marked by a blue rectangle in the figure. The bare and leading-half porous cylinders show almost the same recirculation region, while the trailing-half porous cylinder shows a bigger recirculation region, compliant with the streamlines in Figure 6.4 and the experimental results given in Figure 4.8. It is also evident in the figure that the velocity is not zero right at the back of the trailing-half porous cylinder, which shows that the fluid flows through the porous material at the downstream half of the cylinder.

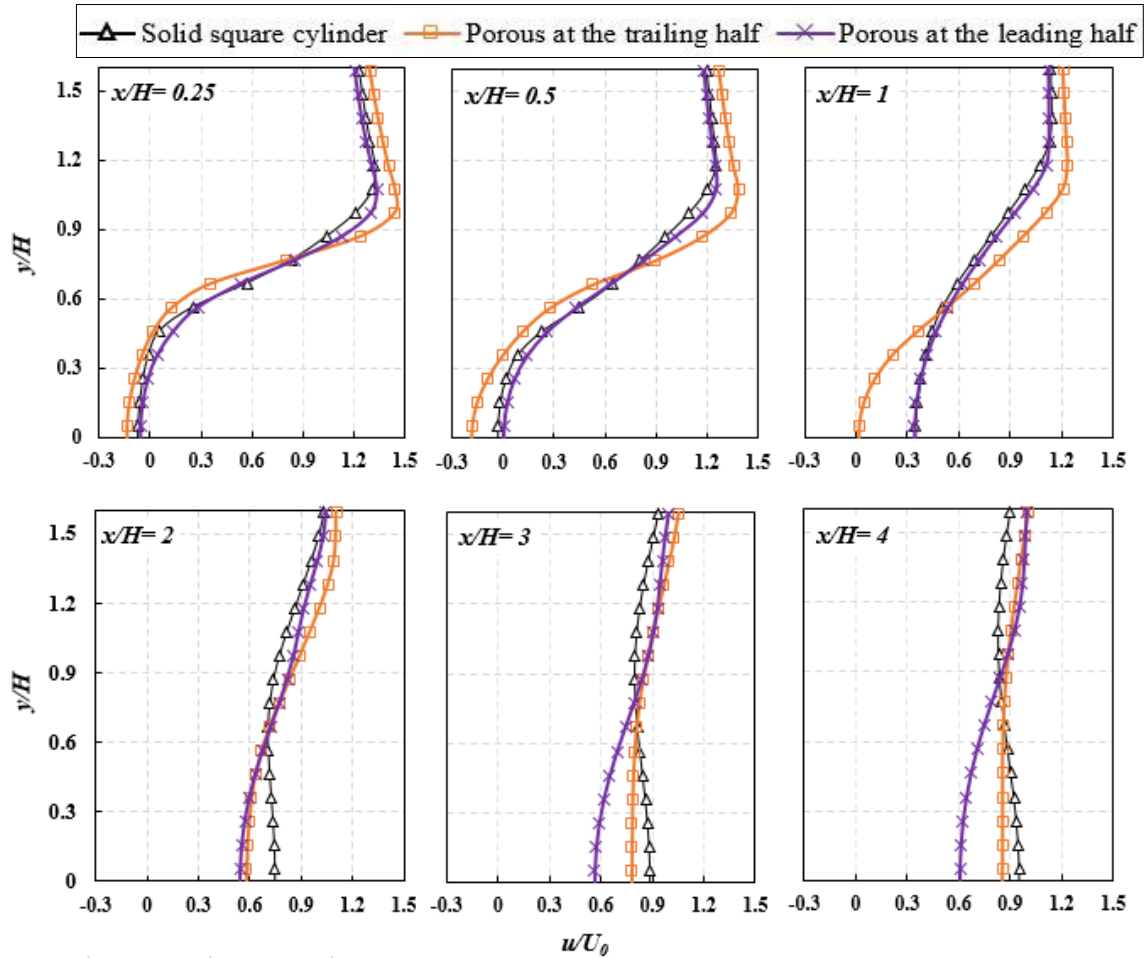


Figure 6.9 Time-averaged stream-wise velocities at different axial locations in the wake of the bare and porous-treated square cylinders.

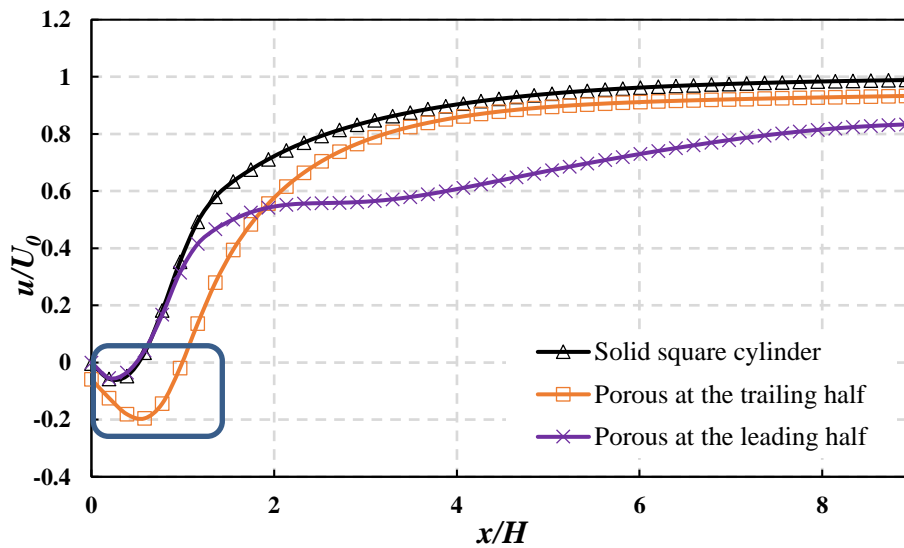


Figure 6.10 Normalised time-averaged stream-wise velocity at the centreline downstream the square cylinders. Comparison is made between the bare square cylinder and the square cylinders with porous materials at their leading and trailing halves.

6.6 Pressure

Figure 6.11 displays the time-averaged pressure field for the bare and porous-treated cylinders. Pressure difference at the leading and trailing edges of the cylinders can be qualitatively seen in the figure. The pressure gradient causes the pressure drag, which is the main source of the drag force on a square cylinder, because the tangential shear stresses, which cause friction drag, are small.

When the upstream uniform flow reaches the square bare cylinder, the flow strike with the upstream wall of the cylinder causes a region with high-pressure values. Then the flow separates from the cylinder surface due to the sharp upstream corners and causes two large recirculation areas at the top and bottom of the cylinder (shown in Figure 6.4). The separation of the flow leads to a sharp drop in the pressure and hence an adverse pressure gradient. The flow experiences negligible changes in its pressure over the top and bottom recirculation areas until it reaches the downstream corner of the cylinder, where a small increase in the flow pressure occurs. Finally, two vortices of the opposite signs form downstream the cylinder causing a decrease in pressure.

The flow experiences the same pressure variations when passing over the trailing-half porous cylinder. However, because the flow penetrates the porous material at the downstream half, the pressure drop is lower compared to the bare cylinder. The minimum value of the pressure coefficient on the centreline in the wake region is -1.7 at $x/H \approx 0.6$ and -1.5 at $x/H \approx 0.88$ for the bare and trailing-half porous cylinders respectively. This can be observed in Figure 6.12 where time-averaged pressure coefficients on the centreline are shown for all the cases. The pressure coefficients were calculated using Equation 5.17.

In the case of the leading-half porous cylinder, the increase in pressure when impinging the upstream porous edge is much lower than that in the case of the bare and trailing-half porous cylinders. This is because the flow can pass through the pores, and therefore the velocity does not fall to zero on the upstream edge. The pressure reduces within the porous material and hence a lower pressure drop occurs when the flow separates from the upstream solid corners. The pressure reduces further downstream the cylinder until it reaches the lowest value of $Cp = -1.8$ at $x/H \approx 0.97$ in the wake region (Figure 6.12). The values of pressure coefficient at the front point and base point, marked respectively by f and b in Figure 6.11, are calculated. The front and base points are the centre points on the centreline at the front and leeward sides of the cylinders, respectively. The above pressure coefficients together with the minimum value of pressure coefficient on the centreline in the wake of cylinders, calculated using Equation 5.17, are presented in Table 6.1 for all the studied cylinders and compared to the result of Minguéz *et al.* (2011).

Table 6.1 Mean values of pressure coefficient for the solid bare square cylinder and square cylinders with porous materials at their trailing and leading halves. From left to right: pressure coefficient at the front point, pressure coefficient at the base point, minimum pressure coefficient in the wake. Results of Minguéz *et al.* (2011) for a solid bare cylinder is included as a comparison to the present work.

Cylinder	Cp_f	Cp_b	$Cp_{min,wake}$
Solid, (Minguéz <i>et al.</i> 2011), LES	–	-1.3	–
Solid, Present work, RANS	1.30	-1.39	-1.7
Porous at the trailing half	1.30	-1.23	-1.5
Porous at the leading half	1.14	-1.45	-1.8

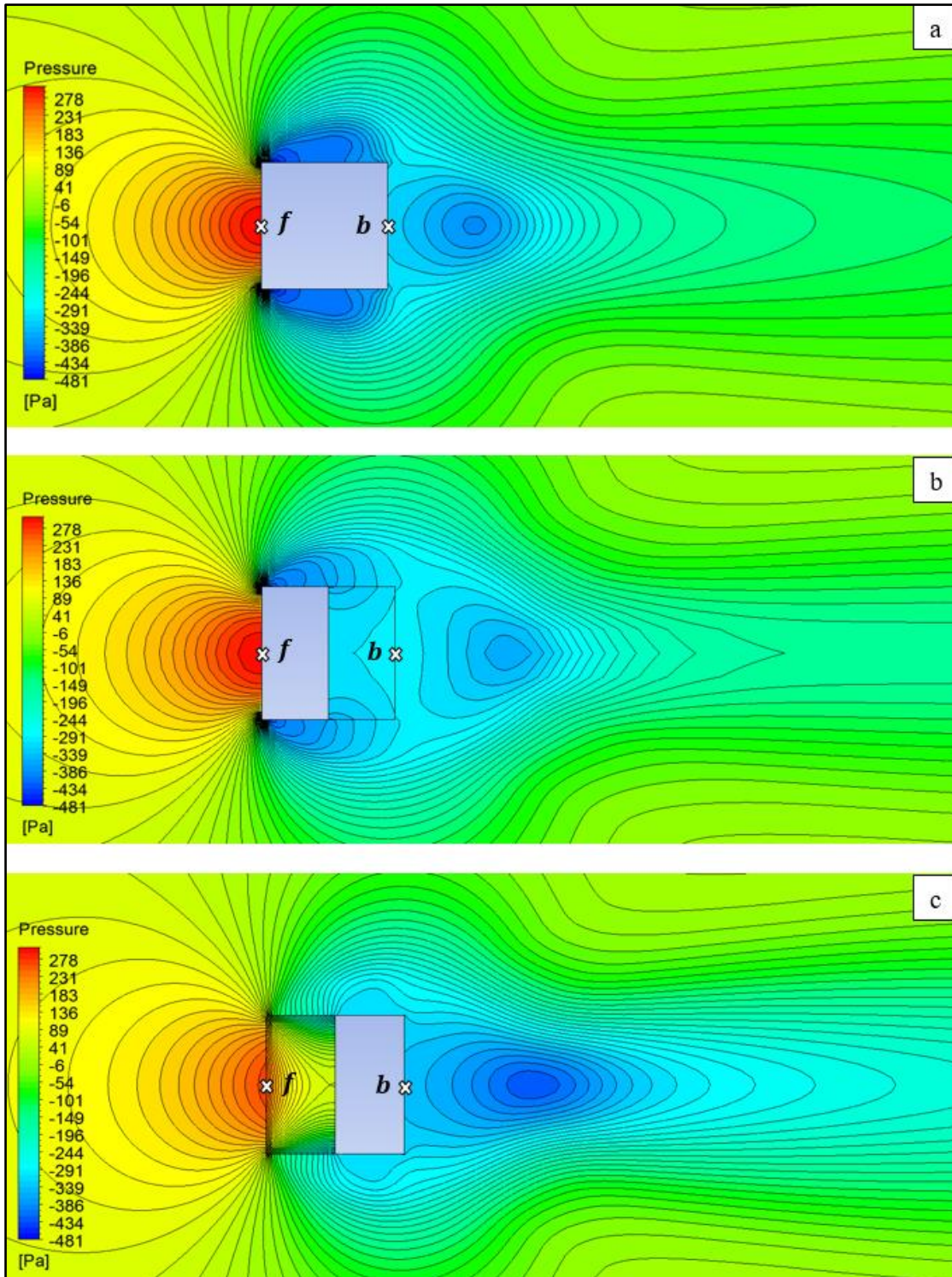


Figure 6.11 Time-averaged pressure at the mid-plane downstream the square cylinders. (a) bare cylinder, (b) cylinder treated with 20 PPI porous layer at the trailing half, (c) cylinder treated with 20 PPI porous layer at the leading half.

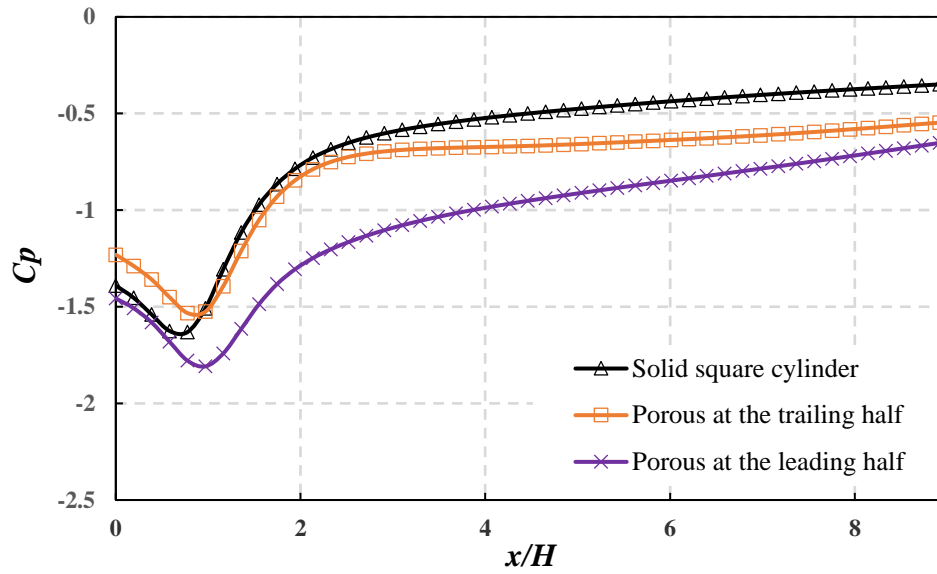


Figure 6.12 Time-averaged pressure coefficient at the centreline downstream the square cylinders. Comparison is made between the solid square cylinder and the square cylinders with porous materials at their leading and trailing halves.

6.7 Aerodynamic Forces

The primary motivation of applying the porous sheaths to the bluff bodies in this research was to investigate the effect on the aerodynamic forces. To obtain the drag and lift coefficients for the solid cylinder, the following equations have been defined in CFX-Pre.

$$C_D = \frac{2F_D}{\rho AU_0^2}, \quad (6.1)$$

$$C_L = \frac{2F_L}{\rho AU_0^2}, \quad (6.2)$$

where, C_D is the drag coefficient, C_L is the lift coefficient, F_D is the drag force, F_L is the lift force, A is the area of the cylinder surface normal to the incoming flow ($A = L \times H$) and U_0 is the free stream velocity.

The time history of the fluctuations of the drag and lift coefficient for the solid bare cylinder obtained from the numerical simulation are given in Figure 6.13. The mean drag coefficient is 2.21 and the RMS lift coefficient is 1.37. These values correspond well with those of Minguez *et al.* (2011) and Lübcke *et al.* (2001) obtained from LES simulations (Presented in Table 6.2).

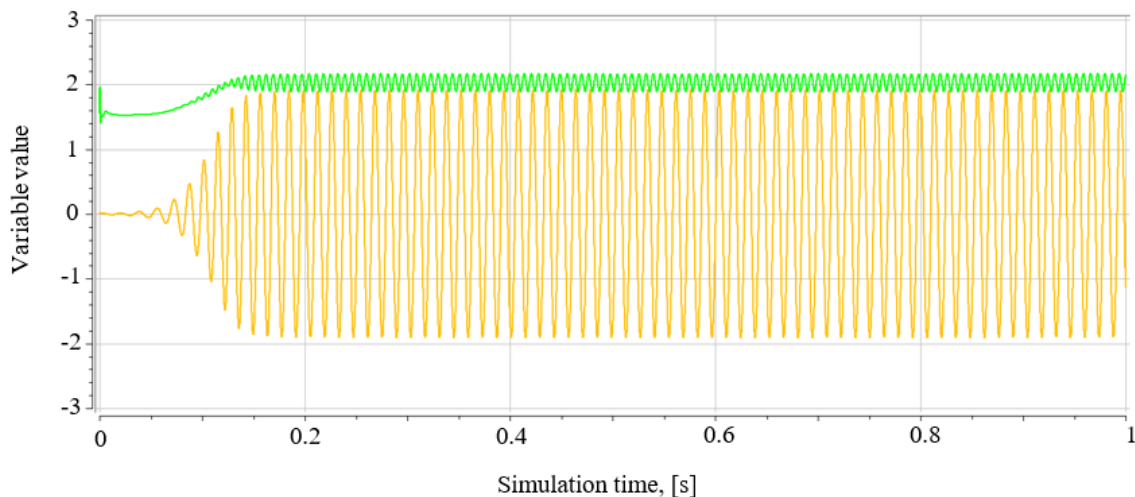


Figure 6.13 Drag and lift coefficients generated by the solid square cylinder; green line: Drag coefficient, yellow line: Lift coefficient.

The drag coefficient for porous-treated cylinders is indirectly determined by using the integral momentum equation. The drag coefficient for solid bare cylinder calculated from Eq. 4.2 is equal to 1.45 which under predicts the real drag coefficient. This is because the integral momentum method gives an approximation of the drag force based on the mean quantities, and the errors in the calculation of mean values and the curve fitting of the

velocity profile and integration yield a smaller drag value compared with the accepted value. However, the errors are the same for all of the calculations and therefore, the difference between the drag force of a solid and porous cylinder is reliable. The drag coefficient calculated for all the case studies are tabulated in Table 6.2 together with the percentage of the change in drag coefficient compared to the bare cylinder. It is found that the drag coefficient of the square cylinder with its trailing half comprised of porous material is 13% lower than that for the bare cylinder, whereas this decrease is 9% in case of the square cylinder with porous material at its leading half. A tentative conclusion of this analysis is that the application of porous media to bluff bodies does reduce the drag coefficient, but this clearly requires further detailed mathematical analysis, and ideally confirmation by experiment

Table 6.2 The time-averaged drag coefficient and rms value of fluctuations in the lift coefficient for the flow around solid bare square cylinder and square cylinders with porous materials at their trailing and leading halves. Results of (Minguez *et al.* 2011) for a solid bare cylinder is included as a comparison to the present work.

Cylinder, Author	Method	C_D	$C_{L,rms}$	Rate of change in C_a compared to bare cylinder
Solid, (Minguez <i>et al.</i> 2011)	LES	2.2	–	–
Solid, (Lübcke <i>et al.</i> 2001)	LES	2.178	1.47	–
Solid, Present	RANS	2.21	1.37	–
Solid, Present	Momentum	1.45	–	0
Porous at the trailing half, Present	Momentum equation	1.25	–	13%
Porous at the leading half, Present	Momentum equation	1.31	–	9%

6.8 Conclusions

In this chapter, the flow around two hybrid solid-porous cylinders has been investigated and compared with the flow around a solid bare cylinder. It has been demonstrated that the flow field around square cylinders can be effectively controlled by the use of porous sheets at the leading and trailing halves of the cylinders. The recirculation bubbles are shifted away from the cylinder by replacing a part of the cylinder with porous material. This shift is more apparent when the porous material replaces the downstream half of the cylinder.

A significant change in the wake velocity is obtained when the cylinder is modified with porous material. The most remarkable difference is in the recirculation region for the trailing-half porous cylinder, where the magnitude of the stream-wise velocity at the centreline is above twice lower than that in the leading-half porous and solid cylinders. However, the difference between the velocity magnitude of the trailing-half porous cylinder and solid cylinder decreases as x/H increases. The leading half porous cylinder behaves the opposite by showing similar velocity profile in the near wake and a significantly reduced velocity magnitude further downstream. It is also found that fluid flow through the porous part of the cylinder causes a deviation in the velocity components in the vicinity of the wall in the shear layer region. A larger growth in boundary layer is observed when the porous sheet replaces the trailing half of the cylinder.

In addition, the use of porous material significantly changes the pressure distribution around the cylinder. A higher pressure difference between the front and base points was found for the leading half porous cylinder. However, the increase in the pressure value further downstream is slower than the solid and trailing-half porous

cylinders. The mean drag coefficient for the porous treated cylinder is obtained and compared with the bare cylinder. The highest decrease in the drag force is observed with the trailing-half porous cylinder when the mean drag coefficient is reduced by 13% compared to the solid cylinder.

CHAPTER 7

CONCLUSIONS AND FUTURE WORK

7.1 Introduction

Control of the flow and reduction of drag forces on bluff bodies using passive control is of increasing importance in many fields of engineering. One such control method is to add a porous element to the body to regularise the flow. The behaviour of systems comprising porous treatment on a bluff body in high Reynolds numbers of the fluid flow has not been widely reported in the literature. A significant research opportunity exists not only in the investigation of the efficacy of flow control and drag reduction by porous treatment in high Reynolds number turbulent flow, but also in carefully validating numerical methods for simulating the flow. This was accomplished in this project by performing a series of experiments and numerical simulations on bluff bodies with porous treatments located in a fluid flow to compare the flow behaviour over a bluff body without the treatment.

In the experiments, circular bluff bodies were treated by replacing half of the diameter of the cylinder with a porous layer. Bluff bodies with square and rectangular cross sections were treated such that their trailing halves comprised porous materials. The effect of the parameters of porous material on flow field and wake quantities was studied.

In addition, validation of the numerical methods has been achieved by the adoption of the numerical schemes for the prediction of the flow behaviour on boundaries where different equations govern the flow domain. Results from the laboratory experiments were used to validate the simulation results. Numerical simulations complemented the experiments by further investigating square bluff bodies with porous layers at their trailing and leading halves. Flow structures around and downstream of the square bluff bodies with different locations of the porous treatment in turbulent regime were determined and drag forces on the bodies were calculated. Due to the difference in the location of the porous-treatment for solid cylinders, results of porous-treated cylinders with circular cross section cannot be compared with the cylinders with square and rectangular cross sections. Nevertheless, each set of results can be used in an application that uses a particular cross-section. For the square and rectangular cylinders with the same porous treatment, however, similar effects on the flow structures have been found by the use of porous materials as the trailing halves of the cylinders.

The results obtained for all cases considered in this work demonstrated that the presence of open cell porous layers affect the wake formation. The mechanism of such effect is found to be related to the penetration of the flow inside the porous medium. Flow penetration damps the fluctuations in the velocity and Reynolds stress components of fluid flow in the wake of porous-treated cylinders. As a result, vortex shedding can be controlled by the treatment of solid cylinders with porous materials.

7.2 Key Contributions of the Research

This research contributes to existing knowledge of the three-dimensional flow over bluff bodies treated with porous material. Contributions have been made to several key areas, namely:

- Experimental studies showed that the application of porous media on different configurations of bluff bodies causes the recirculation bubbles to form further downstream all the bluff bodies studied.
- The biggest displacement of the recirculation bubbles to a location further downstream was found in the case of the circular-treated cylinders.
- The displacement of the recirculation bubbles in treated circular cylinders increases with the increase in the permeability of the porous material. Such dependency of the bubbles location to the permeability is less evident in square and rectangular cases.
- A sharp reduction in Reynolds stresses was also found in the presence of porous materials when the highest reduction was observed for the circular case. This implies the reduction in the TKE of the flow.
- Results of numerical investigations on the square cylinders showed that the trailing-half porous cylinder had the most shift in the recirculation bubbles compared with the leading-half porous cylinder.
- The replacement of the trailing half of a square cylinder with porous material caused the stream-wise velocity of the cylinder in the recirculation region gave rise to a reduction of about two compared to the untreated cylinder.
- The velocity profile of the leading-half porous cylinder is very similar to the bare cylinder in the near wake and has smaller values in the far wake.

- The velocity components in the shear layer near the walls change when the porous layer replaces a part of a square cylinder. The trailing-half porous cylinder showed the highest development in the boundary layer.
- The pressure distribution around the cylinders is strongly affected by the use of porous materials. The leading-half porous cylinder showed the maximum pressure difference between the front and base points of the cylinder.
- The drag coefficient was observed to be decreased in porous-treated cylinders. The trailing-half porous cylinder resulted in the highest reduction of drag coefficient equal to 13% compared to the bare cylinder.

The results of the present research provides researchers with new experimental data on the flow fields in the wake of bluff bodies treated by porous materials, which can be used as benchmark for future studies. In addition, designers of vehicles can benefit from the innovative idea presented in this research in controlling the flow around the vehicles and hence reducing drag, vibration, wear and tear and noise. Reducing the aerodynamic drag have the potential of energy saving and providing environmental benefits by reducing fuel consumption. This also helps manufacturers to comply with the environmental legislations regarding the emission of greenhouse gases.

7.3 Future Work

The research presented in this thesis represents a contribution to knowledge in the control of flow by porous treatment. However, it can still be extended in several ways such as investigation of the flow in different angles of attack, effects of porous treatment on noise generation and vibration and a parametric study for different configurations. These studies can improve our fundamental knowledge of porous flow control. The findings are also important in practical applications.

In studies on fluid flow over bluff bodies, the upstream velocity is commonly considered parallel to the axis of the bluff body the same way as it was considered in the present study. However, in the real world, the angle of oncoming fluid flow in relation to a reference line on the body is arbitrary, hence the angle of attack may assume arbitrary values. Also, even a streamlined body can behave like a bluff body at large angles of attack, as the flow detaches from the surface. Therefore, the flow effect on a surface is more completely defined when different likely directions of the undisturbed upstream velocity are considered. In the case of porous-treated bluff bodies it appears that there are no research findings on the effect of angle of attack on the flow characteristics. Therefore, studying different angles of attack can provide more realistic outcomes.

The flow control techniques not only affect the drag forces, as investigated in this research, but other researchers have observed an effect on the noise generated from a bluff body and the vibration of the structure. The study of noise and vibration were beyond the scope of this project. However, a comprehensive study including the effect of porous treatment on the drag reduction, noise generation and vibration is necessary for an optimized treatment. Therefore, any compromises can be minimised in the interest of a particular purpose. As an instance, when the reduction of noise in an airplane is desired, the study of the effect of passive control on the aerodynamic performance as the main function of the airplane is necessary.

Furthermore, the effect of porous material on the flow control depends on various parameters such as the configuration that the material is applied, the Reynolds number of the flow, the location and size of the porous material. In this regard, as another extension to this research, other configurations can be considered and studied in a range of geometric parameters. For a particular application, it is useful to perform a parametric

study. The velocities at which a specific device is subjected to determine the range of Reynolds numbers that should be considered. Different characteristics, locations and sizes of porous material also need to be investigated for optimal designs.

REFERENCES

Adler, P. M. (1981). "Streamlines in and around porous particles." Journal of Colloid and Interface Science **81**(2): 531-535.

Adrian, R. (1991). "Particle-imaging techniques for experimental fluid mechanics." Annual Review of Fluid Mechanics **23**(1): 261-304.

Adrian, R. J. (1986). "Image shifting technique to resolve directional ambiguity in double-pulsed velocimetry." Applied Optics **25**(21): 3855-3858.

Adrian, R. J. (2005). "Twenty years of particle image velocimetry." Experiments in Fluids **39**(2): 159-169.

Adrian, S. and David, H. (2005). "Correcting for sub-grid filtering effects in particle image velocimetry data." Measurement Science and Technology **16**(11): 2323.

Angland, D., X Zhang and Molin, N. (2009). "Measurements of flow around a flap side edge with porous edge treatment." AIAA Journal **47**(7): 1660-1671.

ANSYS FLUENT 15.0: *Theory Guide*, Release 15.0, ANSYS Inc., Canonsburg, PA.

Antohe, B. V., Lage, J. L., Price, D. C. and Weber, R. M. (1997). "Experimental Determination of Permeability and Inertia Coefficients of Mechanically Compressed Aluminum Porous Matrices." Journal of Fluids Engineering **119**(2): 404-412.

Arquis, E. and Caltagirone, J. P. (1984). {Sur les conditions hydrodynamiques au voisinage d'une interface milieu fluide-milieu poreux: application à la convection naturelle}. {Comptes Rendus de l'Académie des Sciences}.

Bae, Y., Jeong, Y. and Moon, Y. (2009). "Effect of Porous Surface on the Flat Plate Self-Noise." 15th AIAA/CEAS Aeroacoustics Conference (30th AIAA Aeroacoustics Conference), American Institute of Aeronautics and Astronautics.

Bai, W., Mingham, C. G., Causon, D. M. and Qian, L. (2016). "Detached eddy simulation of turbulent flow around square and circular cylinders on Cartesian cut cells." Ocean Engineering **117**: 1-14.

Baker, J. P. and Dam, C. P. V. (2008). Drag reduction of blunt trailing-edge airfoils. BBAA VI International Colloquium on: Bluff Bodies Aerodynamics & Applications Milano, Italy: 20-24.

- Barkley, D. and Henderson, R. D. (1996). "Three-dimensional Floquet stability analysis of the wake of a circular cylinder." Journal of Fluid Mechanics **322**: 215-241.
- Bear, J. (1972). Dynamics of Fluids In Porous Media, American Elsevier Publishing Company.
- Bearman, P. W. (1984). "Vortex Shedding from Oscillating Bluff Bodies." Annual Review of Fluid Mechanics **16**(1): 195-222.
- Beavers, G. S. and Joseph, D. (1967). "Boundary Conditions at a Naturally Permeable Wall." Journal of Fluid Mechanics **30**(1): 197-207.
- Bejan, A. (1984). Convection heat transfer, New York: Wiley.
- Blevins, R. D. (1977). Flow-induced vibration, New York: Van Nostrand Reinhold Co.
- Bellman, M., Agarwal, R., Naber, J., and Chusak, L. (2010). "Reducing energy consumption of ground vehicles by active flow control. " In ASME 2010 4th International Conference on Energy Sustainability, pp 785- 793, American Society of Mechanical Engineers.
- Bhattacharyya, S., Dhinakaran, S. and Khalili, A. (2006). "Fluid motion around and through a porous cylinder." Chemical Engineering Science **61**(13): 4451-4461.
- Bhattacharyya, S. and Singh, A. K. (2011). "Reduction in drag and vortex shedding frequency through porous sheath around a circular cylinder." International Journal for Numerical Methods in Fluids **65**(6): 683-698.
- Bloor, M. S. (2006). "The transition to turbulence in the wake of a circular cylinder." Journal of Fluid Mechanics **19**(2): 290-304.
- Boileau, M., Duchaine, F., Jouhaud, J. C. and Sommerer, Y. (2013). "Large-Eddy Simulation of Heat Transfer Around a Square Cylinder Using Unstructured Grids." AIAA Journal **51**(2): 372-385.
- Bosl, W. J., Jack, D. and Amos, N. (1998). "A study of porosity and permeability using a lattice Boltzmann simulation." Geophysical Research Letters **25**(9): 1475-1478.
- Brede, M., Eckelmann, H. and Rockwell, D. (1996). "On secondary vortices in the cylinder wake." Physics of Fluids **8**(8): 2117-2124.
- Brinkman, H. C. (1949). "A calculation of the viscous force exerted by a flowing fluid on a dense swarm of particles." Flow, Turbulence and Combustion **1**(1): 27.

- Brooks, T. F., Pope, D. S. and Marcolini, M. A. (1989). "Airfoil self-noise and prediction." NASA Reference Publication 1218.
- Browand, F. (2005). "Reducing Aerodynamic Drag and Fuel Consumption." Global Climate and Energy Project Workshop on Advanced Transportation. October 10-11, Stanford University.
- Bruneau, C.-H. and Mortazavi, I. (2004). "Passive control of the flow around a square cylinder using porous media." International Journal for Numerical Methods in Fluids **46**(4): 415-433.
- Bruneau, C.-H. and Mortazavi, I. (2008). "Numerical modelling and passive flow control using porous media." Computers & Fluids **37**(5): 488-498.
- Bruun, H. H. (1995). Hot-wire anemometry : principles and signal analysis. Oxford ; New York: Oxford University Press.
- Buchhave, P. (1992). "Particle image velocimetry—status and trends." Experimental Thermal and Fluid Science **5**(5): 586-604.
- Cancelliere, A., Chang, C., Foti, E., Rothman, D. and Succi, S. (1990). "The permeability of a random medium: Comparison of simulation with theory." Physics of Fluids A: Fluid Dynamics **2**(12): 2085-2088.
- Cao, Y., Gunzburger, M., Hua, F. and Wang, X. (2010). "Coupled Stokes-Darcy model with Beavers-Joseph interface boundary condition." Commun. Math. Sci. **8**(1): 1-25.
- Cao, Y. and Tamura, T. (2016). "Large-eddy simulations of flow past a square cylinder using structured and unstructured grids." Computers & Fluids **137**: 36-54.
- Carosone, F., Cenedese, A. and Querzoli, G. (1995). "Recognition of partially overlapped particle images using the Kohonen neural network." Experiments in Fluids **19**(4): 225-232.
- Carpenter, P., Davies, C., & Lucey, A. (2000). "Hydrodynamics and compliant walls: Does the dolphin have a secret?." *Current Science*, *79*(6), 758-765. Retrieved from <http://www.jstor.org/stable/24104198>
- Chan, H. C., Huang, W. C., Leu, J. M. and Lai, C. J. (2007). "Macroscopic modeling of turbulent flow over a porous medium." International Journal of Heat and Fluid Flow **28**(5): 1157-1166.
- Chen, F. and Chen, C. F. (1992). "Convection in superposed fluid and porous layers." Journal of Fluid Mechanics **234**: 97-119.

- Chen, X. B., Low, H. T., Winoto, S. H. and Yu, P. (2008). "Numerical analysis for the flow past a porous square cylinder based on the stress - jump interfacial - conditions." International Journal of Numerical Methods for Heat & Fluid Flow **18**(5): 635-655.
- Chen, X. B., Yu, P., Winoto, S. H. and Low, H. T. (2009). "Numerical analysis for the flow past a porous trapezoidal - cylinder based on the stress - jump interfacial - conditions." International Journal of Numerical Methods for Heat & Fluid Flow **19**(2): 223-241.
- Choi, H., Jeon, W. P. and Kim, J. (2008). "Control of Flow Over a Bluff Body." Annual Review of Fluid Mechanics **40**(1): 113-139.
- Choi, S. and Choi, H. (2002). "Characteristics of flow over a rotationally oscillating cylinder at low Reynolds number." Physics of Fluids **14**(8): 2767-2777.
- Choudhari, M. and Khorrami, M. (2003). "Computational Study of Porous Treatment for an Altered Flap Side-Edge Flowfield." 9th AIAA/CEAS Aeroacoustics Conference and Exhibit, American Institute of Aeronautics and Astronautics.
- Costa, U. M. S., Jr, J. S. A., Makse, H. A. and Stanley, H. E. (1999). "The role of inertia on fluid flow through disordered porous media." Physica A: Statistical Mechanics and its Applications **266**(1): 420-424.
- Costa, V. A. F., Oliveira, L. A., Baliga, B. R. and Sousa, A. C. M. (2004a). "Simulation of coupled flows in adjacent porous and open domains using a control-volume finite-element method." Numerical Heat Transfer, Part A: Applications **45**(7): 675-697.
- Costa, V. A. F., Oliveira, M. S. A. and Sousa, A. C. M. (2004b). "Numerical simulation of non-Darcian flows through spaces partially filled with a porous medium." Computers & Structures **82**(17): 1535-1541.
- Coutanceau, M. and Defaye, J.-R. (1991). "Circular Cylinder Wake Configurations: A Flow Visualization Survey." Applied Mechanics Reviews **44**(6): 255-305.
- Craft, T. J. and Launder, B. E. (1996). "A Reynolds stress closure designed for complex geometries." International Journal of Heat and Fluid Flow **17**(3): 245-254.
- Darcy, H. (1856). *Les Fontaines Publiques de la Ville de Dijon: Exposition et Application des Principes a Suivre et des Formules a Employer dans les Questions de Distribution d'Eau*. In: Dalmont, V., Ed.,. Paris.
- D'Angelo, C. and Zunino, P. (2009). "A Finite Element Method Based on Weighted Interior Penalties for Heterogeneous Incompressible Flows." SIAM Journal on Numerical Analysis **47**(5): 3990-4020.

- Davidson, L. (2017). An introduction to turbulence models. Sweden: Chalmers University of Technology.
- Davis, R. W., Moore, E. F. and Purtell, L. P. (1984). "A numerical-experimental study of confined flow around rectangular cylinders." The Physics of Fluids **27**(1): 46-59.
- Dupuit, J. (1863). Etudes Théoriques et Pratiques sur le mouvement des Eaux dans les canaux découverts et à travers les terrains perméables (ed. 2.). Paris: Dunod.
- Dudderar, T. D., Meynart, R. and Simpkins, P. G. (1988). "Full-field laser metrology for fluid velocity measurement." Optics and Lasers in Engineering **9**(3): 163-199.
- Durão, D. F. G., Heitor, M. V. and Pereira, J. C. F. (1988). "Measurements of turbulent and periodic flows around a square cross-section cylinder." Experiments in Fluids **6**(5): 298-304.
- Durlofsky, L. and Brady, J. (1987). "Analysis of the Brinkman equation as a model for flow in porous media." The Physics of Fluids **30**(11): 3329-3341.
- Eisfeld, B. (2006). Numerical simulation of aerodynamic problems with a Reynolds stress turbulence model, Berlin, Heidelberg: Springer Berlin Heidelberg.
- Ergun, S. (1952). "Fluid flow through packed columns." Journal of Chemical Engineering Progress **48**: 89-94.
- Fink, M. R. and Bailey, D. A. (1980). Airframe noise reduction studies and clean-airframe noise investigation, NASA Contractor Report 159311.
- Fourar, M., Radilla, G., Lenormand, R. and Moyne, C. (2004). "On the non-linear behavior of a laminar single-phase flow through two and three-dimensional porous media." Advances in Water Resources **27**(6): 669-677.
- Franke, J., Hellsten, A., Schlunzen, K. H. and Carissimo, B. (2011). "The COST 732 Best Practice Guideline for CFD simulation of flows in the urban environment: a summary." International Journal of Environment and Pollution (IJEP) **44**(1/2/3/4): 419-427.
- García-Mayoral, R. and Jiménez, J. (2011). "Hydrodynamic stability and breakdown of the viscous regime over riblets." Journal of Fluid Mechanics **678**: 317-347.
- Gerrard, J. H. (1966). "The mechanics of the formation region of vortices behind bluff bodies." Journal of Fluid Mechanics **25**(2): 401-413.

- Geyer, T. and Sarradj, E. (2014). "Trailing Edge Noise of Partially Porous Airfoils. " 20th AIAA/CEAS Aeroacoustics Conference, American Institute of Aeronautics and Astronautics.
- Geyer, T., Sarradj, E. and Fritzsche, C. (2010a). "Measurement of the noise generation at the trailing edge of porous airfoils." Experiments in Fluids **48**(2): 291-308.
- Geyer, T., Sarradj, E. and Fritzsche, C. (2010b). "Porous Airfoils: Noise Reduction and Boundary Layer Effects." International Journal of Aeroacoustics **9**(6): 787-820.
- Grant, I. (1997). "Particle image velocimetry: A review." Proceedings of the Institution of Mechanical Engineers, Part C: Journal of Mechanical Engineering Science **211**(1): 55-76.
- Green, R. B. and Gerrard, J. H. (1993). "Vorticity measurements in the near wake of a circular cylinder at low Reynolds numbers." Journal of Fluid Mechanics **246**: 675-691.
- Greidanus, A., Delfos, R., Tokgoz, S. and Westerweel, J. (2015). "Riblet drag reduction and the effect of bulk fluid rotation in a fully turbulent taylor-couette flow. " European Drag Reduction and Flow Control Meeting – EDRFCM 2015 March 23–26, Cambridge, UK.
- Griffin, O. M. and Hall, M. S. (1991). "Review—Vortex Shedding Lock-on and Flow Control in Bluff Body Wakes." Journal of Fluids Engineering **113**(4): 526-537.
- Hahn, S., Je, J. and Choi, H. (2002). "Direct numerical simulation of turbulent channel flow with permeable walls." Journal of Fluid Mechanics **450**: 259-285.
- Hart, D. P. (2000). "Super-resolution PIV by recursive local-correlation." Journal of Visualization **3**(2): 187-194.
- Henderson, R. D. (1997). "Nonlinear dynamics and pattern formation in turbulent wake transition." Journal of Fluid Mechanics **352**: 65-112.
- Herr, M., Rossignol, K.-S., Delfs, J., Lippitz, N. and Mößner, M. (2014). "Specification of Porous Materials for Low-Noise Trailing-Edge Applications." 20th AIAA/CEAS Aeroacoustics Conference, American Institute of Aeronautics and Astronautics.
- Hooman, K., Li, J. and Dahari, M. (2017). "Thermal dispersion effects on forced convection in a porous-saturated pipe." Thermal Science and Engineering Progress **2**: 64-70.
- Hsu, C. T. and Cheng, P. (1990). "Thermal dispersion in a porous medium." International Journal of Heat and Mass Transfer **33**(8): 1587-1597.

- Huang, L., Huang, P. G., LeBeau, R. P. and Hauser, T. (2004). "Numerical Study of Blowing and Suction Control Mechanism on NACA0012 Airfoil." Journal of Aircraft **41**(5): 1005-1013.
- Jiménez, J., Uhlmann, M., Pinelli, A. and Kawahara, G. (2001). "Turbulent shear flow over active and passive porous surfaces." Journal of Fluid Mechanics **442**: 89-117.
- Jorgen, F. and Mutlu, S. B. (1997). Hydrodynamics Around Cylindrical Structures, World Scientific Publishing Company.
- Jue, T. C. (2004). "Numerical analysis of vortex shedding behind a porous square cylinder." International Journal of Numerical Methods for Heat & Fluid Flow **14**(5): 649-663.
- Kazuo, O. and Hang-Yu, L. (2000). "Particle-tracking velocimetry with new algorithms." Measurement Science and Technology **11**(6): 603.
- Keane, R. D. and Adrian, R. J. (1990). "Optimization of particle image velocimeters. I. Double pulsed systems." Measurement Science and Technology **1**(11): 1202.
- Khashehchi, M., Ashtiani Abdi, I., Hooman, K. and Roesgen, T. (2014). "A comparison between the wake behind finned and foamed circular cylinders in cross-flow." Experimental Thermal and Fluid Science **52**: 328-338.
- Khorrami, M. R. and Choudhari, M. (2003). Application of Passive Porous Treatment to Slat Trailing Edge Noise., NASA Technical Report 212416.
- Kladias, N. and Prasad, V. (1991). "Experimental verification of Darcy-Brinkman-Forchheimer flow model for natural convection in porous media." Journal of Thermophysics and Heat Transfer **5**(4): 560-576.
- Kline, S. J. and McClintock, F. A. (1953). "Describing the uncertainties in single sample experiments." Mechanical Engineering, **75**(1): 3-8.
- Koh, S. R., Meinke, M. H., Schroeder, W., Zhou, B. Y. and Gauger, N. R. (2014). "Noise Sources of Trailing-Edge Turbulence Controlled by Porous Media." " 20th AIAA/CEAS Aeroacoustics Conference, American Institute of Aeronautics and Astronautics.
- Koha, S. R., Meinke, M. H., Schroeder, W., Zhou, B. and Gauger, N. R. (2017). "Impact of Permeable Surface on Trailing-Edge Noise at Varying Lift." " 23rd AIAA/CEAS Aeroacoustics Conference, American Institute of Aeronautics and Astronautics.

- Kohring, G. A. (1991). "Calculation of the permeability of porous media using hydrodynamic cellular automata." Journal of Statistical Physics **63**(1): 411-418.
- Kuroda, M., Tamura, T. and Suzuki, M. (2007). "Applicability of LES to the turbulent wake of a rectangular cylinder—Comparison with PIV data." Journal of Wind Engineering and Industrial Aerodynamics **95**(9): 1242-1258.
- Larson, R. E. and Higdon, J. J. L. (1986). "Microscopic flow near the surface of two-dimensional porous media. Part 1. Axial flow." Journal of Fluid Mechanics **166**: 449-472.
- Larson, R. E. and Higdon, J. J. L. (1987). "Microscopic flow near the surface of two-dimensional porous media. Part 2. Transverse flow." Journal of Fluid Mechanics **178**: 119-136.
- Lauterborn, W. and Vogel, A. (1984). "Modern Optical Techniques in Fluid Mechanics." Annual Review of Fluid Mechanics **16**(1): 223-244.
- Lecuona, A., Ruiz-Rivas, U. and Nogueira, J. (2002). "Simulation of particle trajectories in a vortex-induced flow: application to seed-dependent flow measurement techniques." Measurement Science and Technology **13**(7): 1020.
- Liebenberg, L. and Meyer, J. (2007). Intube passive heat transfer enhancement in the process industry.
- Lienhart, H., Stoots, C. and Becker, S. (2002). Flow and Turbulence Structures in the Wake of a Simplified Car Model (Ahmed Modell). New Results in Numerical and Experimental Fluid Mechanics III, Berlin, Heidelberg: Springer.
- Lin, J. T. and Pao, Y. H. (1979). "Wakes in Stratified Fluids." Annual Review of Fluid Mechanics **11**(1): 317-338.
- Liu, H., Azarpeyvand, M., Wei, J. and Qu, Z. (2015). "Tandem cylinder aerodynamic sound control using porous coating." Journal of Sound and Vibration **334**: 190-201.
- Liu, H., Wei, J. and Qu, Z. (2012). "Prediction of aerodynamic noise reduction by using open-cell metal foam." Journal of Sound and Vibration **331**(7): 1483-1497.
- Liu, H., Wei, J. and Qu, Z. (2013). "The Interaction of Porous Material Coating With the Near Wake of Bluff Body." Journal of Fluids Engineering **136**(2): 021302-021302-021308.
- Lockhard, D. P. and Lilley, G. M. (2004). The Airframe Noise Reduction Challenge. NASA Technical Report NASA/TM-2004-213013, L-18346.

- Lu, G., Lu, G. Q. and Xiao, Z. M. (1999). "Mechanical Properties of Porous Materials." *Journal of Porous Materials* **6**(4): 359-368.
- Lübcke, H., Schmidt, S., Rung, T. and Thiele, F. (2001). "Comparison of LES and RANS in bluff-body flows." *Journal of Wind Engineering and Industrial Aerodynamics* **89**(14): 1471-1485.
- Lundgren, T. S. and Ashurst, W. T. (1989). "Area-varying waves on curved vortex tubes with application to vortex breakdown." *Journal of Fluid Mechanics* **200**: 283-307.
- Lyn, D. A., Einav, S., Rodi, W. and Park, J. H. (1995). "A laser-Doppler velocimetry study of ensemble-averaged characteristics of the turbulent near wake of a square cylinder." *Journal of Fluid Mechanics* **304**: 285-319.
- Lyu, B. and Azarpeyvand, M. (2017). "On the noise prediction for serrated leading edges." *Journal of Fluid Mechanics* **826**: 205-234.
- Marshall, T. J. (1958). "A relation between permeability and size distribution of pores." *Journal of Soil Science* **9**(1): 1-8.
- Melling, A. (1997). "Tracer particles and seeding for particle image velocimetry." *Measurement Science and Technology* **8**(12): 1406.
- Menter, F., Hemstrom, B., Henriksson, M., Karlsson, R., Latrobe, A., Martin, A., . . . Willemsen, S. (2002). *CFD Best Practice Guidelines for CFD Code Validation for Reactor-Safety Applications*, Report EVOL-ECORA-D01, Contract No. FIKS-CT-2001-00154.
- Menter, F. R. (1994). "Two-equation eddy-viscosity turbulence models for engineering applications." *AIAA Journal* **32**(8): 1598-1605.
- Menter, F. R. (2009). "Review of the shear-stress transport turbulence model experience from an industrial perspective." *International Journal of Computational Fluid Dynamics* **23**(4): 305-316.
- Minguez, M., Brun, C., Pasquetti, R. and Serre, E. (2011). "Experimental and high-order LES analysis of the flow in near-wall region of a square cylinder." *International Journal of Heat and Fluid Flow* **32**(3): 558-566.
- Minguez, M., Pasquetti, R. and Serre, E. (2008). "High-order large-eddy simulation of flow over the "Ahmed body" car model." *Physics of Fluids* **20**(9): 095101.

- Mobner, M. and Radespiel, R. (2017). "Flow Simulations over Porous Media & Comparisons with Experiments." Computers and Fluids **154**: 358-370.
- Naim, A., Greenblatt, D., Seifert, A. and Wignanski, I. (2007). "Active Control of a Circular Cylinder Flow at Transitional Reynolds Numbers." Flow, Turbulence and Combustion **78**(3): 383-407.
- Naito, H. and Fukagata, K. (2012). "Numerical simulation of flow around a circular cylinder having porous surface." Physics of Fluids **24**(11): 117102.
- Nazarov, R., Jin, H.-J. and Kaplan, D. L. (2004). "Porous 3-D Scaffolds from Regenerated Silk Fibroin." Biomacromolecules **5**(3): 718-726.
- Neale, G., Epstein, N. and Nader, W. (1973). "Creeping flow relative to permeable spheres." Chemical Engineering Science **28**(10): 1865-1874.
- Nield, D. A. (1991). "The limitations of the Brinkman-Forchheimer equation in modeling flow in a saturated porous medium and at an interface." International Journal of Heat and Fluid Flow **12**(3): 269-272.
- Nield, D. A. and Bejan, A. (2014). Convection in Porous Media, New York: Springer.
- Norberg, C. (1986). "Interaction between freestream turbulence and vortex shedding for a single tube in cross-flow." Journal of Wind Engineering and Industrial Aerodynamics **23**: 501-514.
- Noymer, P. D., Glicksman, L. R. and Devendran, A. (1998). "Drag on a permeable cylinder in steady flow at moderate Reynolds numbers." Chemical Engineering Science **53**(16): 2859-2869.
- Ochoa-Tapia, J. A. and Whitaker, S. (1995a). "Momentum transfer at the boundary between a porous medium and a homogeneous fluid—I. Theoretical development." International Journal of Heat and Mass Transfer **38**(14): 2635-2646.
- Ochoa-Tapia, J. A. and Whitaker, S. (1995b). "Momentum transfer at the boundary between a porous medium and a homogeneous fluid—II. Comparison with experiment." International Journal of Heat and Mass Transfer **38**(14): 2647-2655.
- Oertel, H. J. (1990). "Wakes Behind Blunt Bodies." Annual Review of Fluid Mechanics **22**(1): 539-562.
- Okajima, A. (1982). "Strouhal numbers of rectangular cylinders." Journal of Fluid Mechanics **123**: 379-398.

- Park, H., Bernitsas, M. M. and Kumar, R. A. (2011). "Selective Roughness in the Boundary Layer to Suppress Flow-Induced Motions of Circular Cylinder at $30,000 < \text{Re} < 120,000$." (44397): 715-724.
- Peng, Y., Zeng, Y., Lee, T. S., Chen, X. B. and Low, H. T. (2011). "Steady flow around and through a permeable circular cylinder." Computers & Fluids **42**(1): 1-12.
- Peng, Y., Zeng, Y., Lee, T. S., Chen, X. B. and Low, H. T. (2012). "Numerical simulation on steady flow around and through a porous sphere." International Journal of Heat and Fluid Flow **36**: 142-152.
- Perng, S.-W., Wu, H.-W., Wang, R.-H. and Jue, T.-C. (2011). "Unsteady convection heat transfer for a porous square cylinder varying cylinder-to-channel height ratio." International Journal of Thermal Sciences **50**(10): 2006-2015.
- Pop, I.I. and Ingham, D.B., Eds. (2001) Convective Heat Transfer: Mathematical and Computational Modelling of Viscous Fluids and Porous Media. The Netherlands: Elsevier Science & Technology Books.
- Pope, S. B. (2000). Turbulent Flows, Cambridge, United Kingdom: Cambridge University Press.
- Prasad, A. K. (2000). "Stereoscopic particle image velocimetry." Experiments in Fluids **29**(2): 103-116.
- Raffel, M., Seelhorst, U. and Willert, C. (1998). "Vortical Flow Structures at a Helicopter Rotor Model Measured by LDV and PIV." The Aeronautical Journal of the Royal Aeronautical Society **102**: 221-227.
- Rajagopal, K. R. (2007). "On a hierarchy of approximate models for flows of incompressible fluids through porous solids." Mathematical Models and Methods in Applied Sciences **17**(02): 215-252.
- Rashidi, S., Tamayol, A., Valipour, M. S. and Shokri, N. (2013). "Fluid flow and forced convection heat transfer around a solid cylinder wrapped with a porous ring." International Journal of Heat and Mass Transfer **63**: 91-100.
- Rees, D. A. S. (2015). "On convective boundary layer flows of a Bingham fluid in a porous medium." International Journal of Heat and Mass Transfer **82**: 206-212.
- Revell, J., Revell, J., Kuntz, H., Balena, F., Horne, C., Storms, B., . . . Dougherty, R. (1997). "Trailing-edge flap noise reduction by porous acoustic treatment." 3rd AIAA/CEAS Aeroacoustics Conference, American Institute of Aeronautics and Astronautics.

- Robichaux, J., Balachandar, S. and Vanka, S. P. (1999). "Three-dimensional Floquet instability of the wake of square cylinder." Physics of Fluids **11**(3): 560-578.
- Robinson, S. K. (1991). "Coherent Motions in the Turbulent Boundary Layer." Annual Review of Fluid Mechanics **23**(1): 601-639.
- Rong, F. M., Guo, Z. L., Lu, J. H. and Shi, B. C. (2011). "Numerical simulation of the flow around a porous covering square cylinder in a channel via lattice Boltzmann method." International Journal for Numerical Methods in Fluids **65**(10): 1217-1230.
- Roshko, A. (1954). On the drag and shedding frequency of two-dimensional bluff bodies. Washington, D.C, National Advisory Committee for Aeronautics.
- Roshko, A. (1993). "Perspectives on bluff body aerodynamics." Journal of Wind Engineering and Industrial Aerodynamics **49**(1): 79-100.
- Rothman, D. H. (1988). "Cellular - automaton fluids: A model for flow in porous media." GEOPHYSICS **53**(4): 509-518.
- Sarioglu, M. (2017). "Control of flow around a square cylinder at incidence by using a splitter plate." Flow Measurement and Instrumentation **53**: 221-229.
- Sarradj, E. and Geyer, T. (2007). "Noise generation by porous airfoils. " 13th AIAA/CEAS Aeroacoustics Conference. AIAA-2007, Rome, Italy.
- Sauret, E., Hooman, K. and Saha, S. C. (2014). "CFD Simulations of Flow and Heat Transfer Through the Porous Interface of a Metal Foam Heat Exchanger." (46087): V001T003A005.
- Schewe, G. (2006). "On the force fluctuations acting on a circular cylinder in crossflow from subcritical up to transcritical Reynolds numbers." Journal of Fluid Mechanics **133**: 265-285.
- Schneider, K. (2005). "Numerical simulation of the transient flow behaviour in chemical reactors using a penalisation method." Computers & Fluids **34**(10): 1223-1238.
- Schneider, K. and Farge, M. (2002). "Adaptive Wavelet Simulation of a Flow around an Impulsively Started Cylinder Using Penalisation." Applied and Computational Harmonic Analysis **12**(3): 374-380.
- Schulze, J. and Sesterhenn, J. (2013). "Optimal distribution of porous media to reduce trailing edge noise." Computers & Fluids **78**: 41-53.

- Schwartz, L. M., Martys, N., Bentz, D. P., Garboczi, E. J. and Torquato, S. (1993). "Cross-property relations and permeability estimation in model porous media." Physical Review E **48**(6): 4584-4591.
- Shi, L., Zhang, C., Wang, J. and Ren, L. (2012). "Numerical Simulation of the Effect of Bionic Serrated Structures on the Aerodynamic Noise of a Circular Cylinder." Journal of Bionic Engineering **9**(1): 91-98.
- Shimada, K. and Ishihara, T. (2002). "Application of a modified $k-\epsilon$ model to the prediction of aerodynamic characteristics of rectangular cross-section cylinders." Journal of Fluids and Structures **16**(4): 465-485.
- Showkat Ali, S. A., Azarpeyvand, M. and Ilario da Silva, C. R. (2017). "Experimental Study of Porous Treatment for Aerodynamic and Aeroacoustic Purposes." 23rd AIAA/CEAS Aeroacoustics Conference, American Institute of Aeronautics and Astronautics.
- Showkat Ali, S. A., Azarpeyvand, M. and Ilário da Silva, C. R. (2018). "Trailing-edge flow and noise control using porous treatments." Journal of Fluid Mechanics **850**: 83-119.
- Showkat Ali, S. A., Liu, X. and Azarpeyvand, M. (2016). "Bluff Body Flow and Noise Control Using Porous Media." 22nd AIAA/CEAS Aeroacoustics Conference, American Institute of Aeronautics and Astronautics.
- Siegel, S. G., Cohen, K. and McLaughlin, T. (2006). "Numerical Simulations of a Feedback-Controlled Circular Cylinder Wake." AIAA Journal **44**(6): 1266-1276.
- Snyder, L. J. and Stewart, W. E. (1966). "Velocity and pressure profiles for newtonian creeping flow in regular packed beds of spheres." AIChE Journal **12**(1): 167-173.
- Sohankar, A. (2008). "Large eddy simulation of flow past rectangular-section cylinders: Side ratio effects." Journal of Wind Engineering and Industrial Aerodynamics **96**(5): 640-655.
- Sohankar, A., Davidson, L. and Norberg, C. (2000). Large Eddy Simulation of Flow Past a Square Cylinder: Comparison of Different Subgrid Scale Models.
- Standish, K. J. and van Dam, C. P. (2003). "Analysis of Blunt Trailing Edge Airfoils." Journal of Solar Energy Engineering **25**(4): 479-487.
- Succi, S., Benzi, R. and Higuera, F. (1991). "The lattice Boltzmann equation: A new tool for computational fluid-dynamics." Physica D: Nonlinear Phenomena **47**(1): 219-230.

- Sudin, M.N., Abdullah, M.A., Shamsuddin, S.A., Ramli, F.R., & Tahir, M.M. (2014). "Review of Research on Vehicles Aerodynamic Drag Reduction Methods. " International Journal of Mechanical & Mechatronics Engineering **14**(2): 35-47.
- Sumer, B. M. and Fredsøe, J. (2006). Hydrodynamics Around Cylindrical Structures, World Scientific.
- Takeshi, S., Takehisa, T., Mitsuru, I. and Norio, A. (2010). "Application of porous material to reduce aerodynamic sound from bluff bodies." Fluid Dynamics Research **42**(1): 015004.
- Tan, H. and Pillai, K. M. (2009). "Finite element implementation of stress-jump and stress-continuity conditions at porous-medium, clear-fluid interface." Computers & Fluids **38**(6): 1118-1131.
- Thompson, M., Hourigan, K. and Sheridan, J. (1996). "Three-dimensional instabilities in the wake of a circular cylinder." Experimental Thermal and Fluid Science **12**(2): 190-196.
- Timmins, B. H. Smith, B. L. and Vlachos P. P. (2010). "Automatic particle image velocimetry uncertainty quantification". In: ASME 2010 3rd Joint US-European Fluids Engineering Summer Meeting collocated with 8th International Conference on Nanochannels, Microchannels, and Minichannels. American Society of Mechanical Engineers. (49484):2811–2826.
- Trias, F. X., Gorobets, A. and Oliva, A. (2015). "Turbulent flow around a square cylinder at Reynolds number 22,000: A DNS study." Computers & Fluids **123**: 87-98.
- Ünal, U. u. O., Atlar, M. and Gören, Ö. (2010). "Effect of turbulence modelling on the computation of the near-wake flow of a circular cylinder." Ocean Engineering **37**(4): 387-399.
- Usera, G., Vernet, A. and Ferre, J. (2004). Considerations and improvements of the analysing algorithms used for time resolved PIV of wall bounded flows. the 12th international symposium on applications of laser techniques to fluid mechanics, Lisbon.
- Vafai, K. (2005). Handbook of porous media, Crc Press.
- Vafai, K. and Kim, S. (1990). "Fluid mechanics of the interface region between a porous medium and a fluid layer-an exact solution." International Journal of Heat and Fluid Flow **11**(3): 254-256.
- Vafai, K. and Kim, S. J. (1995). "On the limitations of the Brinkman-Forchheimer-extended Darcy equation." International Journal of Heat and Fluid Flow **16**(1): 11-15.

Vafai, K. and Tien, C. L. (1981). "Boundary and inertia effects on flow and heat transfer in porous media." International Journal of Heat and Mass Transfer **24**(2): 195-203.

Valipour, M. S., Rashidi, S., Bovand, M. and Masoodi, R. (2014). "Numerical modeling of flow around and through a porous cylinder with diamond cross section." European Journal of Mechanics - B/Fluids **46**: 74-81.

Vaz, G., Mabilat, C., van der Wal, R. and Gallagher, P. (2007). "Viscous Flow Computations on a Smooth Cylinders: A Detailed Numerical Study With Validation." (4269X): 849-860.

Venkataraman, D. and Bottaro, A. (2012). "Numerical modeling of flow control on a symmetric aerofoil via a porous, compliant coating." Physics of Fluids **24**(9): 093601.

Vickery, B. J. (1966). "Fluctuating lift and drag on a long cylinder of square cross-section in a smooth and in a turbulent stream." Journal of Fluid Mechanics **25**(3): 481-494.

Vu, H. C., Ahn, J. and Hwang, J. H. (2016). "Numerical investigation of flow around circular cylinder with splitter plate." KSCE Journal of Civil Engineering **20**(6): 2559-2568.

Walsh, M. J. (1983). "Riblets as a Viscous Drag Reduction Technique." AIAA Journal **21**(4): 485-486.

Wang, Y., Wu, C., Tan, G. and Deng, Y. (2017). "Reduction in the aerodynamic drag around a generic vehicle by using a non-smooth surface." Proceedings of the Institution of Mechanical Engineers, Part D: Journal of Automobile Engineering **231**(1): 130-144.

West, G. S. and Apelt, C. J. (1982). "The effects of tunnel blockage and aspect ratio on the mean flow past a circular cylinder with Reynolds numbers between 104 and 105." Journal of Fluid Mechanics **114**: 361-377.

White, F. M. (2015). Fluid Mechanics, New York, United States: McGraw-Hill Education.

Wiegel, M. and Fischer, M. (1995). Proper orthogonal decomposition applied to PIV data for the oblique transition in a Blasius boundary layer. SPIE's 1995 International Symposium on Optical Science, Engineering, and Instrumentation, SPIE.

Wilcox, C. D. (2006). Turbulence Modeling for CFD, California, United States: D C W Industries.

- Williamson, C. H. K. (1988). "The existence of two stages in the transition to three-dimensionality of a cylinder wake." The Physics of Fluids **31**(11): 3165-3168.
- Williamson, C. H. K. (1996). "Vortex Dynamics in the Cylinder Wake." Annual Review of Fluid Mechanics **28**(1): 477-539.
- Williamson, C. H. K. and Govardhan, R. (2004). "Vortex-induced vibrations." Annual Review of Fluid Mechanics **36**(1): 413-455.
- Winnemöller, T. and van Dam, C. P. (2007). "Design and Numerical Optimization of Thick Airfoils Including Blunt Trailing Edges." Journal of Aircraft **44**(1): 232-240.
- Wiplier, O. and Ehrenstein, U. (2000). "Numerical simulation of linear and nonlinear disturbance evolution in a boundary layer with compliant walls." Journal of Fluids and Structures **14**(2): 157-182.
- Wu, W., Bernitsas, M. M. and Maki, K. (2014). "RANS Simulation Versus Experiments of Flow Induced Motion of Circular Cylinder With Passive Turbulence Control at 35,000 < RE < 130,000." Journal of Offshore Mechanics and Arctic Engineering **136**(4): 041802-041802-041810.
- Yu, P., Zeng, Y., Lee, T. S., Bai, H. X. and Low, H. T. (2010). "Wake structure for flow past and through a porous square cylinder." International Journal of Heat and Fluid Flow **31**(2): 141-153.
- Yunhua, H., David, W. G., Shelley, R. W. and Jeffrey, O. H. (2002). "Fabrication of poly(α -hydroxy acid) foam scaffolds using multiple solvent systems." Journal of Biomedical Materials Research **59**(3): 563-572.
- Zdravkovich, M. M. (2003). Flow Around Circular Cylinders, Vol 1: Fundamentals. Oxford, United Kingdom: OXFORD University Press.
- Zhang, R. and Ma, P. (1999). Poly(A-hydroxyl acids)/hydroxyapatite porous composites for bone-tissue engineering. I. Preparation and morphology.
- Zhao, M. and Cheng, L. (2010). "Finite element analysis of flow control using porous media." Ocean Engineering **37**(14): 1357-1366.
- Zhou, B. Y., Gauger, N. R., Koh, S. R., Meinke, M. H. and Schroeder, W. (2015). On the Adjoint-based Control of Trailing-Edge Turbulence and Noise Minimization via Porous Material. 21st AIAA/CEAS Aeroacoustics Conference, American Institute of Aeronautics and Astronautics.

APPENDIX A

TKE CONTENT IN THE WAKE OF CIRCULAR, SQUARE AND RECTANGULAR BLUFF BODIES

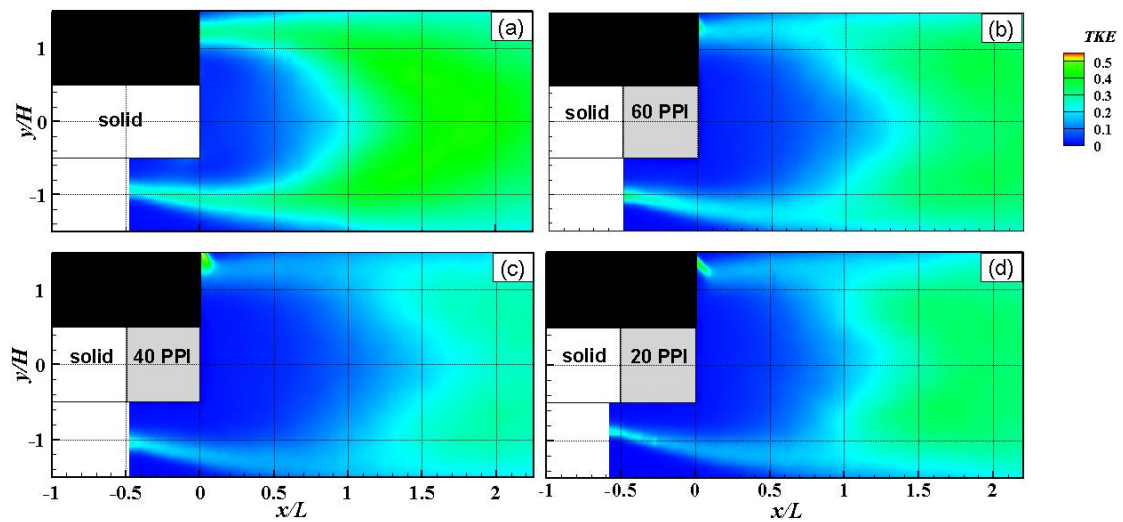


Figure A.1 TKE content in the wake of rectangular cylinders; (a) bare cylinder, (b) cylinder treated with 60 PPI porous layer, (c) cylinder treated with 40 PPI porous layer and (d) cylinder treated with 20 PPI porous layer

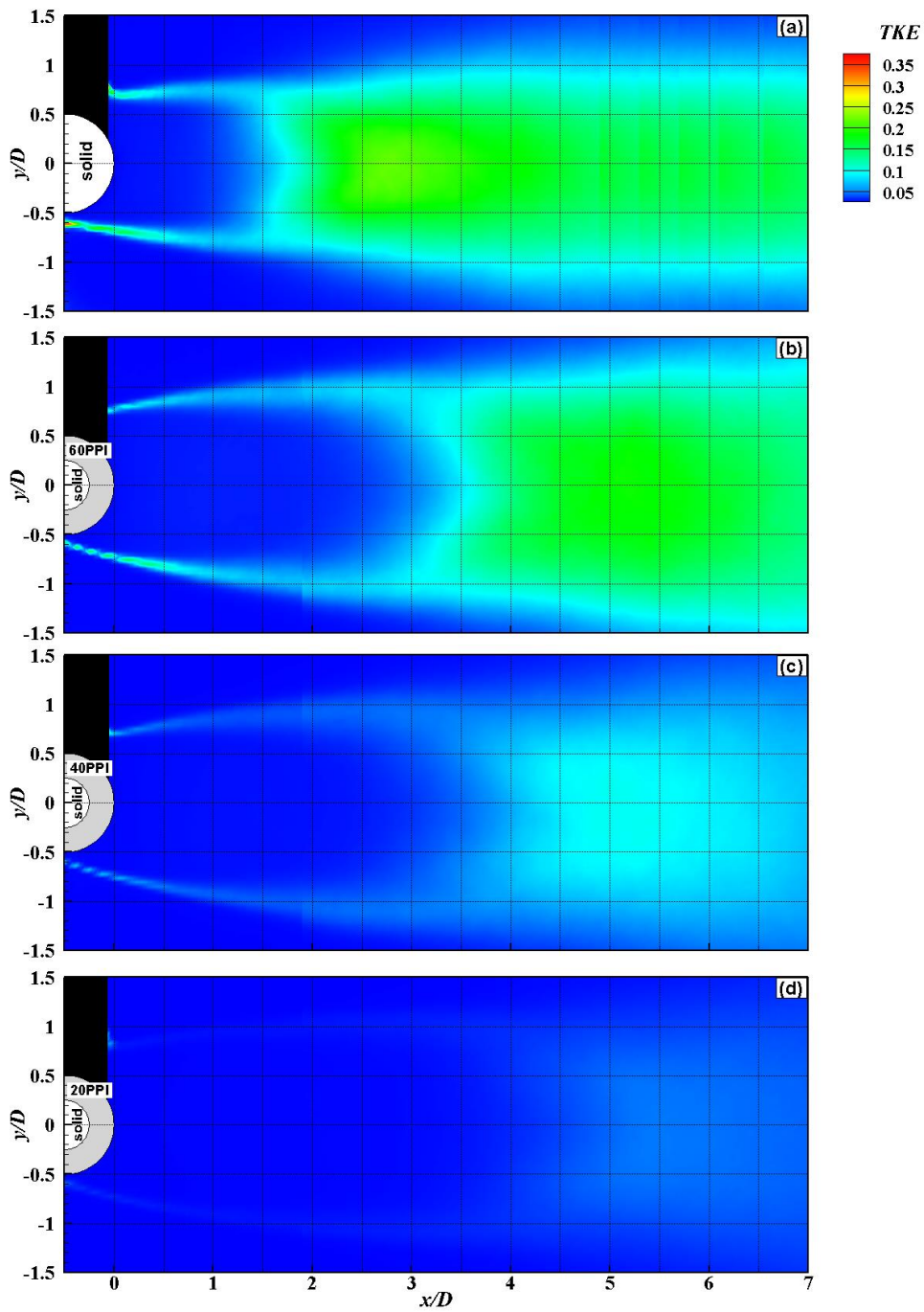


Figure A.2 TKE content in the wake of circular cylinders; (a) bare cylinder, (b) cylinder covered with 60 PPI porous layer, (c) cylinder covered with 40 PPI porous layer and (d) cylinder covered with 20 PPI porous layer

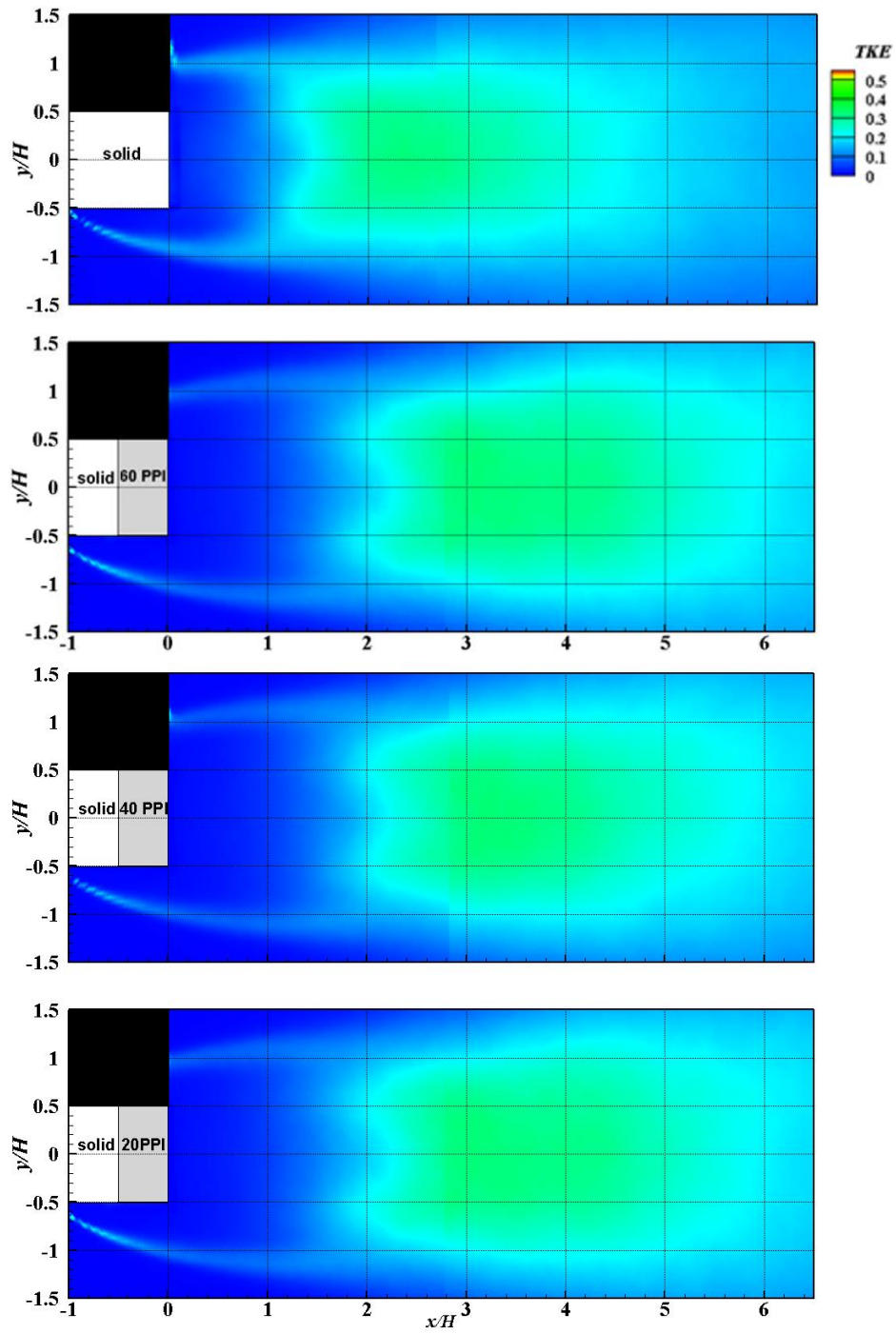


Figure A.3 TKE content in the wake of square cylinders; (a) bare cylinder, (b) cylinder treated with 60 PPI porous layer, (c) cylinder treated with 40 PPI porous layer and (d) cylinder treated with 20 PPI porous layer

APPENDIX B

GOVERNING EQUATIONS FOR RANS MODELLING

$$u_i(\mathbf{x}, t) = \bar{u}_i(\mathbf{x}, t) + u_i'(\mathbf{x}, t), \quad (\text{B.1})$$

in which $u_i(\mathbf{x}, t)$ are the instantaneous values, $u_i'(\mathbf{x}, t)$ are the fluctuating values and $\bar{u}_i(\mathbf{x}, t)$ denotes the time-averaged values defined as:

$$\bar{u}_i(\mathbf{x}, t) = \lim_{N \rightarrow \infty} \frac{1}{N} \sum_{n=1}^N u_i^{(n)}(\mathbf{x}, t). \quad (\text{B.2})$$

Applying the above averaging into the continuity equation and Navier-Stokes equation, their time-averaged representations become:

$$\frac{\partial \bar{u}_i}{\partial x_i} = 0, \quad (\text{B.3})$$

$$\frac{\partial \bar{u}_i}{\partial t} + \frac{\partial \bar{u}_i \bar{u}_j}{\partial x_j} = -\frac{1}{\rho} \frac{\partial \bar{p}}{\partial x_i} + \frac{\partial}{\partial x_j} \left(\nu \frac{\partial \bar{u}_i}{\partial x_j} - \rho \overline{u_i' u_j'} \right). \quad (\text{B.4})$$

Equation (B.4) is called the Reynolds-averaged Navier-Stokes (RANS) equation. The additional term $(\rho \overline{u'_i u'_j})$, called the Reynolds stress tensor, is introduced by the averaging procedure. This tensor is an unknown stress term caused by fluctuating velocities. Now we have four equations, continuity and three momentum equations, and a total number of ten unknowns in the equations, namely pressure, three velocity components plus six stress components. This gives rise to a closure problem, as the number of unknowns is more than the number of equations. To close this problem, we need expressions for the stress term, $\overline{u'_i u'_j}$. This is the essence of turbulence models. The turbulence models mainly fall into two categories; the eddy-viscosity models in which the Reynolds stress tensor is replaced by a turbulent viscosity (μ_T), and Reynolds-stress models in which Reynolds stress tensor is obtained by solving algebraic or differential equations. The eddy-viscosity models have been found to be satisfactory for modelling simple turbulent shear flows including, for example boundary layer and channel flows. The Reynolds-stress models perform better in complex three-dimensional flows such as swirling flows. The eddy-viscosity models are less computationally intensive and they converge more readily compared to Reynolds-stress models.